Comprehensive Analysis of Micro-Structure Dynamics in Longitudinal Electron Bunch Profiles

Master's Thesis of

Tobias Boltz

at the Department of Physics
Laboratory for Applications of Synchrotron Radiation (LAS)

Reviewer:	Prof. Dr. Anke-Susanne Müller
Second reviewer:	Prof. Dr. Günter Quast
Advisor:	Dr. Minjie Yan

March 17, 2017

I declare that I have developed and written the enclosed thesis completely by myself, and have not used sources or means without declaration in the text.

Karlsruhe, March 17, 2017

. . . .

(Tobias Boltz)

Accepted as master's thesis

. . . .

Abstract

The operation with short electron bunches at synchrotron light sources leads to the formation of micro-structures within the bunches, which increase the emitted coherent synchrotron radiation power. The dynamic changes of these micro-structures can indirectly be studied by measuring the resulting fluctuations of the emitted radiation power. Such fluctuations have been observed at various synchrotron light sources including ANKA, KIT. Although several techniques exist to measure the electron distribution within the bunch, the small scale of the micro-structures makes their direct observation quite challenging. Therefore, in this thesis, the longitudinal dynamics have been simulated using the newly developed simulation code Inovesa. As this quickly accumulates to large data sets, machine learning techniques are employed in order to identify the dominant micro-structures in the longitudinal bunch profiles. Subsequently, these findings are used to extensively study the characteristics and dynamics of the micro-structures, and to investigate their correlation to the emitted coherent synchrotron radiation.

Kurzfassung

Der Betrieb von Synchrotronstrahlungsquellen mit kurzen Elektronenpaketen führt zur Ausbildung von Mikro-Strukturen innerhalb der Pakete, was wiederum einen Anstieg der abgestrahlten kohärenten Synchrotronstrahlungs-Leistung zur Folge hat. Die dynamische Entwicklung dieser Mikro-Strukturen kann indirekt durch die Messung der resultierenden Fluktuationen der emittierten Strahlungsleistung untersucht werden. Diese Fluktuationen konnten an verschiedenen Synchrotronstrahlungsquellen gemessen werden, so auch an ANKA, KIT. Für die direkte Beobachtung der Mikro-Strukturen stehen zwar bereits einige Methoden zur Messung der Elektronenverteilung in den Paketen zur Verfügung, der kleine Maßstab stellt hier allerdings hohe Anforderung an die jeweilige Messtechnik. Zum Zwecke dieser Masterarbeit wurde die longitudinale Dynamik daher mittels des neu entwickelten Programms Inovesa simuliert. Da dies schnell zu großen Datenmengen führen kann, wurden Methoden des maschinellen Lernens eingesetzt, um die dominanten Mikro-Strukturen in den longitudinalen Elektronenverteilungen zu identifizieren. Anhand der so gewonnenen Resultate wird anschließend die Charakteristik und Dynamik der Mikro-Strukturen und deren Korrelation zur abgestrahlten kohärenten Synchrotronstrahlung ausführlich untersucht.

Contents

List of Figures

1. Introduction

First experimental observations of synchrotron radiation were made at the General Electric synchrotron in the United States in 1947 [1]. Back then, it was considered a nuisance as it was causing the accelerated particles to lose energy. In the following years to come, its characteristics were studied parasitically at high energy particle accelerators. However, it took until the 1960s before the exceptional properties of the synchrotron radiation were realized and the first dedicated storage ring for the production of synchrotron radiation was build in 1968 in Wisconsin, USA [2].

The continuous synchrotron radiation spectrum is emitted over a wide spectral range, covering frequencies from the far infra-red to hard X-rays. Furthermore, synchrotron radiation can yield highly collimated photon beams of high intensity, i.e. high flux and brilliance. Amongst other desirable properties, this leads to a multitude of different applications, e.g. in materials science, biology and medicine. One recent example for the applications of synchrotron radiation is the spectroscopy of biological macromolecules, which provides insights into fundamental cellular mechanisms and led to the award of the Nobel Prize in Chemistry to Lefkowitz and Kobilka in 2012 [3].

Today, synchrotron radiation is generated at specialized particle accelerators, called synchrotron light sources, which typically accelerate electrons as radiation source. Within the accelerator, the electrons are divided into distinct groups, the so-called bunches. If these bunches are short enough, parts of the synchrotron radiation are emitted coherently, and thus called coherent synchrotron radiation (CSR). The principle of CSR was already predicted by Nodvick and Saxon in 1954 [4], but its characteristics remain subject of today's research. The power of the emitted CSR can exceed the power of the incoherently emitted parts by several orders of magnitude, which is why some synchrotron light sources are deliberately operating with short bunch lengths. One example is the Ångström source Karlsruhe (ANKA), a test facility and synchrotron light source of the Karlsruhe Institute of Technology (KIT) operated by IBPT, where this thesis has been carried out.

While the reduction of the bunch length is intended to enhance the emitted synchrotron radiation power, it causes complex dynamics in the energy and longitudinal density distribution of the electrons inside the bunch, leading to the formation of dynamically changing micro-structures. This is also known as microwave instability [5] or micro-bunching instability [6]. The micro-structures can indirectly be studied by investigating the resulting fluctuations of the radiated CSR power, also called bursting [7]. Such observations have been made at various synchrotron light sources including ANKA [8], BESSY II [9], DIAMOND [10], MLS [11] and SOLEIL [6]. Additionally, they can be observed directly by measuring the longitudinal electron distribution, i.e. the longitudinal bunch profile, which might provide deeper insights, but is quite challenging to achieve. Several measurement techniques are existing, including e.g. the electro-optical setup [12] at ANKA, to observe these longitudinal bunch profiles at synchrotron light sources. However, the small scale of

these micro-structures results in such demanding requirements, that they can not easily be resolved so far, especially when the dynamics have to be studied over a relatively long time range with single shot capability. Thus, simulation codes have been developed to approximate and study especially the longitudinal dynamics within the electron bunch, including the simulation code Inovesa [13]. While several approximations have to be made, the such generated simulation data carries very low noise and therefore enables further investigations of the micro-structure dynamics.

In this thesis, the longitudinal dynamics and the corresponding radiation behavior are simulated using Inovesa. As the desired accuracy can quickly lead to large data sets, machine learning techniques have been employed to analyze the simulated longitudinal bunch profiles and to reveal the dominant micro-structures. Subsequently, the dynamics of the found micro-structures are extensively studied and its correlations to the observed fluctuations of the emitted CSR are investigated. In this process, several basic techniques to gain first direct insights to the underlying micro-structure dynamics are developed.

The thesis is structured in the following way: Chapter 2 gives a brief overview of the required fundamentals of accelerator physics and a short description of the phenomenon of bursts in the CSR emission. Subsequently, the employed machine learning techniques are introduced. The simulation code Inovesa and the used parameter settings to generate the data sets in this thesis are described in Chapter 3. Additionally, the concrete application of the previously mentioned machine learning techniques and the applied pre-processing are discussed. The results of this analysis are presented in Chapter 4. Besides different methods of visualizing the micro-structures, severals ways of evaluating these findings are explored. The chapter concludes by analyzing the scale and current-dependency of the found micro-structures. Chapter 5 contains a compilation of further characteristics of the micro-structures found in this thesis. This includes, e.g. the dynamics of a localized charge density within the electron bunch. Eventually, a signal-to-noise ratio benchmark test is conducted with regard to the application of the derived techniques on measured data. The thesis concludes with a brief summary and outlook in Chapter 6.

2. Theoretical Framework

The first part of this chapter contains some fundamentals of accelerator physics with a particular focus on the THz-Bursting phenomenon. The second part gives a short introduction to the field of machine learning and, moreover, includes a detailed description of the k-means method. The two parts together provide the necessary theoretical framework for this thesis.

2.1. Accelerator Physics

In the following, the required concepts of accelerator physics are briefly introduced. For a more extensive and detailed description it is referred to existing textbooks, e.g. Refs. [14] and [15].

2.1.1. Charged Particles in External Electromagnetic Fields

A particle with charge q and velocity $\boldsymbol{v}$ in external electromagnetic fields is subject to the Lorentz force:

$$ \boldsymbol{F}_{\mathrm{L}} = q \ (\boldsymbol{E} + \boldsymbol{v} \times \boldsymbol{B}) \ , \tag{2.1} $$

where $\boldsymbol{E}$ denotes the electric field and $\boldsymbol{B}$ is the magnetic field. Its motion from position $\boldsymbol{r}_1$ to $\boldsymbol{r}_2$ leads to the following change in the particle's energy:

$$ \Delta E = \int_{r_1}^{r_2} \boldsymbol{F}_{\mathrm{L}} \mathrm{d}\boldsymbol{r} = q \int_{r_1}^{r_2} (\boldsymbol{v} \times \boldsymbol{B} + \boldsymbol{E}) \, \mathrm{d}\boldsymbol{r} \ . \tag{2.2} $$

Given $\mathrm{d}\boldsymbol{r}$ is always parallel to the velocity vector $\boldsymbol{v}$, it follows $(\boldsymbol{v} \times \boldsymbol{B}) \, \mathrm{d}\boldsymbol{r}$ equals to zero. This means the change in energy ΔE is independent of the magnetic field $\boldsymbol{B}$, simplifying Eq. (2.2) to:

$$ \Delta E = q \int_{r_1}^{r_2} \boldsymbol{E} \mathrm{d}\boldsymbol{r} = qU \ , \tag{2.3} $$

where U is the potential difference induced by the electric field. Nevertheless, magnetic fields are essential in particle accelerators when it comes to beam guidance and deflection. Inducing a force component orthogonal to $\boldsymbol{v}$, a constant magnetic field yields a circular trajectory where the Lorentz force acts as the centripetal force:

$$ \frac{mv^2}{R} = qv|\boldsymbol{B}| \ , \tag{2.4} $$

where R is the circle's radius and m is the particle's mass. Considering relativistic particles with $v \equiv |\boldsymbol{v}| \approx c$, where c is the speed of light, it is apparent from Eq. (2.1) that the effects

of magnetic fields are by a factor of c stronger than those of electric fields. Hence, for circular accelerators operating at relativistic energies, electric fields are used to increase the particle's energy whereas bending and focusing of the beam is achieved via magnetic fields. One such example is the synchrotron which is described below.

2.1.2. Synchrotron as Storage Ring

Historically, the first particle accelerators in the 1920s utilized a static electric field induced between two electrodes. The maximum energy achieved by such technically accessible voltage is limited by the so-called corona effect, which causes a spark-over and thus the collapse of the high voltage. This led to the application of an alternating voltage for high energy accelerators. In order to avoid unintentional deceleration, the particles are only exposed to the sinusoidal voltage U_{RF} at a specific phase Ψ_s:

$$U_{RF}(t) = U_0 \sin(2\pi f_{RF} t + \Psi_s) \, . \tag{2.5}$$

With regard to the further increase of the particle's energy, there are generally two different designs. In a linear accelerator, the particles run through an iterative arrangement of accelerating structures along a straight line. In a circular accelerator however, the particles are forced on a circular orbit and run through the same accelerating structure multiple times. The synchrotron is such a circular accelerator with a constant bending radius R_s. For relativistic particles Eq. (2.4) yields:

$$R_s = \frac{E}{qc|\boldsymbol{B}|} = \text{const.} \, , \tag{2.6}$$

which means, the strength of the magnetic field has to be ramped up synchronously with increasing energy in order to keep the bending radius constant. Some of the existing synchrotrons can also be operated as a storage ring, where particles are stored at constant energy (implying also a constant magnetic field). This is particularly convenient when the accelerator is used as a synchrotron light source (see the section below).

Since particles can only be accelerated at specific phases, the resulting beam is not continuous, but consists of distinct groups of particles, the so-called bunches. This means, the accelerating radio-frequency f_{RF} and the revolution frequency f_{rev} relate as follows:

$$f_{RF} = h \, f_{rev} \, , \tag{2.7}$$

where h is an integer, called the harmonic number and states the maximum number of bunches in the storage ring. All particles from the different bunches accumulate to the total charge q_{tot} and therefore define the beam current together with the revolution frequency f_{rev} as:

$$I_{beam} = q_{tot} \, f_{rev} \, . \tag{2.8}$$

Additionally, the bunch current denotes the current which is solely generated by one particular bunch:

$$I_{bunch} = q_{bunch} \, f_{rev} \, . \tag{2.9}$$
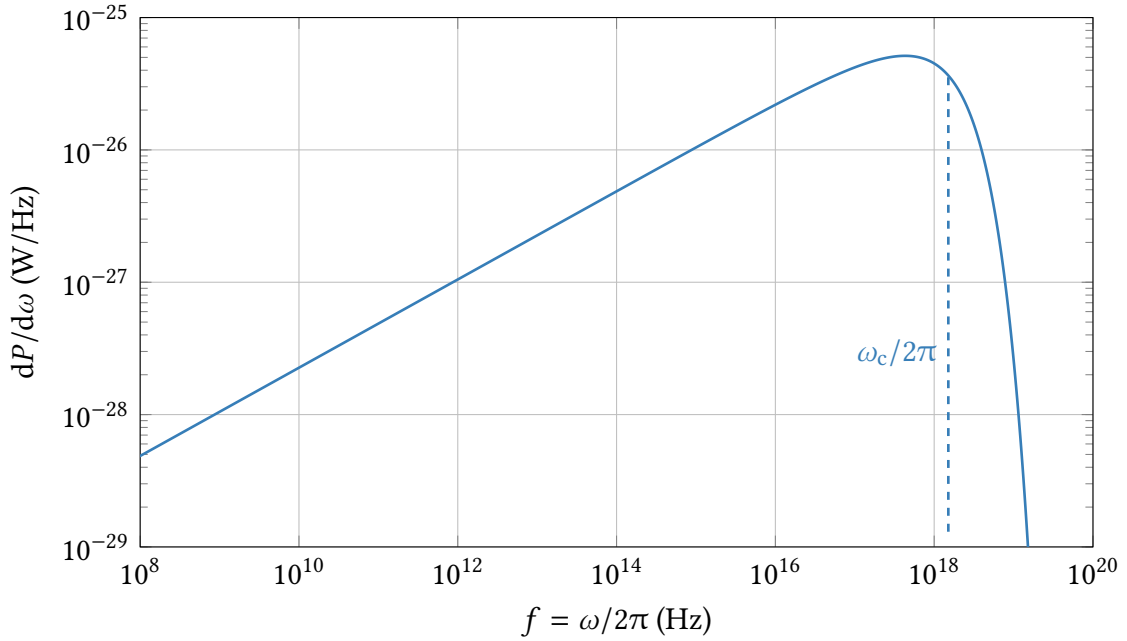
Figure 2.1.: Shown is the radiated power per unit frequency $\mathrm{d}P/\mathrm{d}\omega$ of the synchrotron radiation generated by a single electron. The radiation is emitted over a wide range of frequencies, where the critical frequency ω_c divides the spectrum into two sections with equal integrated radiation power. For this illustration, the incorporated bending radius $R_\mathrm{s} = 5.559\,\mathrm{m}$ and energy $E = 2.5\,\mathrm{GeV}$ are chosen equivalent to the ANKA storage ring.

2.1.3. Synchrotron Radiation

Fundamental rules of classical electrodynamics imply, accelerated charged particles lose energy by emitting electromagnetic waves. In the following, the radiation of a relativistic electron is treated. Since the energy loss due to longitudinal acceleration is negligible, only the radiation induced by acceleration in the transversal direction is considered. In the context of particle accelerators, this radiation is called synchrotron radiation, as it was observed at synchrotrons for the first time. The synchrotron radiation power for a single electron due to the force of a bending magnet is [14]:

$$P_\mathrm{s} = \frac{e^2 c}{6\pi\varepsilon_0} \frac{1}{(m_0 c^2)^4} \frac{E^4}{R_\mathrm{s}^2} \, , \tag{2.10}$$

with the electron charge e, the electron's rest mass m_0 and the dielectric constant of vacuum ε_0. Hence, the energy loss per turn is given by:

$$\Delta E = \oint P_\mathrm{s}\mathrm{d}t = \frac{1}{f_\mathrm{rev}} P_\mathrm{s} = \frac{2\pi R}{c} P_\mathrm{s} \, . \tag{2.11}$$

5

The synchrotron radiation is emitted over a wide range of frequencies. The radiated power per unit frequency, as illustrated in Figure 2.1, is given by [16]:

$$\frac{dP}{d\omega} = \frac{P_s}{\omega_c} \frac{9\sqrt{3}}{8\pi} \frac{\omega}{\omega_c} \int_{\omega/\omega_c}^{\infty} K_{5/3}(\xi)d\xi \, , \tag{2.12}$$

where $K_{5/3}$ is the modified Bessel function and ω_c denotes the critical frequency:

$$\omega_c = \frac{3c\gamma^3}{2R} \, , \tag{2.13}$$

with the relativistic quantities $\gamma = 1/\sqrt{1 - \beta^2}$ and $\beta = v/c$. This critical frequency divides the power spectrum into two sections of equal integrated radiation power:

$$\int_0^{\omega_c} \frac{dP}{d\omega} d\omega = \int_{\omega_c}^{\infty} \frac{dP}{d\omega} d\omega = \frac{1}{2} P_s \, . \tag{2.14}$$

Extending the scope from a single electron to the entirety of the bunch, the number of electrons involved is typically in the order of:

$$N_e \approx 10^9 \, . \tag{2.15}$$

Their combined radiation yields the incoherent synchrotron radiation:

$$\frac{dP_{isr}}{d\omega} = N_e \frac{dP}{d\omega} \, . \tag{2.16}$$

However, if the size of the emitting structure, i.e. the electron bunch, is in the order of the emitted wavelength ($\sigma_z/\lambda \approx 1$) or even smaller, a part of the synchrotron radiation is emitted coherently and thus called coherent synchrotron radiation (CSR). The coherently emitted radiation power per unit frequency is illustrated in Figure 2.2 and is given by [15]:

$$\frac{dP_{csr}}{d\omega} = N_e(N_e - 1)\mathcal{F}(k) \frac{dP}{d\omega} \, , \tag{2.17}$$

where $\mathcal{F}(k)$ denotes the form factor, which specifies the dependence of the emitted radiation power on the normalized electron distribution $\rho(r)$ within the bunch:

$$\mathcal{F}(k) = \left| \int \rho(r)e^{ikr}dr \right|^2 \, . \tag{2.18}$$

For this thesis, it is focused on the contribution of the longitudinal form factor:

$$\mathcal{F}_z(k_z) = \left| \int \rho(z)e^{ik_z z}dz \right|^2 \, . \tag{2.19}$$

The total synchrotron radiation power spectrum is finally given by:

$$\frac{dP_{tot}}{d\omega} = \frac{dP_{isr}}{d\omega} + \frac{dP_{csr}}{d\omega} = N_e \left[1 + (N_e - 1)\mathcal{F}(k)\right] \frac{dP}{d\omega} \, . \tag{2.20}$$

Due to the quadratic dependency on the number of electrons in Eq. (2.17), the coherent synchrotron radiation can increase the intensity of the emitted radiation considerably, which renders it a promising subject of scientific research and potential industrial applications.
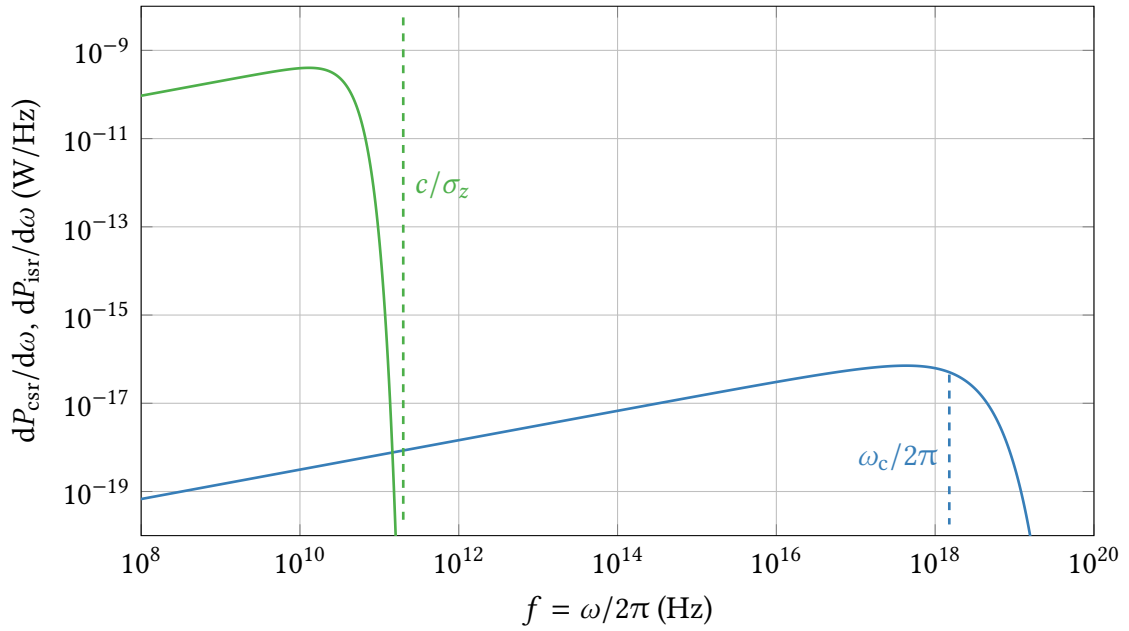
Figure 2.2.: For wavelengths $\lambda = c/f$ longer than the bunch length σ_z, i.e. for frequencies f smaller than c/σ_z, the CSR power (green) exceeds the power of the incoherent synchrotron radiation (blue) by several orders of magnitude. However, for wavelengths that are significantly shorter than the bunch length $\lambda \ll \sigma_z$, the power of the emitted CSR drops off rapidly. For this illustration, the same parameters as in Figure 2.1 are used and an exemplary electron bunch with current $I_\text{bunch} = 2\,\text{mA}$ and a Gaussian longitudinal electron distribution with $\sigma_z/c = 5\,\text{ps}$ is chosen.[1]

2.1.4. Longitudinal Beam Dynamics

The energy loss due to synchrotron radiation has to be compensated by the accelerating voltage. In a storage ring, the synchronous particle is defined to hold exactly the reference momentum p_s. The accelerating voltage $U_\text{RF}(t)$ is adjusted for the synchronous particle to pass through at the synchronous phase Ψ_s where it is subject to the voltage U_s. Therefore, the particle gains exactly the energy it loses due to synchrotron radiation. According to Eq. (2.6), a particle with lower energy and therefore momentum, i.e. $\delta p < 0$ with:

$$\delta p = (p - p_\text{s})/p_\text{s}\,, \tag{2.21}$$

gets deflected more by the bending magnets. This leads to a shorter orbit as illustrated in Figure 2.3a. Subsequently it arrives earlier at the accelerating structure, is exposed to a higher voltage and gains more energy (see Figure 2.3b). Vice versa, a particle with higher momentum ($\delta p > 0$) is deflected less, exposed to a lower voltage and therefore gains less energy.

The fact that in both cases the particle's energy and momentum are corrected toward those of the synchronous particle is deliberately designed and called phase focusing. These

---

[1] In practice, the electron bunch lengths are in the order of tens of picoseconds, but can be reduced by appropriate settings of the accelerator's magnets (see Section 2.1.5).

(a) Deviating orbits   (b) RF voltage U_{RF}
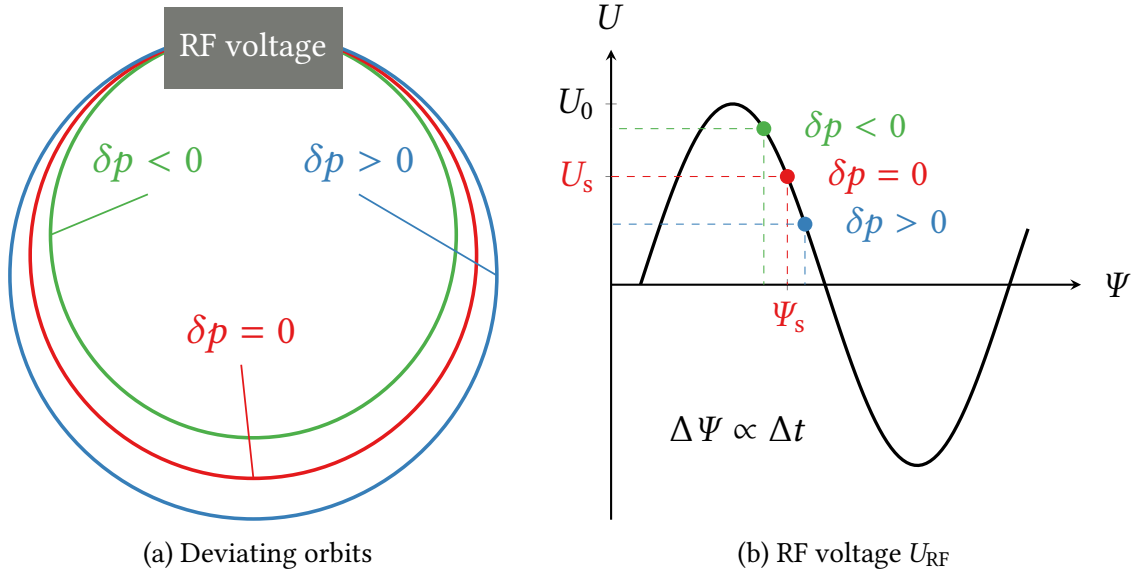
Figure 2.3.: Principle of phase focusing. (a) A particle with lower momentum than the synchronous particle (red line) moves on a shorter orbit (green line), whereas a higher momentum results in a longer orbit (blue line). (b) Particles with $\delta p < 0$ are subject to a higher voltage $U_{\text{RF}} > U_{\text{s}}$ and gain more energy, whereas particles with $\delta p > 0$ are subject to a lower voltage $U_{\text{RF}} < U_{\text{s}}$ and gain less energy. In both cases, energy and momentum are corrected toward those of the synchronous particle. Figure adapted and based on [17].

effects result in a longitudinal oscillation or so-called synchrotron oscillation with the synchrotron frequency:

$$f_{\text{s}} = f_{\text{rev}} \sqrt{-\frac{eU_0 h \cos(\Psi_{\text{s}})}{2\pi \beta^2 E} \left(\alpha_{\text{c}} - \frac{1}{\gamma^2} \right)} , \tag{2.22}$$

where α_{c} denotes the momentum compaction factor (see the section below).

2.1.5. Low Alpha Mode

As explained above, the orbit of any particle with $\delta p \neq 0$ deviates from the synchronous particle's orbit. The relation between the relative deviation in the electron's orbit length:

$$\delta L = (L - L_{\text{s}})/L_{\text{s}} , \tag{2.23}$$

and the electron's relative momentum deviation δp is called momentum compaction factor:

$$\alpha_{\text{c}} = \frac{\delta L}{\delta p} . \tag{2.24}$$

Considering a single bunch, a small momentum compaction factor leads to small deviations of the longitudinal positions of the electrons inside the bunch and therefore to

(a) Electron bunch on its orbit   (b) Longitudinal bunch profile $\rho(z)$
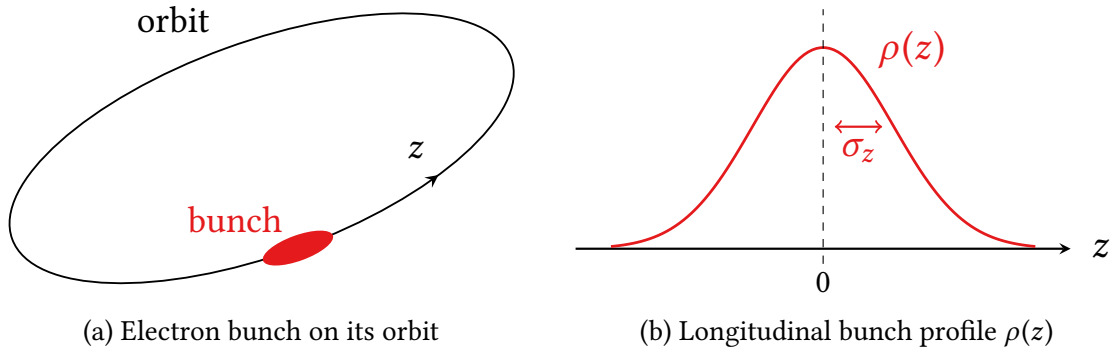
Figure 2.4.: (a) A bunch moves on its orbit, where z indicates the longitudinal axis parallel to the direction of motion. (b) The electron distribution along the z-axis is described by the longitudinal bunch profile $\rho(z)$, where $z = 0$ commonly refers to the position of the synchronous particle. Its standard deviation σ_z is called the bunch length.

a short bunch length σ_z. Here, the bunch length σ_z is defined as the standard deviation of the longitudinal electron distribution $\rho(z)$, also called longitudinal bunch profile (see Figure 2.4). Analogously, the energy profile $\rho(E)$ denotes the energy distribution of the electrons within the bunch and its standard deviation σ_E is called energy spread. The energy E and the longitudinal position z are commonly given with respect to the synchronous particle, i.e. the synchronous particle marks the axes origins ($z = 0$ and $E = 0$). Furthermore, the longitudinal position and the particle's energy span the longitudinal phase space. The longitudinal bunch profile and energy profile are the projections of the longitudinal phase space density $\varphi(z, E)$ on the respective axis, i.e.:

$$\rho(z) = \int \varphi(z, E) \mathrm{d}E \ . \tag{2.25}$$

Since the longitudinal form factor in Eq. (2.19) depends on the longitudinal bunch profile and therefore on the bunch length σ_z, the CSR power spectrum in Eq. (2.17) depends on σ_z as well. As a reduction of α_c leads to a decreasing bunch length, this can also be used to exert influence on the emitted synchrotron radiation. In practice, some synchrotron light sources are operated at low α_c to reduce the bunch length and therefore to enlarge the CSR spectrum (see Figure 2.2). This operation at low momentum compaction factor is achieved by appropriate settings of the accelerator's magnets and is called low alpha mode.

2.1.6. CSR Wake Field and Impedance

In the previous sections, the dependence of the emitted synchrotron radiation on the electron distribution within the bunch was treated. The dynamics of the electron bunch however, depend heavily on the electromagnetic interaction with the environment. In the time domain, this is described by the so-called wake field, the electromagnetic field propagating with the bunch. In the frequency domain, the interaction can be described by
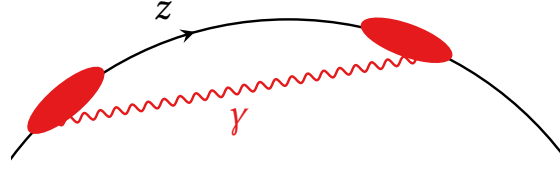
Figure 2.5.: An emitted electromagnetic wave propagating on a straight line has a marginally shorter path length than the electron bunch on its curved orbit. This enables the interaction of the electron bunch with its own synchrotron radiation, which is described by the CSR impedance.

a frequency-dependent impedance $Z(\omega)$. Together with the bunch current $I_{\text{bunch}}(\omega)$ this yields the induced voltage [15]:

$$V(\omega) = -I_{\text{bunch}}(\omega)\, Z(\omega) \; . \tag{2.26}$$

One example is the resistive wall impedance that describes the interaction of the electron bunch with the surrounding beam pipe. The pipe walls are neither completely homogeneous nor perfectly conducting. Moreover, the cross section might change due to specific machine requirements, e.g. a diagnostic device placed within the beam pipe, which is described by additional geometric impedances.

   Additionally, there can be an interaction of the electron bunch with its own emitted synchrotron radiation. This is due to the marginally shorter path length of an emitted electromagnetic wave propagating on a straight line compared to the curved orbit of the electron bunch (see Figure 2.5). This means, the synchrotron radiation emitted by the trailing part of the bunch catches up with the head of the bunch, and their interaction can especially influence the particle's energies. The interaction due to the coherently emitted part of the synchrotron radiation is described by the CSR impedance. Due to the complexity of an analytical description, approximations have been made to study the influence of the CSR impedance on the longitudinal beam dynamics. In the free space model, the CSR impedance merely describes this effect for electrons on a circular motion in a vacuum without any shielding. The parallel plates model additionally approximates the beam pipe by two infinitely extending parallel plates with distance g, and such describes the combined effects of the beam pipe walls and CSR interaction on the bunch. The longitudinal beam dynamics can then be studied by solving the Vlasov-Fokker-Planck equation, where the CSR impedance induces a perturbation to the Hamiltonian [13]:

$$\frac{\partial \widetilde{\varphi}}{\partial \Theta} + \frac{\partial H}{\partial p}\frac{\partial \widetilde{\varphi}}{\partial q} - \frac{\partial H}{\partial q}\frac{\partial \widetilde{\varphi}}{\partial p} = \frac{1}{f_{\text{s}}\tau_{\text{d}}}\frac{\partial}{\partial p}\left(p\widetilde{\varphi} + \frac{\partial \widetilde{\varphi}}{\partial p}\right) \; , \tag{2.27}$$

with the time-dependent normalized electron distribution $\widetilde{\varphi}(z, E, t)$, the time in multiples of synchrotron periods $\Theta = f_{\text{s}}t$, the normalized coordinates $q = z/\sigma_{z,0}$ and $p = (E - E_{\text{s}})/\sigma_{E,0}$, the Hamiltonian H and the damping time τ_{d}. The so-called natural bunch length $\sigma_{z,0}$ and natural energy spread $\sigma_{E,0}$ are defined by the equilibrium state that exists for small bunch currents.

2.1.7. THz-Bursting Phenomenon

In practice, one of the quantities that can actually be measured at the ANKA storage ring is the radiation power arriving at a detector. This includes in particular the radiated power over the THz frequency range, denoted by the THz-Power:

$$P_{\text{THz}} = \int_{\omega_1}^{\omega_2} \frac{\mathrm{d}P_{\text{tot}}}{\mathrm{d}\omega} r(\omega) \mathrm{d}\omega \,, \tag{2.28}$$

where $r(\omega)$ describes the detector response. This THz frequency range can be specified as e.g. $\omega_1/2\pi = 1\,\text{GHz}$ and $\omega_2/2\pi = 1\,\text{THz}$ and corresponds to the dimension of typical bunch lengths (see Figure 2.2). Especially during operation at low momentum compaction factor α_{c}, one observes a heavily fluctuating THz-Power signal. This is due to the above described interaction of the electron bunch with its CSR wake field, which causes a dynamically changing electron distribution $\varphi(z, E, t)$. For bunch currents I_{bunch} higher than the threshold I_{th}, this leads to the formation of micro-structures in the longitudinal phase space, which means that parts of the synchrotron radiation with wavelengths shorter than the bunch length σ_z are emitted coherently as well. These changes in the overall emitted CSR power:

$$P_{\text{csr}} = \int \frac{\mathrm{d}P_{\text{csr}}}{\mathrm{d}\omega} \mathrm{d}\omega \,, \tag{2.29}$$

is eventually what yields the time-dependent fluctuation of the THz-Power, also called THz-Bursting. It is worth noting, an emitted frequency of $\omega/2\pi = 1\,\text{THz}$ corresponds to bunch lengths or micro-structures in the order of $\sigma_z/c = 1\,\text{ps}$.
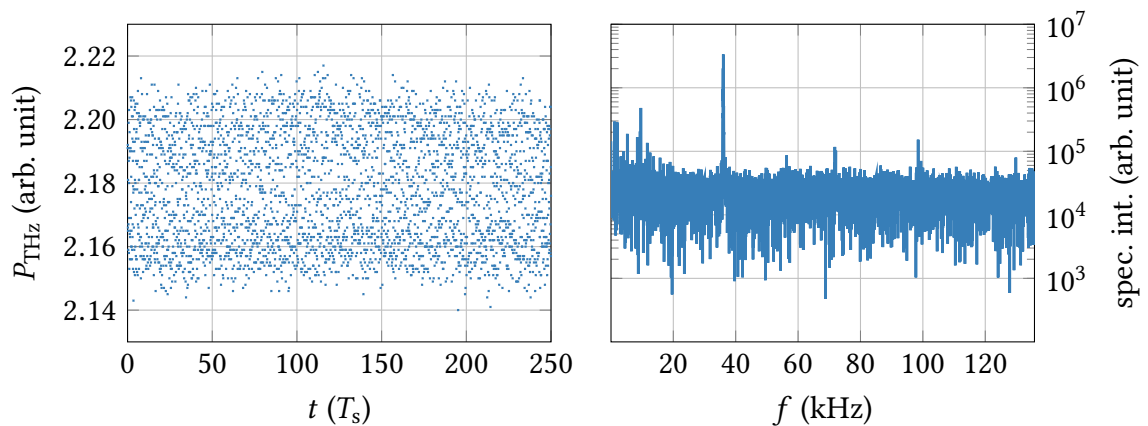
Figure 2.6.: (Left) The observed THz-Power signal P_{THz} above the threshold I_{th} is fluctuating. However, the fluctuations do not occur randomly, but with quite characteristic frequencies. (Right) This becomes apparent by examining its Fourier transform[2]. Data taken at ANKA, courtesy of Miriam Brosi.

By examining the Fourier transformed THz-Power signal (see Figure 2.6), it is apparent that the fluctuations do not occur utterly at random, but with quite characteristic frequencies. Especially right above the threshold I_{th}, the THz-Power oscillates primarily with

---

[2] In this thesis, if not otherwise specified, the absolute value of the Fourier transform is considered.

one specific frequency. The THz-Power spectrogram as shown in Figure 2.7, is generated by incorporating such Fourier transformed THz-Power signals for a range of different bunch currents. This is particularly useful for studying the current-dependency of these fluctuations. Below the threshold $I_{th} \approx 0.2\,\text{mA}$, the only clearly visible contributing frequencies are multiples of the synchrotron frequency $f_s = 9.8\,\text{kHz}$. Above I_{th} however, there is a distinct line at $f_{reg} \approx 35\,\text{kHz}$ and its higher harmonics $f = nf_{reg}$, with $n \in \mathbb{N}$. Due to the almost harmonic behavior this is called regular bursting regime for the context of this thesis. At higher bunch currents, there are contributions from much lower frequencies causing a sawtooth shaped THz-Power signal. Hence, in the following this is called sawtooth bursting regime, see e.g. Refs. [18], [19] and [20].

It is worth noting, that these characteristics are fairly well reproducible for fixed machine settings. However, for altered settings, e.g. a modified synchrotron frequency f_s, the THz-Power spectrogram might look slightly different. The most pronounced features, i.e. a distinct frequency beyond the respective bursting threshold and rather spread frequencies above with some low-frequency contributions, are yet always present.
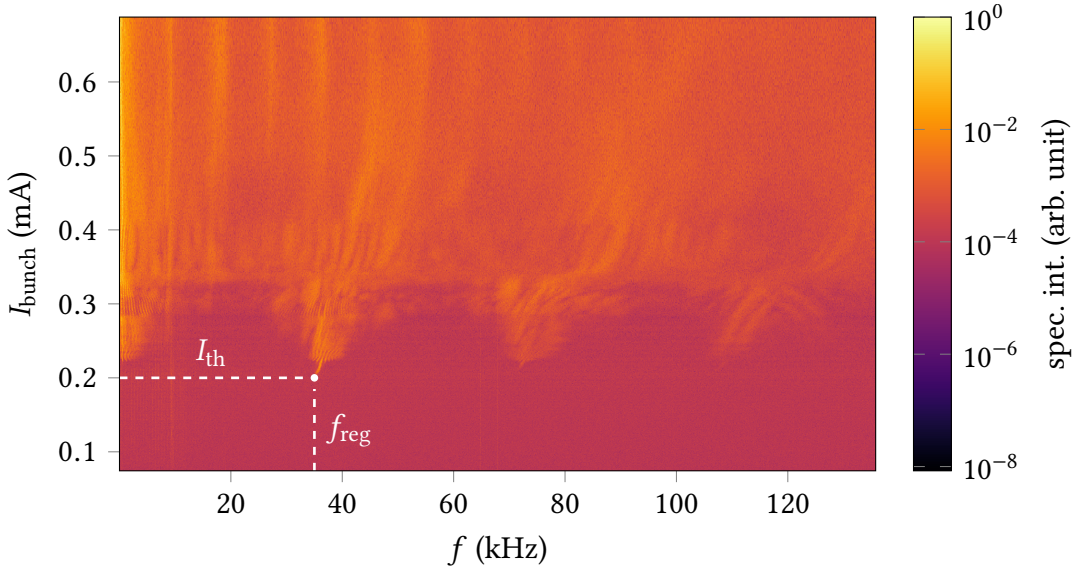
Figure 2.7.: Exemplary THz-Power spectrogram. The THz-Power signal P_{THz} for each bunch current I_{bunch} is Fourier transformed and plotted as a horizontal line in the above spectrogram with the color code indicating the intensity at that frequency. It is apparent, the fluctuations in the THz-Power signal are not occurring randomly, but with characteristic frequencies dependent on the respective bunch current. Directly above the bursting threshold I_{th}, the THz-Power oscillates with the distinct frequency f_{reg}. For higher bunch currents, more frequencies including some low frequencies at the left edge of the figure are significantly contributing. Data taken at ANKA, courtesy of Miriam Brosi.

Historically, first experimental observations of this phenomenon were made at the NSLS VUV storage ring [21]. It then has been systematically studied at various synchrotron light sources, e.g. ANKA [8], BESSY II [9], DIAMOND [10], MLS [11] and SOLEIL [6].

Furthermore, efforts have been made to simulate the dynamics and to predict the bursting threshold I_{th}, e.g. Refs. [5], [7] and [22]. As the simulation code employed in this thesis, Inovesa is introduced in Section 3.1.

2.2. Machine Learning

Machine learning emerged as a sub-field of computer science in the 1950s. It explores algorithms that enable computers to learn from data without being explicitly programmed [23]. The techniques derived in machine learning have been utilized for a large range of problems in various fields, e.g. financial systems, retail industry, telecommunication industry, genetics, climate and ecosystem modeling in geosciences and anomaly detection for computer security systems [24]. The variety of its application is enabled by the steadily rising accessible computing power as well as the increasing amounts of data being collected in several fields. Yet, the latter makes it often inevitable to resort to a computer-aided approach, given that solely manpower is either not sufficient or too expensive.

In this thesis, machine learning techniques have been employed in the data analysis to help understanding the characteristics of the data and gaining deeper insights into the underlying features.

2.2.1. Supervised and Unsupervised Learning

The field of machine learning can be separated into two main categories, supervised learning and unsupervised learning. While both of them incorporate the aim to achieve an appropriate categorization of a given data set, their approach is fundamentally different. A typical application of supervised learning looks like this: Given a training set of data containing objects whose category membership is known, a classification procedure is applied, in which a so-called classifier is trained to fit this data set and to correctly map a given object to its corresponding category. If over-fitting of the training set can be avoided, the classifier can also be used to predict the category of new objects. It is worth mentioning, in many cases the exact procedure by which the classification algorithm derives its predicted category can be difficult to pinpoint, even when the classifier is working quite well. Furthermore, a multitude of different classification algorithms exists, providing the opportunity to chose the most suitable for the given application. Regarding physics in particular, one established application of these classification algorithms is particle identification in the context of collider experiments [25].

In many cases it is not possible to access a large training set with known category memberships. Unsupervised learning deals with this problem. It does so by emphasizing the intrinsic structure, e.g. the density distribution of the data objects, to derive different categories within the data set. The categories are chosen to separate the data set into different groups, the so-called clusters, whereby objects within one cluster are more similar to each other than to those of other clusters. As it is not always apparent on which intrinsic structure emphasis should be put, various clustering algorithms have been developed for different applications.

supervised learning unsupervised learning
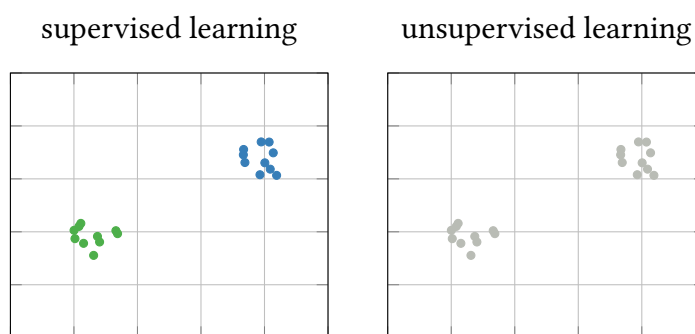
Figure 2.8.: Shown are initial data sets for the cases of supervised learning and unsupervised learning. Classification methods offer automated identification of new objects based on the provided information, i.e. the category membership of the data objects (green and blue dots). This means, given a new data object, its category membership (color) can be predicted. In contrast, clustering methods can be used as a tool of exploratory data analysis to reveal underlying structure. For the illustration above, this implies identifying the two separate groups of objects in the data set in the first place.

Classification methods as a type of supervised learning can be employed to offer automated identification of new objects based on the given information, whereas clustering methods as a type of unsupervised learning can be used as an exploratory tool in data analysis to reveal underlying structures. This is illustrated in Figure 2.8. In other words, classification is a form of learning by examples while clustering is a form of learning by observation [24]. Based on the given requirements and the data sets available in the content of this thesis, the latter has been chosen.

2.2.2. Clustering Method *k*-means

As one of the most well-known and extensively used among the various clustering methods, k-means has been adopted in this thesis. Introductions to the k-means method can be found in many common textbooks, e.g. Refs. [26] and [27]. In the following, the principle will be shortly introduced, based on the treatment in Ref. [24].

Considering a data set of n objects, the k-means method takes the number of clusters k as an input and partitions the n objects into k clusters aiming to maximize the similarity between objects within a cluster while minimizing those between objects from different clusters. The similarity measure here is defined in regard to the arithmetic mean of the objects within a cluster. These means, from which the method derives its name, can also be interpreted as the cluster centers, centroids or representatives. Standard implementations use an iterative approach as illustrated in Figure 2.9 and described in the following:

1. Initialization: Firstly, k arbitrary points in the given data space are chosen as initial cluster centers.

2. Assignment: Each object is then assigned to the cluster to which it has the most similarity, that is, where its distance to the respective cluster center is the smallest.

In practice, the cluster assignment is generally denoted by attaching a so-called label $y \in \{0, 1, \ldots, k-1\}$ to the object.

3. Update: Subsequently the cluster centers are updated by computing the mean of each newly formed cluster.

The assignment and update steps are repeated until some measure of convergence is reached, which is generally based on the minimization of the objective function J (also called the square-error criterion or inertia):

$$J = \sum_{i=1}^{k} \sum_{\boldsymbol{x} \in C_i} |\boldsymbol{x} - \boldsymbol{\mu}_i|^2 \, , \tag{2.30}$$

where C_i is the i-th cluster, $\boldsymbol{\mu}_i$ its corresponding mean and $\boldsymbol{x}$ represents the data objects. One possible condition to state the convergence of J can be expressed as:

$$\delta J = \frac{J_m - J_{m+1}}{J_m} \leq \varepsilon \, , \tag{2.31}$$

where J_m denotes the value of J after the m-th iteration. Minimizing J leads to the minimal within-cluster sum of squares, making the resulting k clusters as compact and separate as possible.

The computational complexity of the k-means algorithm is $O(nkt)$ with t being the number of iterations. This makes the algorithm efficient and scalable for applications on large data sets. Alongside the advantage of fast computation, implementations of this algorithm are widely established, e.g. Refs. [28], [29] and [30]. Furthermore, the results from the k-means algorithm are derived using procedures which can be very easily and intuitively understood. This fact is crucial for data mining applications that aim for deeper insights into not yet fully understood phenomena. As the k-means procedure is based on the calculation of cluster means, these can be used as reasonable representatives to analyze the found clusters. All these major advantages of the k-means algorithm define it as optimal choice for the purpose of this thesis.

It should be noted, the k-means algorithm can sometimes terminate at a local optimum, since it is highly dependent on the initial cluster centers. However, this effect can be mitigated by restarting the algorithm several times with different initializations (e.g. the seeding technique "kmeans++", as proposed by Arthur and Vassilvitskii [31] and implemented as default in the scikit-learn package [28] for Python employed for this thesis). Additionally, the k-means method is not suited for clusters of very different sizes or non-convex shapes. Furthermore, it can be prone to noise and outliers in the data set, as even small numbers of such data points can substantially influence the mean value, which this algorithm is based on. One fundamental aspect is the fact that the number of clusters k has to be chosen in advance. Though it might be seen as a disadvantage in some cases, it extended the understanding of the data in this thesis (see Chapter 4). The issue of finding the optimal value for k is further addressed in Section 4.3.
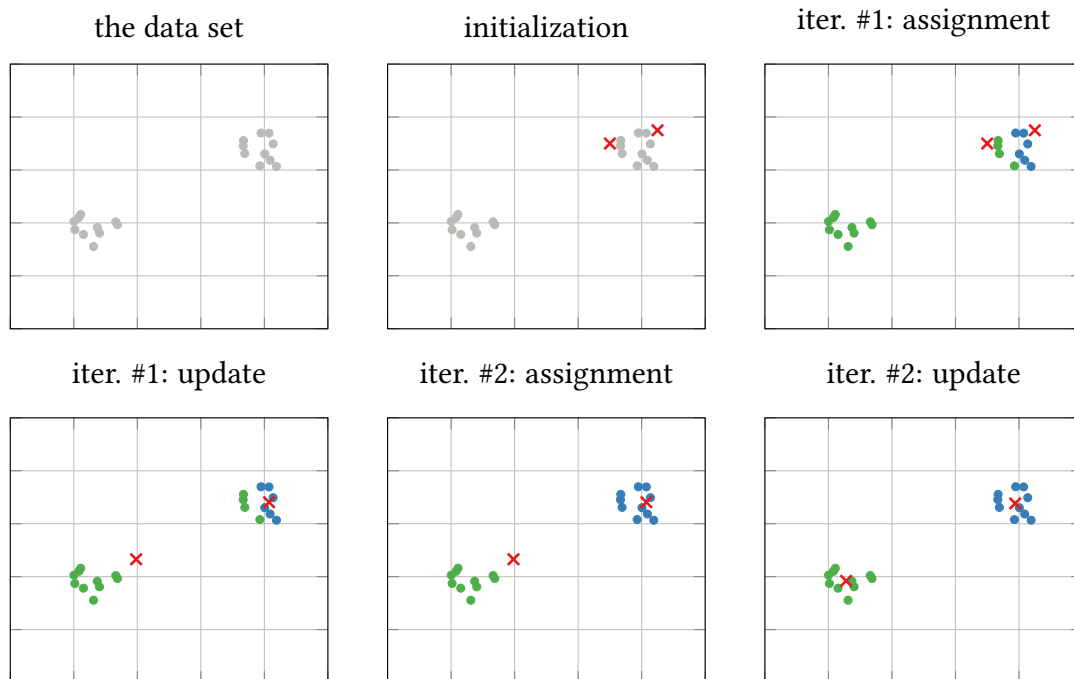
Figure 2.9.: Principle of the k-means algorithm. This example explains the procedures for the case of $k = 2$. (Upper left) A data set of objects with unknown categories is given. (Upper middle) Two initial cluster centers (red crosses) are randomly chosen. (Upper right) In the first iteration, each object is assigned to one of the clusters (green or blue dots) according to their distances to the cluster centers, (lower left) and then the means of the newly formed clusters are updated. (Lower middle and right) The assignment and update steps are iterated until convergence criteria is reached.

3. Simulation Procedure and Methods

Besides a brief description of the used simulation code Inovesa, this chapter provides an overview of the simulation settings used to generate the data sets for this thesis. Subsequently, the general idea of the k-means application within the context of this thesis is described. The final section explains the pre-processing procedure applied in preparation for the data analysis in Chapters 4 and 5.

3.1. Simulation Code Inovesa

As mentioned in Section 2.1.6, the longitudinal dynamics of an electron bunch in a storage ring can be studied by solving the Vlasov-Fokker-Planck equation. The self-interaction of the bunch with its wake field can be added as a perturbation to the Hamiltonian. Inovesa (Inovesa Numerical Optimized Vlasov-Equation Solver Application), which was developed within the THz radiation research group at IBPT, KIT by Patrik Schönfeldt [13], is a simulation code that solves the Vlasov-Fokker-Planck equation numerically. Besides the CSR self-interaction, several other dynamic aspects are modeled, including the synchrotron oscillation, radiation damping and diffusion. It does so using OpenCL to massively parallelize the computation and therefore speed up run-time. This enables the application to run on a standard desktop PC. Specifically, the longitudinal dynamics are approximated by calculating the longitudinal phase space densities $\varphi(z, E, t_i)$ for a sequence of discrete time steps t_i. Therefor, it uses an iterative approach where each longitudinal phase space density $\varphi(z, E, t_i)$ is calculated based on that for the previous time step $\varphi(z, E, t_{i-1})$.

It should be noted, in the following, t_i is used to denote the discrete sequences of the simulated quantities, e.g. $P_{\text{csr}}(t_i)$ describes the sequence of CSR power values for the different simulation time steps t_i with $i \in \{1, 2, \ldots, n_{\text{steps}}\}$, while $P_{\text{csr}}(t)$ denotes the theoretically continuous signal or an actual measurement.

One essential finding for the content of this thesis is the extent to which Inovesa can model the THz-Bursting behavior described in Section 2.1.7, when approximating the shielding effects by two parallel plates. As the incoherent synchrotron radiation does merely yield a constant contribution to the THz-Power in Eq. (2.28), it is sufficient to exclusively focus on the CSR power to study the dynamics. The simulated CSR power spectrogram in Figure 3.1 does not only show the threshold I_{th}, but also the different regimes of CSR emission above that. This is taken as the foundation for the following investigation of the underlying micro-structure dynamics and their correlation to the emitted CSR.
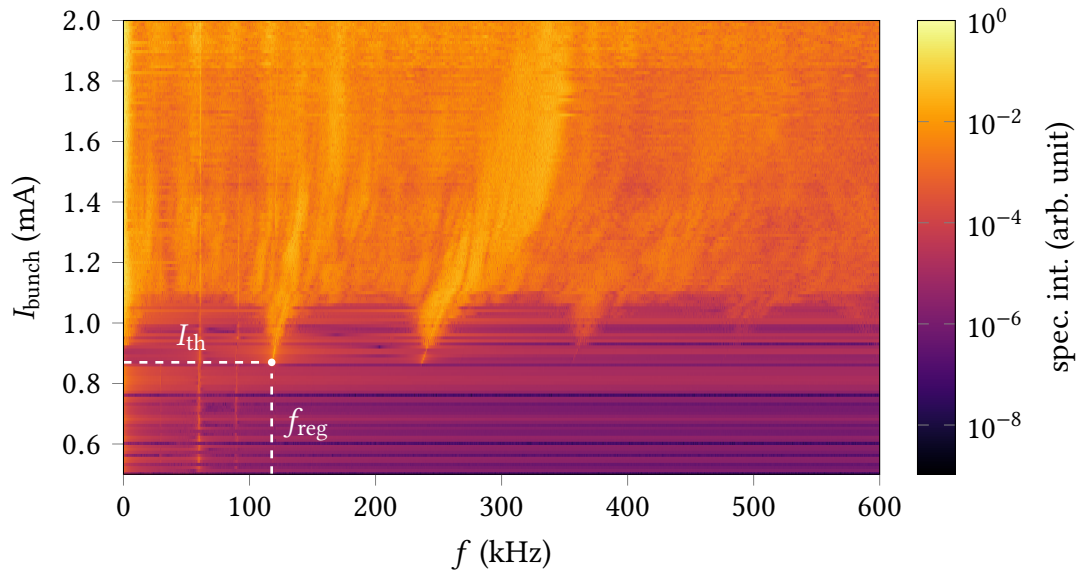
Figure 3.1.: Shown is a simulated CSR power spectrogram. Analogously to the THz-Power spectrogram in Figure 2.7, the CSR power signal P_{csr} for each bunch current I_{bunch} is Fourier transformed and plotted as a horizontal line. Not only the threshold I_{th} is clearly visible, but also different regimes of CSR emission above that are represented. The simulation settings for this CSR power spectrogram can be found in Table 3.1.

3.2. Simulation Settings

While several different data sets were generated and studied, one particular data set is analyzed in-depth for the main part of this thesis. In the following, the simulation settings used to generate this data set are discussed.

Inovesa provides a variety of tunable physical parameters, which are listed in Table 3.1. Additionally, there are several control parameters that influence e.g. accuracy and runtime. This includes the grid size $n_{grid} = 256$ determining the discretization of the longitudinal phase space $\varphi(z, E, t)$. That is, the z-axis and E-axis are specified at n_{grid} points respectively, with the equidistant axes step sizes Δz and ΔE. This renders the longitudinal phase space density $\varphi(z, E, t_i)$ for each time step t_i, into a 256×256 matrix. The amount of simulation steps during the simulation time t is set to $n_{steps} = 10\,000$.

One issue with numerical Vlasov-Fokker-Planck-Solvers is, that the initial electron distribution $\varphi(z, E, t_0)$ can not be calculated analytically and has to be chosen manually. This means, there is a transition oscillation before a physical state with the desired accuracy is reached, as illustrated in Appendix A.1. To deal with this issue, the simulated data for a time period of $t_{transition} \approx 1000\,T_s$ is neglected before the actual data set for a duration of $t = 250\,T_s$ is generated.

The simulated bunch currents I_{bunch} are varied from $0.5\,\text{mA}$ to $2.0\,\text{mA}$, with an equidistant step size of $\Delta I_{bunch} = 0.01\,\text{mA}$. This accumulates to a total of 151 simulated bunch

currents in this data set and therefore to about 1.5 million longitudinal bunch profiles. Together with the 1.5 million corresponding longitudinal phase space densities $\varphi(z, E, t_i)$, this yields roughly 1 TB of data for these simulated settings alone. This illustrates the difficulties of the following analysis and motivated the idea of employing machine learning techniques for this thesis.

Table 3.1.: Simulation parameters used to generate the main data set for this thesis. Besides a variety of tunable physical parameters, Inovesa provides several control parameters to manipulate runtime and accuracy. For the given settings, multiple bunch currents I_{bunch} between 0.5 mA and 2.0 mA are simulated. In order to deal with the transition oscillation mentioned in Section 3.2, the simulated data for a time period of $t_{transition} \approx 1000 \, T_s$ is neglected, before the actual data set is generated.

Physical parameter	Value
RF voltage U_0	1 MV
revolution frequency f_{rev}	9 MHz
synchrotron frequency f_s	30 kHz
damping time τ_d	5 ms
harmonic number h	50
parallel plates distance g	3.2 cm
initial electron distribution $\varphi(z, E, t_0)$	2-dim. Gaussian
simulation time t	250 T_s
bunch current I_{bunch}	0.5 mA to 2.0 mA

Control parameter	Value
grid size n_{grid}	256
time steps n_{steps}	10 000

3.3. Application of *k*-means

According to Eq. (2.25), each longitudinal phase space density $\varphi(z, E, t_i)$ yields a longitudinal bunch profile $\rho(z, t_i)$. With the aforementioned parameter settings this accumulates to $n_{steps} = 10\,000$ longitudinal bunch profiles for every simulated bunch current I_{bunch}. This is the set of data to which the in Section 2.2.2 introduced *k*-means method is applied. The general idea is to use *k*-means as a data mining tool for discovering the dominant micro-structures within the set of longitudinal bunch profiles $\rho(z, t_i)$ with a fixed bunch current I_{bunch}. In order to achieve that, the *k*-means method is applied to the data space spanned by the longitudinal bunch profiles with a specific current I_{bunch}. This is done for each of the 151 bunch currents while searching for $k = 2$ to $k = 6$ clusters. By employing the scikit-learn package [28], this can be implemented in Python, which is also

used for the major part of the following analysis. Subsequently, it is essential to correlate the results of the k-means application with the respective CSR power signal. As this is not an ordinary application of the clustering method, a considerable part of this thesis is dedicated to the exploration of possible evaluation techniques of the findings provided by the k-means method. As is shown in Section 5.1, this procedure can instead be applied to the energy profiles as well. However, due to the direct dependence of the emitted CSR on the longitudinal form factor, as explained in Eq. (2.19), it is primarily focused on the longitudinal bunch profiles.

3.4. Pre-Processing

While the data generated by Inovesa is of very low noise, there is one issue that has to be addressed to improve the performance of the above explained application of the k-means method. As mentioned in Section 2.1.4, there is the synchrotron oscillation along the longitudinal z-axis. This means, the longitudinal bunch profiles shift periodically along the z-axis against the origin $z = 0$, which is the position of the synchronous particle. Especially for low bunch currents, where the micro-structures are barely noticeable, the synchrotron oscillation can dominate the longitudinal dynamics of interest. The upper part of Figure 3.2 shows the results of an application of k-means with $I_{\text{bunch}} = 0.88\,\text{mA}$ and $k = 2$ on the raw data provided by Inovesa. Displayed are the arithmetic means of the found clusters, also called cluster centers. As aforementioned, these can be used as representatives in order to analyze the actual clusters found by the k-means method. Compared to each other, the two cluster centers are marginally shifted along the longitudinal axis. Since for this thesis, the major concern is the dynamics caused by micro-structures in the longitudinal phase space and its correlation to the emitted CSR, the influence of the synchrotron oscillation on the results of the k-means method has to be mitigated. This is achieved by re-centering all longitudinal bunch profiles to their respective center of mass position, i.e. the expectation value of the longitudinal electron distribution:

$$\mu_z = \frac{\sum_{i=1}^{n_{\text{grid}}} z_i\, \rho(z_i)}{\sum_{i=1}^{n_{\text{grid}}} \rho(z_i)}\ . \tag{3.1}$$

Given the such applied shifts are not always multiples of the z-axis step size Δz chosen by Inovesa, a linear interpolation is employed. In this process the number of data points describing the longitudinal bunch profile is reduced to $n_{\text{grid}} = 200$ by neglecting the very edges of the electron distribution with $\rho(z) \approx 0\,\text{pC/ps}$. The lower part of Figure 3.2 shows the results of the k-means application after this re-centering procedure. Now, the two re-centered cluster centers start to show some modulations on the longitudinal bunch profiles. Due to the comparatively small amplitude of the micro-structures, the deviations of the two cluster centers are marginal, which makes the visualization of these micro-structures one of the difficulties of the subsequent analysis.
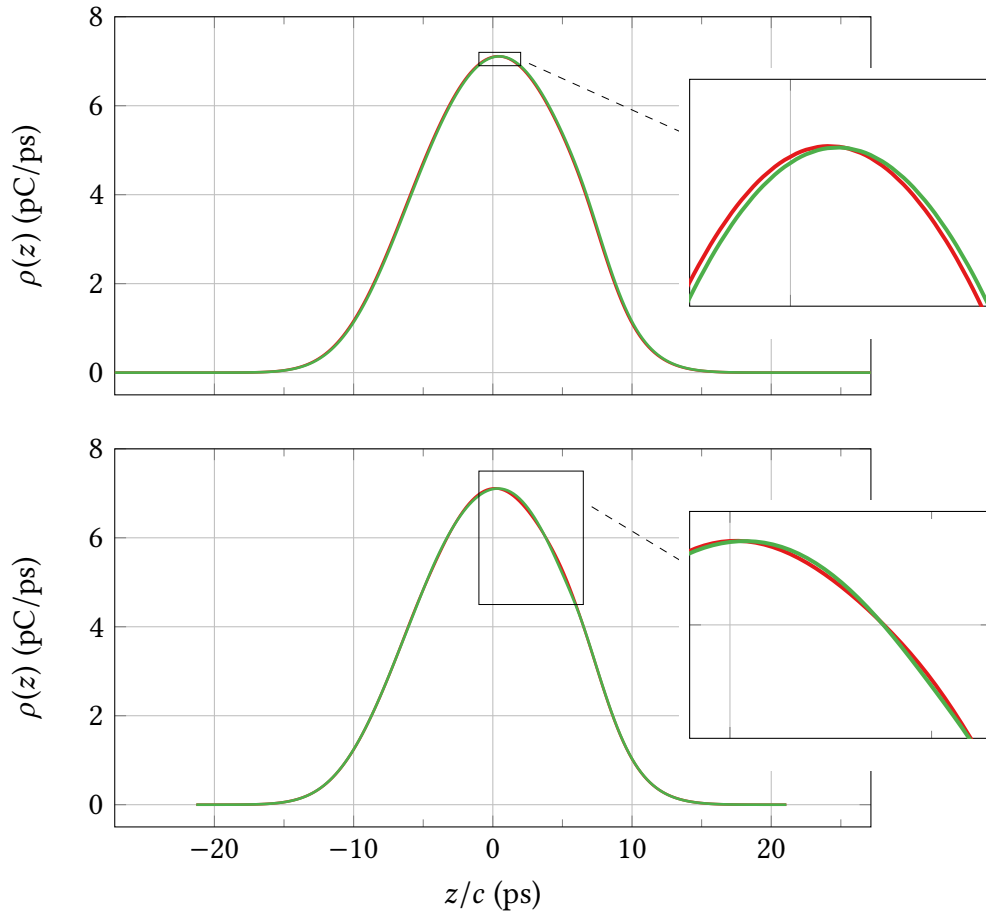
Figure 3.2.: (Top) Shown are the two cluster centers found by the *k*-means method for $k = 2$ when applied to the $n_{\text{steps}} = 10\,000$ longitudinal bunch profiles with bunch current $I_{\text{bunch}} = 0.88\,\text{mA}$. Compared to each other, the cluster centers are marginally shifted along the *z*-axis. This is due to the synchrotron oscillation discussed in Section 2.1.4 and has to be mitigated by a re-centering procedure. (Bottom) After this re-centering procedure, the new cluster centers display small modulations on the longitudinal bunch profiles.

4. Analysis of Micro-Structure Dynamics

In the first part of this chapter, the previously mentioned applications of the k-means method on the longitudinal profiles at a fixed bunch current I_{bunch} are studied in order to understand the dynamics within a single current. The results are shown for two exemplary bunch currents $I_{reg} = 0.88$ mA and $I_{saw} = 1.15$ mA, as illustrated in Figure 4.1. These show the differences of the regular and sawtooth bursting regime as defined in Section 2.1.7. Besides different ways of visualization, evaluation methods for the found clustering results are explored, considering especially the correlation of the found micro-structures with the respective CSR power signal. Within this context, the question for the optimal cluster number k, as raised in Section 2.2.2, is further addressed. Moreover, the scale of the found micro-structures and their current-dependent dynamics are systematically studied by analyzing the amplitude and frequency of the associated modulation on the longitudinal bunch profile. Finally, the chapter concludes by discussing the idea of generating a spectrogram analogously to Figure 2.7 and Figure 4.1 using the categorical cluster label information instead of the THz-Power or CSR power signals.

Figure 4.1.: Spectrogram of the simulated CSR power. For the subsequent analysis of the results of the k-means method, the two exemplary bunch currents $I_{reg} = 0.88$ mA and $I_{saw} = 1.15$ mA are chosen, as highlighted by the two horizontal white lines. These are used as an example to show the differences between the regular and sawtooth bursting regime.

For the Chapters 4 and 5, a consistent color scheme is kept serving as a guidance through the different results. This means that results belonging to a found cluster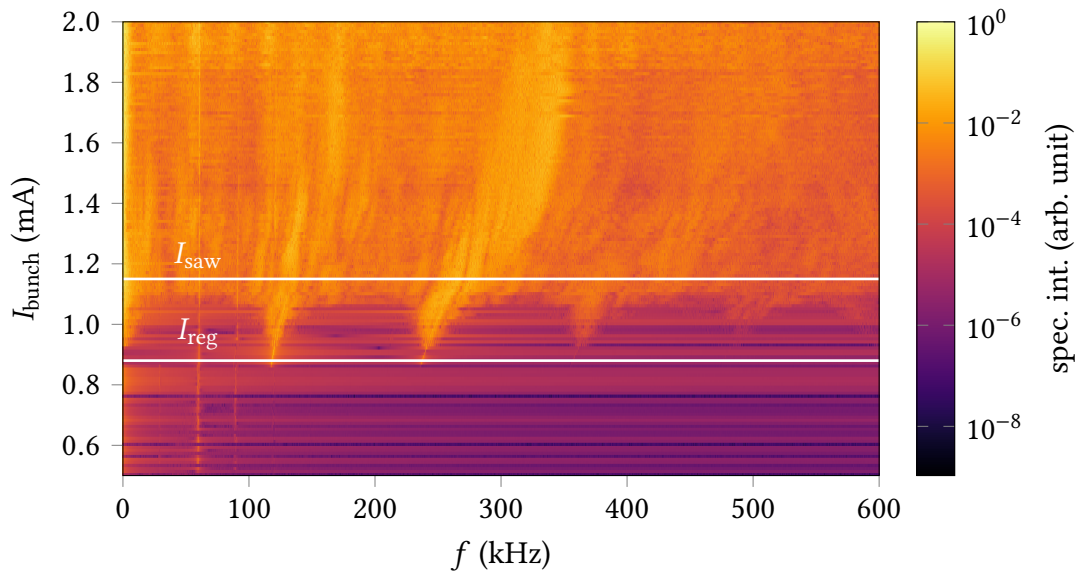 with the specific label y, are always colored the same way, as shown in Table 4.1. However, it should be noted, every application of the k-means method with modified bunch current I_{bunch} or altered cluster number k yields a new independent mapping of the clusters to their associated labels. This means, the cluster label y and therefore the particular color is only sufficiently defined by fixed bunch current I_{bunch} and fixed cluster number k.

Table 4.1.: Throughout the Chapters 4 and 5 a consistent color scheme is kept, which means a specific label y is always mapped to the same color. The cluster label y however, is only sufficiently defined by fixed bunch current I_{bunch} and fixed cluster number k. This means, the cluster with label y from the clustering results using the cluster number k does not relate to the cluster with the same label y found when searching for a different number of clusters k'.

cluster label y	0	1	2	3
assigned color	red	green	blue	orange

4.1. Regular Bursting Regime

In the following, the results of the k-means method applied on the re-centered longitudinal bunch profiles with the bunch current $I_{reg} = 0.88\,\text{mA}$ are analyzed. The obtained findings are correlated to the corresponding CSR power signal. Additionally, the discovered modulations on the longitudinal bunch profiles are explicitly associated with micro-structures in the longitudinal phase space. Moreover, their dynamics in the longitudinal phase space are studied. Finally, a simple toy study modeling the found dynamics in the regular bursting regime is presented.

4.1.1. Visualization of Micro-Structures

In the upper part of Figure 4.2, the cluster centers:

$$\overline{\rho}_{\text{C}}(z) = \frac{1}{n_{\text{cluster}}} \sum_{\rho(z,t_i) \in C} \rho(z, t_i)\,, \tag{4.1}$$

found by the k-means method searching for $k = 2$ clusters in the re-centered longitudinal bunch profiles for the case of $I_{reg} = 0.88\,\text{mA}$ are shown. Now, after the previously explained re-centering procedure, one observes small modulations around the center of mass position ($z = 0$). However, for this form of visualization, the cluster centers' differences are barely visible to the unaided eye. This is one of the issues that needed to be solved in the context of this thesis.
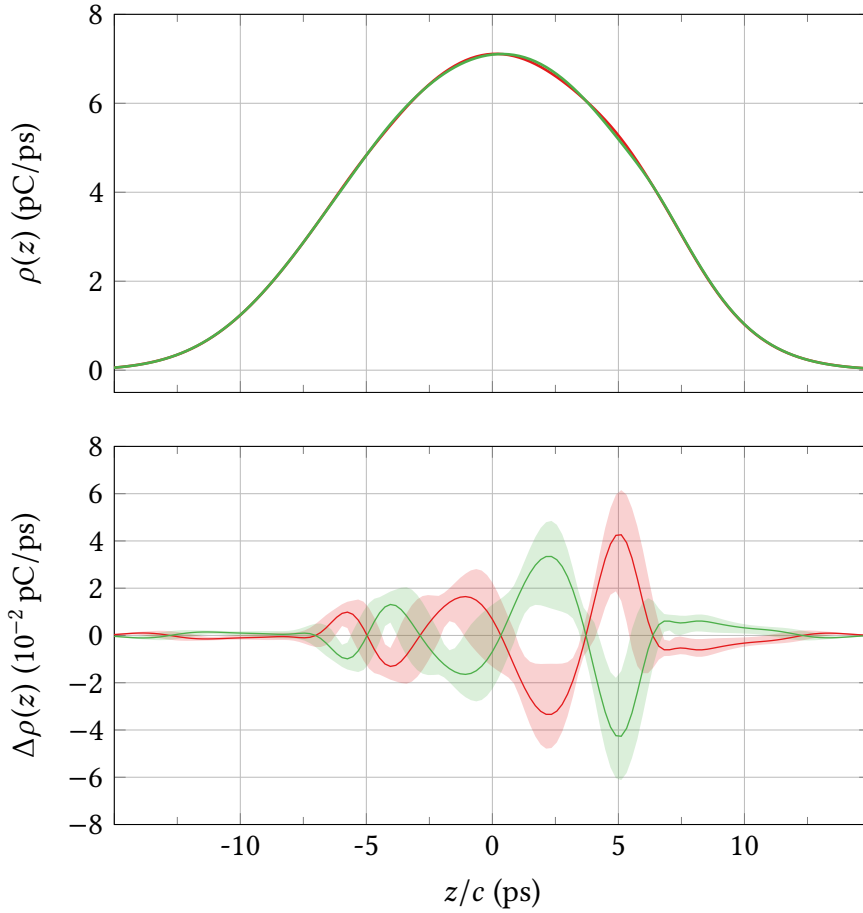
Figure 4.2.: The global mean of the longitudinal bunch profiles with this bunch current $\overline{\rho}(z)$ is subtracted from the cluster centers $\overline{\rho}_{\mathrm{C}}(z)$ displayed in the upper part of the figure. This highlights the found modulation and enables the examination and analysis by the unaided eye (lower part of the figure). The shaded areas denote the standard deviations of the cluster centers within their respective cluster, while treating deviations to higher and lower values separately.

An elegant way to emphasize these modulations, is to reference each longitudinal profile $\rho(z, t_i)$ to the global mean of the longitudinal profiles with this bunch current:

$$\overline{\rho}(z) = \frac{1}{n_{\mathrm{steps}}} \sum_{i=1}^{n_{\mathrm{steps}}} \rho(z, t_i) \,. \tag{4.2}$$

The such obtained difference:

$$\Delta\rho(z, t_i) = \rho(z, t_i) - \overline{\rho}(z) \,, \tag{4.3}$$

can also be calculated for the cluster means in Eq.(4.1) and is shown in the lower part of Figure 4.2. Here, the cluster centers are clearly distinguishable and display a distinct modulation on the longitudinal profiles. The shaded areas denote the standard deviations

of the longitudinal profiles within the respective cluster, while treating deviations to higher and lower values separately. They are used to analyze, to which degree the cluster centers concur with the actual longitudinal profiles in the respective cluster. This is quite reasonable, given the cluster centers are statistical quantities rather than actual longitudinal bunch profiles.

In the regular bursting regime, the application of the k-means method with $k = 2$ yields two clusters of roughly equal size, i.e. they both contain about $n_{\text{cluster}} \approx 5000$ longitudinal profiles. The corresponding cluster centers represent the phase and paraphase of a distinct modulation on the longitudinal bunch profiles. It should be noted, the amplitude of this roughly sinusoidal modulation is not a constant along the z-axis. Instead the modulation is much more prominent near the head of the electron bunch ($z > 0$) compared to its trailing part ($z < 0$). This is expected due to the nature of the interaction with its own CSR wake field, described in Section 2.1.6. In fact, the subtracted global mean $\overline{\rho}(z)$ is slightly skewed in positive z-direction as well. Additionally, it should be noted that despite the overall sinusoidal shape, there are different frequencies, i.e. different period lengths present.
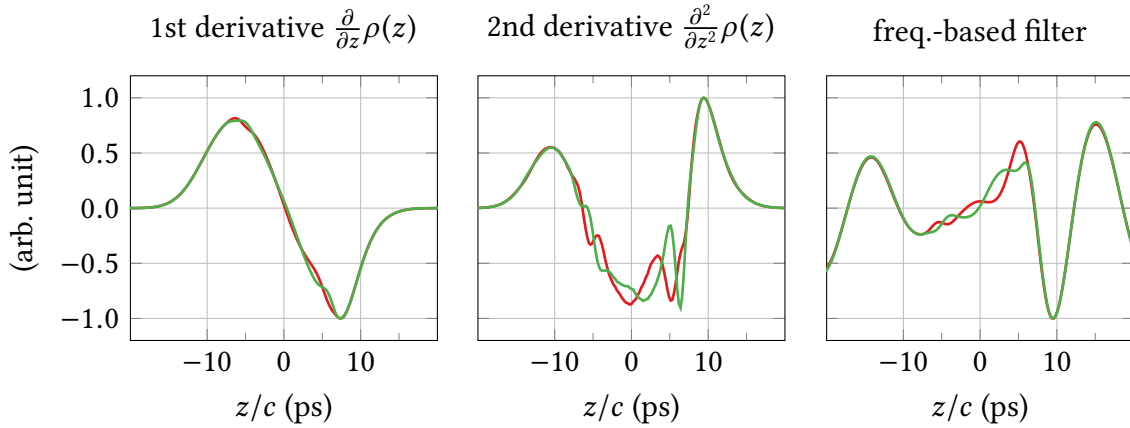
Figure 4.3.: The modulations on the longitudinal profiles are visualized using the first and second derivatives of the cluster centers (left and middle) or by applying a frequency-based filter (right).

Besides the previously illustrated procedure, several other visualization methods have been explored. Figure 4.3 shows the first and second derivatives of the original cluster centers $\overline{\rho}_{\text{C}}$ as well as the results of a frequency-based filter. The second derivative and the results of the frequency-based filter verify the existence of this modulation with its phase and paraphase. However, for the context of this thesis, referencing the cluster centers $\overline{\rho}_{\text{C}}(z)$ to the global mean $\overline{\rho}(z)$ was found to yield the most distinct results. Additionally, one major advantage compared to the application of a frequency-based filter is that there are no cut-off frequencies which have to be manually chosen dependent on the bunch current and the longitudinal profiles at hand. Yet, for the case of $I_{\text{reg}} = 0.88\,\text{mA}$, the frequency content of the modulation overlaps with that of the approximately Gaussian shape of the longitudinal profiles, i.e. they can not be distinctly separated by choosing particular cut-off frequencies. Moreover, due to the multitude of contributing frequencies and the small amplitude of the targeted modulation, it is easily possible to neglect the actual structure

by focusing on another frequency range instead and to wrongly interpret these findings as actual modulations caused by micro-structures in the longitudinal phase space. It is worth mentioning, subtracting a Gaussian fit instead of the global mean $\overline{\rho}(z)$ is not very beneficial due to the major differences of the longitudinal profiles to a purely Gaussian shape, which can exceed the differences caused by the targeted modulations considerably.
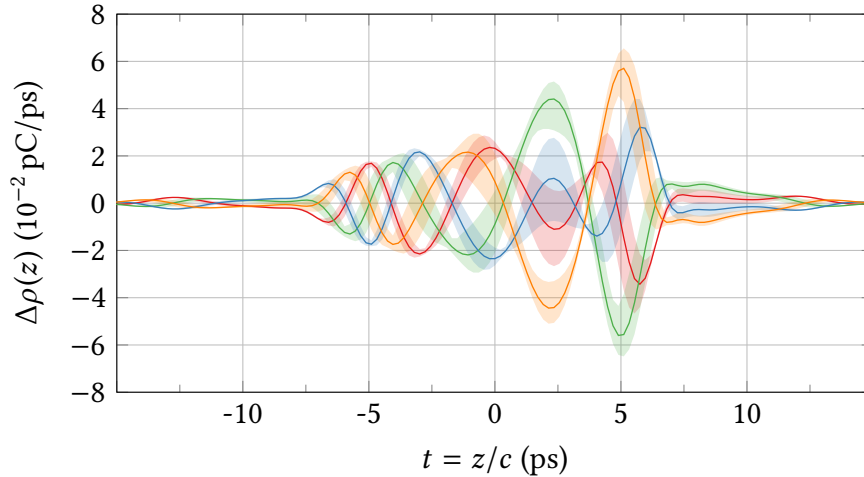
Figure 4.4.: Shown are the differences of the cluster centers for $I_{reg} = 0.88\,\mathrm{mA}$ and $k = 4$ to the global mean of the longitudinal bunch profiles with this bunch current $\overline{\rho}(z)$. Compared to the results for $k = 2$ in Figure 4.2, this yields two intermediate states (red and blue) between the phase and paraphase of the found modulation. The reapplication of the k-means method with modified cluster number k leads to a changed mapping of the found clusters to their associated labels and therefore to the altered coloring.

An application of the k-means method with increased number of clusters k yields additional intermediate states between the phase and paraphase of the found modulation. This is illustrated in Figure 4.4, where the resulting cluster centers for $k = 4$ after subtraction of the global mean $\overline{\rho}(z)$ are shown. The additional red and blue intermediate states correspond to the cluster labels $y = 0$ and $y = 2$ and display a phase and paraphase as well, though with slightly lower amplitude. The respective clusters contain roughly $n_{cluster} \approx 1800$ longitudinal profiles $\rho(z, t_i)$, while the green ($y = 1$) and orange ($y = 3$) cluster have almost twice this size $n_{cluster} \approx 3200$. Although the new cluster centers display slightly different frequencies, the dynamics of the longitudinal bunch profiles in the regular bursting regime can be surprisingly well approximated by a sinusoidal standing wave oscillating with frequency f_{reg} (see Section 2.1.7) which is added as a modulation to the stationary global mean $\overline{\rho}(z)$, as illustrated in Section 4.1.4.

4.1.2. Correlation with Emitted CSR

As illustrated in the previous section, the application of the k-means method for the case of $I_{reg} = 0.88\,\text{mA}$ yields cluster centers that display quite distinct sinusoidal modulations on the longitudinal profiles. However, in order to gain additional insights to the actual clusters' distributions, further steps have to be taken.
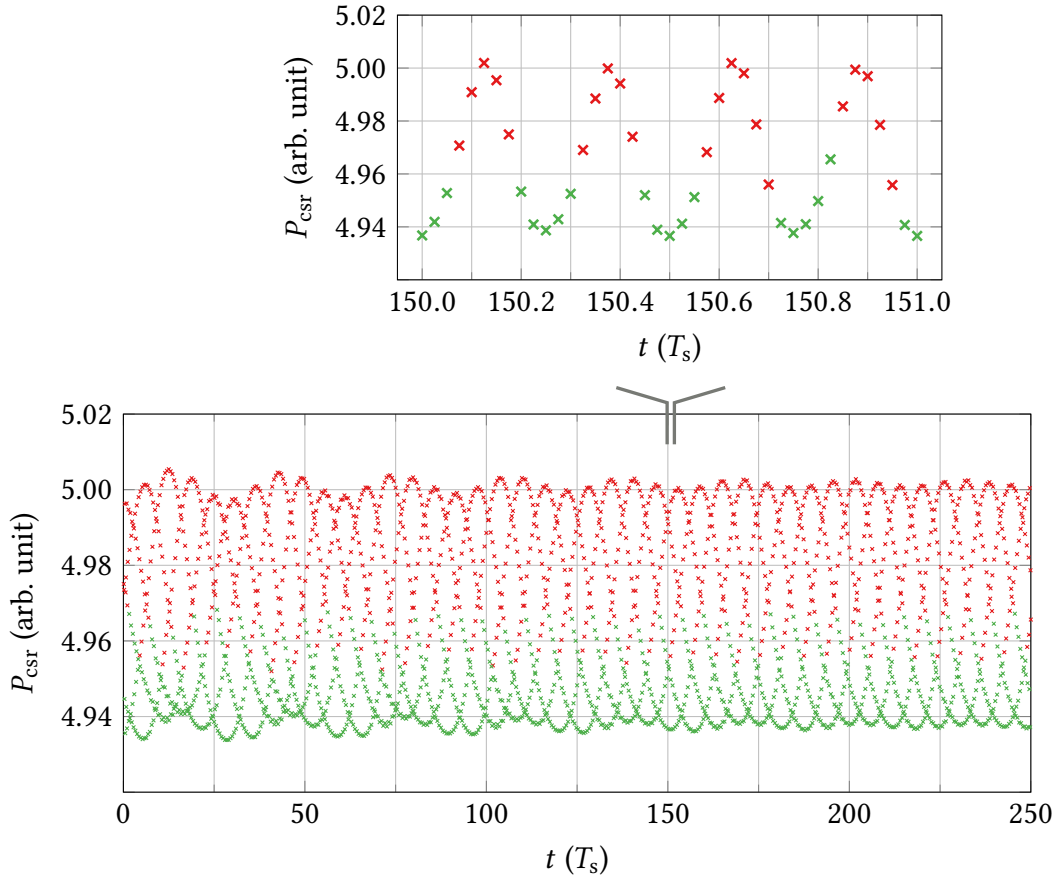
Figure 4.5.: The discrete time signal of the CSR power $P_{csr}(t_i)$ provided by Inovesa can be mapped to the sequence of cluster labels $y(t_i)$. For this illustration, each value of $P_{csr}(t_i)$ is colored according to its corresponding cluster label $y(t_i)$. Apparently, the sequence of the found cluster labels $y(t_i)$ is strongly correlated to the emitted CSR power $P_{csr}(t_i)$. Compared to each other, the red cluster center in Figure 4.2 corresponds to longitudinal profiles with higher emitted CSR power $P_{csr}(t_i)$, while the green cluster center corresponds to longitudinal profiles with lower CSR power $P_{csr}(t_i)$. To highlight the sinusoidal oscillation of the CSR power $P_{csr}(t_i)$, a short section is expanded and displayed in the upper part of the figure.[1]

---

[1] For the illustration of the CSR power signal $P_{csr}(t_i)$ from $t = 0$ to $t = 250\,T_s$, the number of points is reduced from $n_{steps} = 10\,000$ to roughly $n_{steps} \approx 4000$.

Especially the temporal structure of the found categorization is of interest, as this provides the opportunity to correlate the clustering results with the corresponding time signal of the CSR power $P_{\mathrm{csr}}(t_i)$.

During the k-means procedure each longitudinal profile $\rho(z, t_i)$, corresponding to the specific time step t_i, is assigned with a label $y(t_i)$. This temporal sequence of integers $y(t_i)$ contains the entire information about the generated clustering results. The emitted CSR power $P_{\mathrm{csr}}(t_i)$ for each longitudinal profile $\rho(z, t_i)$ is calculated according to Eqs. (2.17) and (2.29) and provided by Inovesa. The thus obtained sequence $P_{\mathrm{csr}}(t_i)$ can be mapped, via the longitudinal profiles $\rho(z, t_i)$, to the sequence of cluster labels $y(t_i)$. This is illustrated in Figure 4.5 for the case of $k = 2$, where each value of $P_{\mathrm{csr}}(t_i)$ is colored according to its corresponding cluster label $y(t_i)$.

The temporal sequence of the cluster labels $y(t_i)$ shows a definite correlation to the corresponding discrete time signal of the CSR power $P_{\mathrm{csr}}(t_i)$. Compared to each other, the red phase of the modulation in Figure 4.2 causes a higher value of the emitted CSR power $P_{\mathrm{csr}}(t_i)$ than its green paraphase. This is due to the fact that the actual modulation, displayed by $\Delta\rho(z)$, sits on top of the roughly Gaussian shaped global mean $\overline{\rho}(z)$.

Due to the length of the simulated t-axis compared to the regular bursting frequency f_{reg}, the sinusoidal oscillation of the CSR power $P_{\mathrm{csr}}(t_i)$ is barely recognizable in the lower part of the figure. Therefore, a short section is expanded and shown again above. Here, the regular behavior and its correlation to the cluster labels $y(t_i)$ become apparent.

As previously illustrated, an application of the k-means method with increased cluster number k yields cluster centers that display additional intermediate states between the phase and paraphase of the sinusoidal modulation (see Figure 4.4). Due to the lower amplitude of these intermediate states, the corresponding values of the discrete CSR power signal $P_{\mathrm{csr}}(t_i)$ are located more closely to the average value at $\overline{P}_{\mathrm{csr}} \approx 4.97$. The blue cluster in Figure 4.4 contains longitudinal profiles with higher CSR power values than the red cluster in Figure 4.4.

4.1.3. Longitudinal Phase Space

Since the longitudinal bunch profiles $\rho(z, t_i)$ and therefore the previously illustrated cluster centers $\overline{\rho}_{\mathrm{C}}(z)$ are the projections of the longitudinal phase space density $\varphi(z, E, t_i)$, the found micro-structures can additionally be studied directly in the longitudinal phase space. One way to do so, is to calculate the mean phase space density of the found clusters:

$$\overline{\varphi}_{\mathrm{C}}(z, E) = \frac{1}{n_{\mathrm{cluster}}} \sum_{\rho(z,t_i) \in C} \varphi(z, E, t_i) \ . \tag{4.4}$$

The left column of Figure 4.6 shows the such obtained results for the case of $k = 2$. However, the micro-structures are once more barely identifiable for this form of visualization. Analogously to the procedure applied to the longitudinal profiles, the global mean of the phase space densities is calculated:

$$\overline{\varphi}(z, E) = \frac{1}{n_{\mathrm{steps}}} \sum_{i=1}^{n_{\mathrm{steps}}} \varphi(z, E, t_i) \ , \tag{4.5}$$

and subtracted from the individual phase space densities:

$$\Delta\varphi(z, E, t_i) = \varphi(z, E, t_i) - \overline{\varphi}(z, E) . \qquad (4.6)$$

Applying this procedure to the phase space cluster means $\overline{\varphi}_C(z, E)$ in Eq. (4.4) yields the results shown in the right column of Figure 4.6. Here, several distinct micro-structures are visible. It should be noted, below the plane $\Delta\varphi(z, E) = 0$, there exist just as many minima with roughly the same amplitude as the visible maxima above $\Delta\varphi(z, E) = 0$, as indicated by the limits of the $\Delta\varphi$-axis. By comparing with Figure 4.2, it becomes clear that the highest values in the amplitude of the modulation on the longitudinal profiles originate from multiple maxima in the corresponding longitudinal phase space densities $\Delta\varphi(z, E, t_i)$ that get added up in the projection on the z-axis. For example, the highest value of the red cluster center referenced to the global mean $\overline{\rho}(z)$ in Figure 4.2 corresponds to the two maxima near the E-axis in the upper right of Figure 4.6.
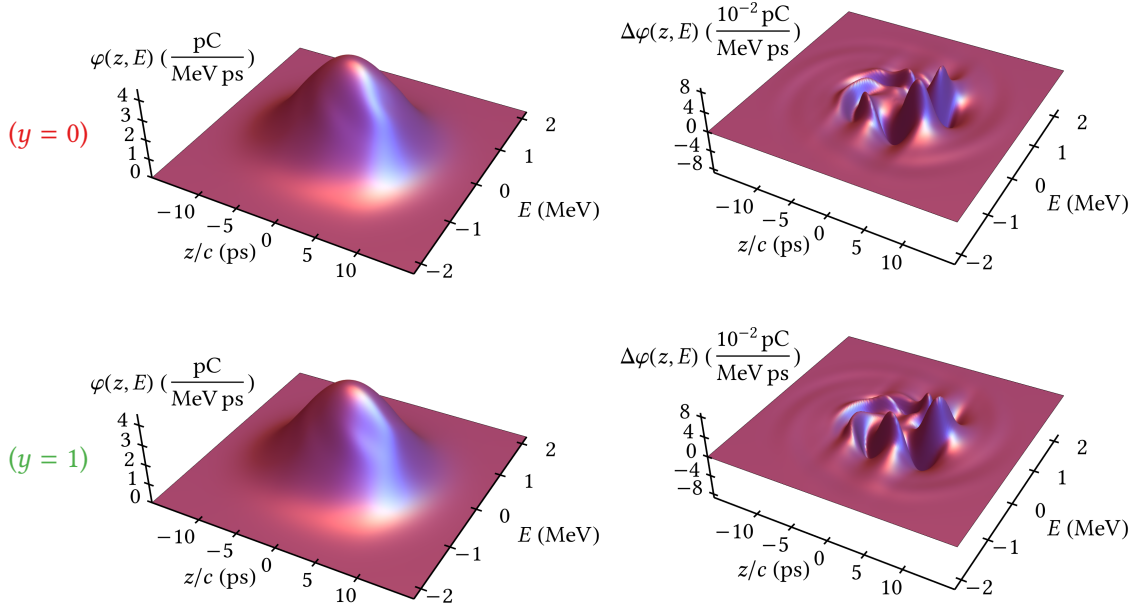
Figure 4.6.: The identified micro-structures can additionally be studied in the longitudinal phase space. Therefor, the mean phase space density of the found clusters $\overline{\varphi}_C(z, E)$ is calculated, shown above is the case of $k = 2$. The phase space means for the clusters with label $y = 0$ (upper left) and $y = 1$ (lower left) display barely recognizable micro-structures. Subtracting the global phase space mean $\overline{\varphi}(z, E)$ reveals quite distinct structures. Despite a slight rotation around the origin, the such illustrated micro-structures for $y = 0$ (upper right) and $y = 1$ (lower right) appear nearly identical.[2]

---

[2] The illustrations of the longitudinal phase space densities in this thesis are generated with *Mathematica* [30].

The asymmetry along the *z*-axis of the micro-structures' amplitude is visible in the longitudinal phase space as well. Furthermore, it should be noted, the two phase space cluster means show very similar structure. In fact, despite a small rotation around the center, they appear almost identical.

4.1.4. Modeling the Regular Bursting Dynamics

As shown in Section 4.1.1, the application of the *k*-means method on the temporal sequence of longitudinal profiles in the regular bursting regime, yields cluster centers that display a distinct sinusoidal modulation. Additionally, the corresponding emitted CSR power is very similar to a sinusoidal oscillation as well. This motivated the idea of modeling the longitudinal dynamics in the regular bursting regime by a simple sinusoidal curve oscillating with f_{reg} as a standing wave on top of the global mean $\overline{\rho}(z)$, i.e. the longitudinal profiles are modeled by:

$$\widetilde{\rho}(z, t_i) = \overline{\rho}(z) + \left[\widetilde{A}_{\text{mod}}(z) \sin(2\pi f_{\text{mod}} z/c + \phi_0)\right] \sin(2\pi f_{\text{reg}} t_i) , \qquad (4.7)$$

where $\widetilde{A}_{\text{mod}}(z)$ is a Gaussian shaped envelope scaling the modulations amplitude and f_{mod} the dominant frequency of the modulation found by the *k*-means method. Here, $f_{\text{mod}} \approx 160\,\text{GHz}$ is set as the frequency which has the maximum spectral intensity in the spectrum of the Fourier transformed referenced cluster center with label $y = 0$. The such approximated modulation is illustrated in Figure 4.7. Analogously, the regular bursting frequency $f_{\text{reg}} \approx 117.6\,\text{kHz}$ is estimated by the frequency where the Fourier transformed CSR power $P_{\text{csr}}(t_i)$ is maximal (see Figure 4.8, top row).

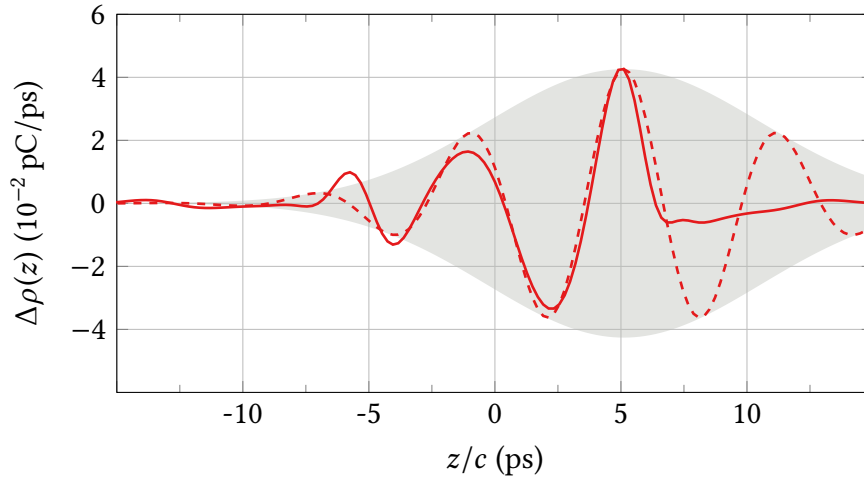Figure 4.7.: The modulation displayed by the referenced cluster centers in Figure 4.2 (solid line) is approximated by a simple sinusoidal curve (dashed line). Its phase and amplitude are chosen to match the maximum of the found modulation, while the modulation frequency is estimated by that which has the maximum spectral intensity in the spectrum of the Fourier transformed referenced cluster center.

For the such obtained longitudinal profiles $\widetilde{\rho}(z, t_i)$, the emitted CSR power $\widetilde{P}_{\mathrm{csr}}(t_i)$ is calculated using Eq. (2.17). Serving as a comparison, at the top of Figure 4.8, a characteristic section of the original CSR power signal $P_{\mathrm{csr}}(t_i)$ and its Fourier transform are shown. At the bottom of Figure 4.8, the CSR power $\widetilde{P}_{\mathrm{csr}}(t_i)$ and its Fourier transform, generated with this simple model, are displayed. The modeled CSR power $\widetilde{P}_{\mathrm{csr}}(t_i)$ (bottom left) oscillates in a very similar way to the originally simulated CSR power $P_{\mathrm{csr}}(t_i)$. Not only the maximum peak in the Fourier transform is found exactly at $f_{\mathrm{reg}} \approx 117.6\,\mathrm{kHz}$ as expected, but also the second peak at $f = 2\,f_{\mathrm{reg}}$ is reconstructed (bottom right), which is due to the square of the absolute value in Eq. (2.19), describing the longitudinal form factor $\mathcal{F}_z(k_z)$. Given the simplicity of the used model, the modeled and simulated signals are quite comparable, proving the model a simple, but robust description of the dynamics.
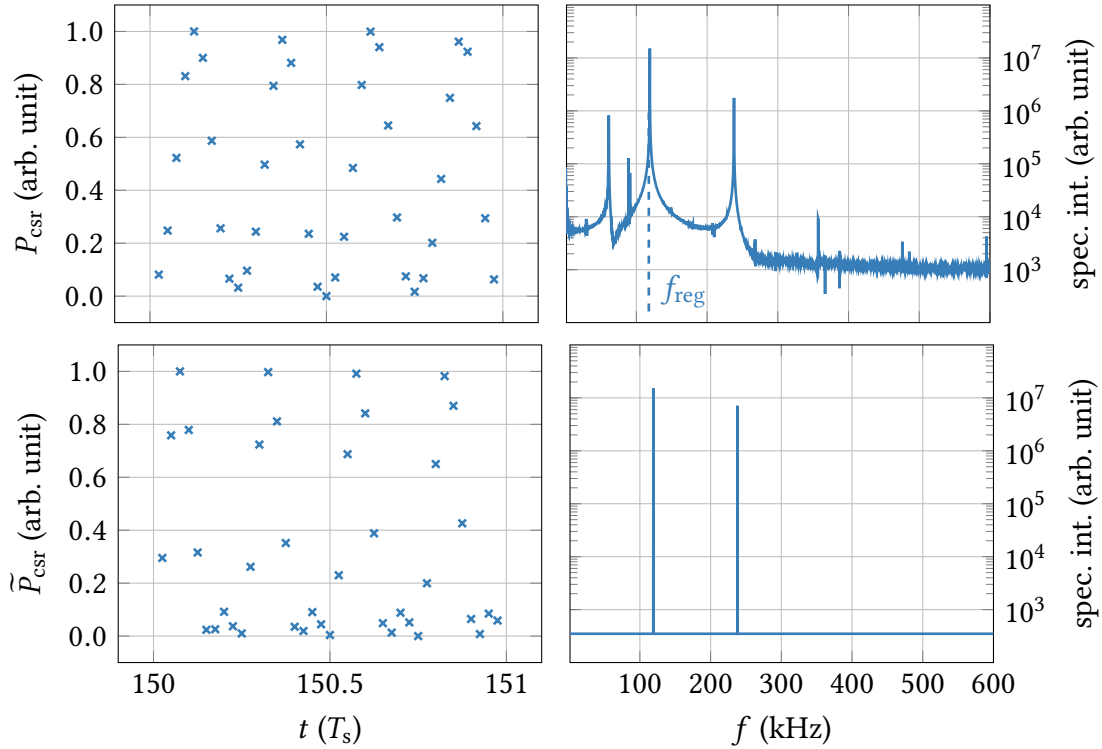
Figure 4.8.: Displayed are representative sections of the original CSR power signal $P_{\mathrm{csr}}(t_i)$ (upper left) and the corresponding $\widetilde{P}_{\mathrm{csr}}(t_i)$ (lower left) generated by the simple model of a sinusoidal modulation oscillating as a standing wave on top of the stationary global mean $\overline{\rho}(z)$. The right column shows the Fourier transform of $P_{\mathrm{csr}}(t_i)$ and $\widetilde{P}_{\mathrm{csr}}(t_i)$ during the full period ($t = 250\,T_s$), respectively. The second peak in the Fourier transform of $\widetilde{P}_{\mathrm{csr}}(t_i)$ at $f = 2\,f_{\mathrm{reg}}$ (lower right) is due to the square of the absolute value in Eq. (2.19), describing the longitudinal form factor $\mathcal{F}_z(k_z)$.

4.2. **Sawtooth Bursting Regime**

In order to demonstrate the differences in the longitudinal dynamics of the regular bursting regime and the sawtooth bursting regime, the exemplary bunch current $I_{saw} = 1.15\,\text{mA}$ is studied. The previously derived techniques of visualization can be used once again to analyze the results obtained by application of the k-means method to the longitudinal profiles.

4.2.1. **Visualization of Micro-Structures**

For the case of $I_{saw} = 1.15\,\text{mA}$, the application of the k-means method on the longitudinal profiles $\rho(z, t_i)$ searching for $k = 2$ clusters yields the cluster centers displayed in Figure 4.9. Again, the corresponding referenced cluster centers are shown below.
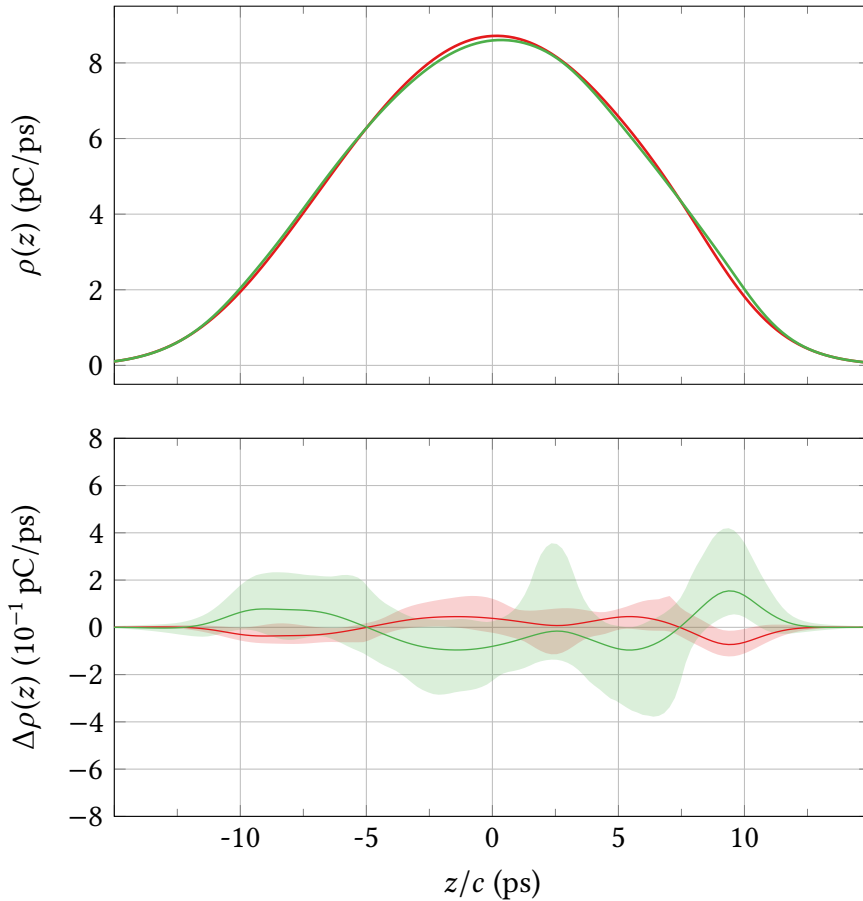
Figure 4.9.: In the upper part of the figure, the cluster centers found by application of the k-means method for the case of $I_{saw} = 1.15\,\text{mA}$ and $k = 2$ are shown. Below, the same cluster centers after subtracting the global mean $\overline{\rho}(z)$ are displayed again. The bunch length of the red cluster center is $\sigma_{z,0}/c = 5.37\,\text{ps}$ in contrast to the green cluster center with $\sigma_{z,1}/c = 5.43\,\text{ps}$.

Though one might be tempted to interpret these findings again as micro-structures on the longitudinal profiles, the circumstances in this case are slightly different and more complex. In fact, the main difference of the two displayed clusters is merely due to the different bunch lengths of the respective longitudinal profiles. This is indicated by the slightly higher values of the green referenced cluster center at the left and right edges of the longitudinal profiles. In contrast, the red referenced cluster center shows slightly higher values around the center $z = 0$.

In order to verify the effect of different bunch lengths on the shape of $\Delta\rho(z)$, two exemplary Gaussian shaped longitudinal profiles $\rho_{\mathrm{gauss},0}(z)$ and $\rho_{\mathrm{gauss},1}(z)$ with different bunch lengths, i.e. different standard deviations $\sigma_{\mathrm{gauss},0}$ and $\sigma_{\mathrm{gauss},1}$ are studied. These are displayed on the left in Figure 4.10. The right part of Figure 4.10 shows the two Gaussian profiles after subtracting their mean. It is apparent, that the difference in bunch length causes the illusion of a modulation induced by micro-structures in the longitudinal phase space. This modulation however, does only appear with about 1.5 period lengths on the longitudinal profiles, which in this case, corresponds to the approximate frequency of $f_\sigma \approx 1.5/30\,\mathrm{ps} = 50\,\mathrm{GHz}$. This is further addressed in Section 4.4.
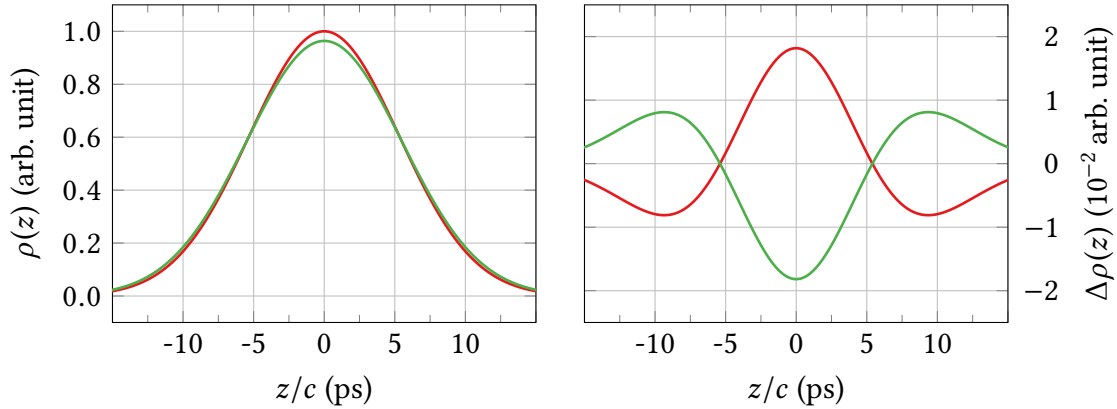
Figure 4.10.: Two exemplary Gaussian profiles with different bunch lengths, i.e. standard deviations $\sigma_{\mathrm{gauss},0}/c = 5.3\,\mathrm{ps}$ (red) and $\sigma_{\mathrm{gauss},1}/c = 5.5\,\mathrm{ps}$ (green) are shown on the left. Their differences to the mean (average of both Gaussian profiles) are displayed on the right. This can create the illusion of micro-structures on the longitudinal profiles. However, this modulation is only appearing with about 1.5 period lengths, which corresponds to the approximate frequency of $f_\sigma \approx 50\,\mathrm{GHz}$.

However, if the k-means method is applied searching for $k = 4$ clusters, the two additional cluster centers display actual micro-structures on the longitudinal bunch profiles, as illustrated in Figure 4.11. The micro-structures are already clearly visible without subtracting the global mean $\overline{\rho}(z)$. This is due to the higher amplitude of the found modulation when compared to the results in the regular bursting regime (see Figure 4.4). The maximum amplitude of the total cluster centers is increased approximately by a factor of 1.26 compared to the cluster centers in Figure 4.2 due to the higher bunch current I_{bunch}. In contrast, the amplitude of the found micro-structures is increased approximately by a factor of 11. The modulation's frequency f_{mod} however, appears to be quite similar.

The newly found clusters corresponding to the green and orange cluster centers contain merely about $n_{\mathrm{cluster}} \approx 300$ longitudinal profiles. In contrast, the red cluster contains about $n_{\mathrm{cluster}} \approx 3200$ longitudinal profiles and the blue cluster approximately twice that amount $n_{\mathrm{cluster}} \approx 6200$. This explains why the micro-structures, although having a relatively large amplitude, were not found for the application of the k-means method with $k = 2$.
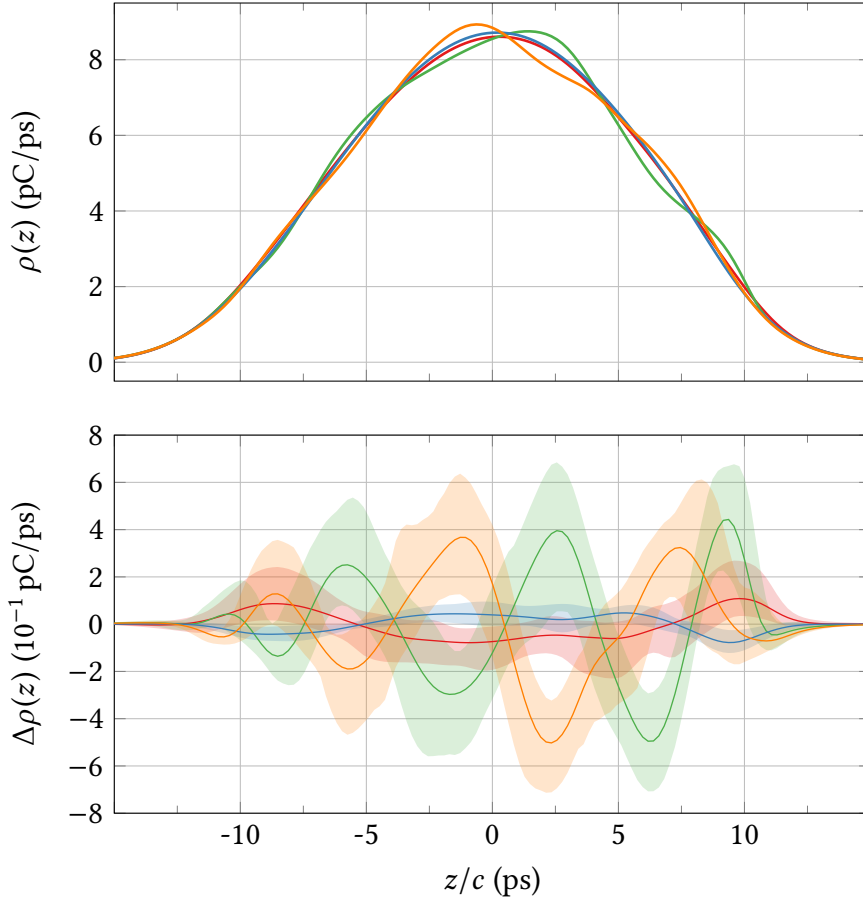
Figure 4.11.: When the number of clusters searched for by the k-means method is increased to $k = 4$, distinct micro-structures are found for the case of $I_{\mathrm{saw}} = 1.15\,\mathrm{mA}$ as well. These are already visible on the original cluster centers (top) and are highlighted by subtracting the global mean $\overline{\rho}(z)$ (bottom). Compared to the micro-structures in the regular bursting regime (see Figure 4.2), the amplitude is increased by a factor of approximately 11, while the modulation's frequency appears to be quite similar. In contrast to the red and blue referenced cluster centers, the green and orange ones display similar bunch lengths, i.e. $\sigma_{z,1}/c = 5.41\,\mathrm{ps}$ and $\sigma_{z,3}/c = 5.40\,\mathrm{ps}$.

4.2.2. Correlation with Emitted CSR

As explained in Section 4.1.2, the discrete time signal of the CSR power $P_{csr}(t_i)$ corresponding to the longitudinal profiles $\rho(z, t_i)$ can be mapped to the associated cluster labels $y(t_i)$. Figure 4.12 shows the CSR power signal $P_{csr}(t_i)$ for the case of $I_{saw} = 1.15\,\text{mA}$ and $k = 4$, where the color of each point is defined by the corresponding label $y(t_i)$. Again, the found clusters appear to be strongly correlated to the emitted CSR power $P_{csr}(t_i)$. The red and blue cluster contain mainly the longitudinal profiles corresponding to the sections between the sawtooth shaped bursts of emitted CSR, e.g. from $t = 50\,T_s$ to $t = 100\,T_s$. As clarified above, the main difference of the longitudinal profiles in those clusters is their respective bunch length, e.g. $\sigma_z(50\,T_s)/c = 5.34\,\text{ps}$ compared to $\sigma_z(100\,T_s)/c = 5.43\,\text{ps}$. As explained in Section 2.1.7, this is attended by an increase of the emitted CSR power.
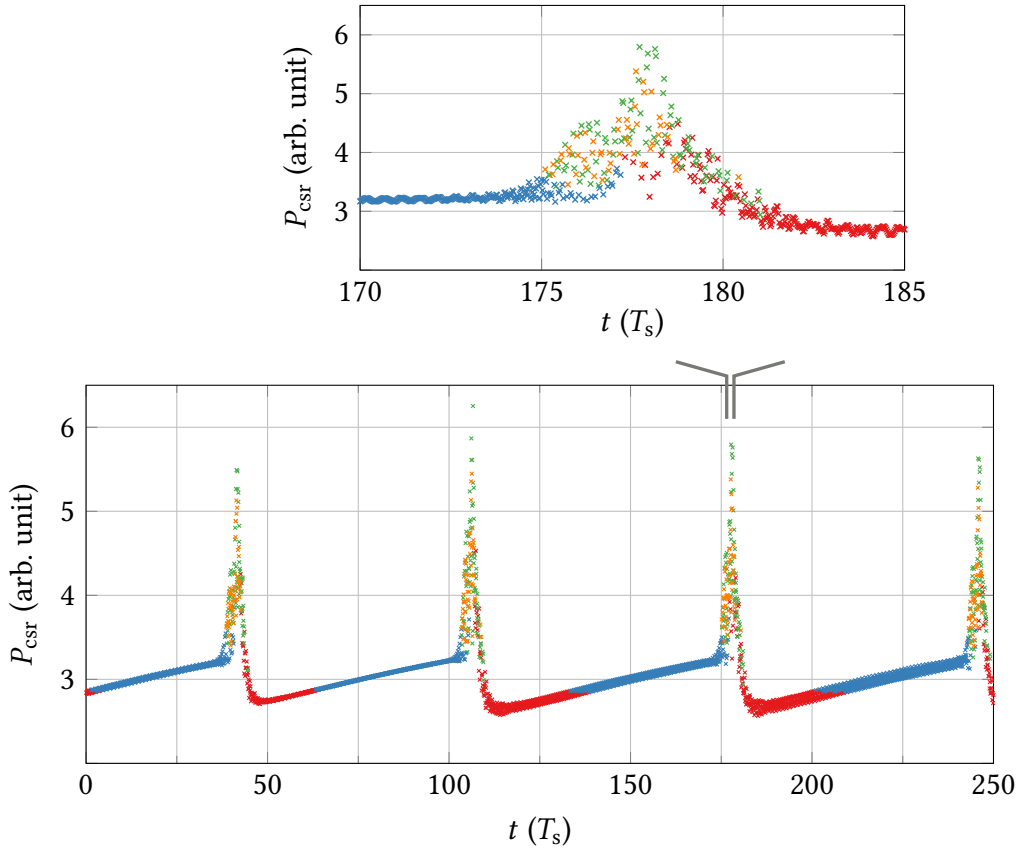
Figure 4.12.: Analogously to Figure 4.5, each value of the discrete CSR power signal $P_{csr}(t_i)$ is colored according to its corresponding label $y(t_i)$. Again, the discrete CSR power signal is strongly correlated to the associated sequence of cluster labels $y(t_i)$. While the red and blue cluster centers in Figure 4.11 describe the bunch length reduction process between the bursts, the green and orange cluster centers describe the relatively large micro-structures during the sawtooth shaped bursts of CSR emission, as the one between $t = 170\,T_s$ and $t = 185\,T_s$ which is expanded in the upper part of the figure.

In contrast, the green and orange cluster contain the longitudinal bunch profiles corresponding to the four sawtooth shaped bursts over the simulated 250 synchrotron periods. The respective cluster centers display an actual modulation caused by micro-structures in the longitudinal phase space. Again, the two cluster centers describe the phase and paraphase of this modulation. During these sawtooth shaped bursts, the cluster labels $y(t_i)$ are rapidly alternating between the phase and its paraphase (green and orange cluster). This is quite similar to the behavior in the regular bursting regime. Additionally, as can be seen in the upper part of Figure 4.12, the emitted CSR power $P_{csr}(t_i)$ is slightly oscillating between these bursts, e.g. between $t = 170\,T_s$ to $t = 174\,T_s$ and $t = 182\,T_s$ to $t = 185\,T_s$. This indicates, these micro-structures are in fact always present, it is just their amplitude that is considerably increased during these burst of CSR emission, which will be further addressed in the following section.

It is worth noting, the frequency with which these sawtooth shaped burst are occurring is in the order of $f_{saw} \approx 1\,\mathrm{kHz}$. These low frequency contributions are merely indicated at the left edge of Figure 4.1, therefore the same CSR power spectrogram is displayed with a logarithmically scaled frequency axis in Appendix A.2. Additionally, further studies of the bunch shortening process are shown in Appendix A.3.

4.2.3. Longitudinal Phase Space

Analogously to Section 4.1.3, the found micro-structures can be studied directly in the longitudinal phase space. The phase space cluster means $\overline{\varphi}_C(z, E)$ for the case of $I_{saw} = 1.15\,\mathrm{mA}$ and $k = 4$ are shown in the left column of Figure 4.13. The right column displays their difference to the global mean $\overline{\varphi}(z, E)$ respectively. The phase space cluster mean with label $y = 0$ (first row) corresponds to the red cluster center in Figure 4.11. Together with the phase space cluster mean for the blue cluster center ($y = 2$, third row), they display the effects of the bunch shortening process between the sawtooth shaped bursts of the emitted CSR power (see Figure 4.12) in the longitudinal phase space. Compared to each other, for the cluster with $y = 2$, the electron distribution is concentrated around the center, whereas for the cluster with $y = 0$ it is spread more widely excessing the global phase space mean $\overline{\varphi}(z)$ near the edges of the figure. The phase space cluster mean with label $y = 1$ (second row) and the phase space cluster mean with label $y = 3$ (last row) correspond to the green and orange cluster centers in Figure 4.11 and display distinct micro-structures in the longitudinal phase space.

At this point however, it is not clear what might be lost by averaging over all the different phase space densities $\varphi(z, E, t_i)$. Since these phase space cluster means are again statistical quantities rather than actual longitudinal phase space densities, additional steps have to be taken in order to verify these findings. For that purpose and to further investigate the dynamics of the longitudinal phase space density, characteristic sequences of $\Delta\varphi(z, E, t_i)$ for the different bursting regimes have been put into short videos, while incorporating the corresponding CSR power $P_{csr}(t_i)$ and the corresponding referenced longitudinal profiles $\Delta\rho(z, t_i)$. Subsequently, these video sequences have been studied frame by frame. While displaying all the frames is beyond the scope of this thesis, several insights could be gained with this method. Figure 4.14 shows a selection of the referenced phase space densities $\Delta\varphi(z, E, t_i)$ for three particular time steps.
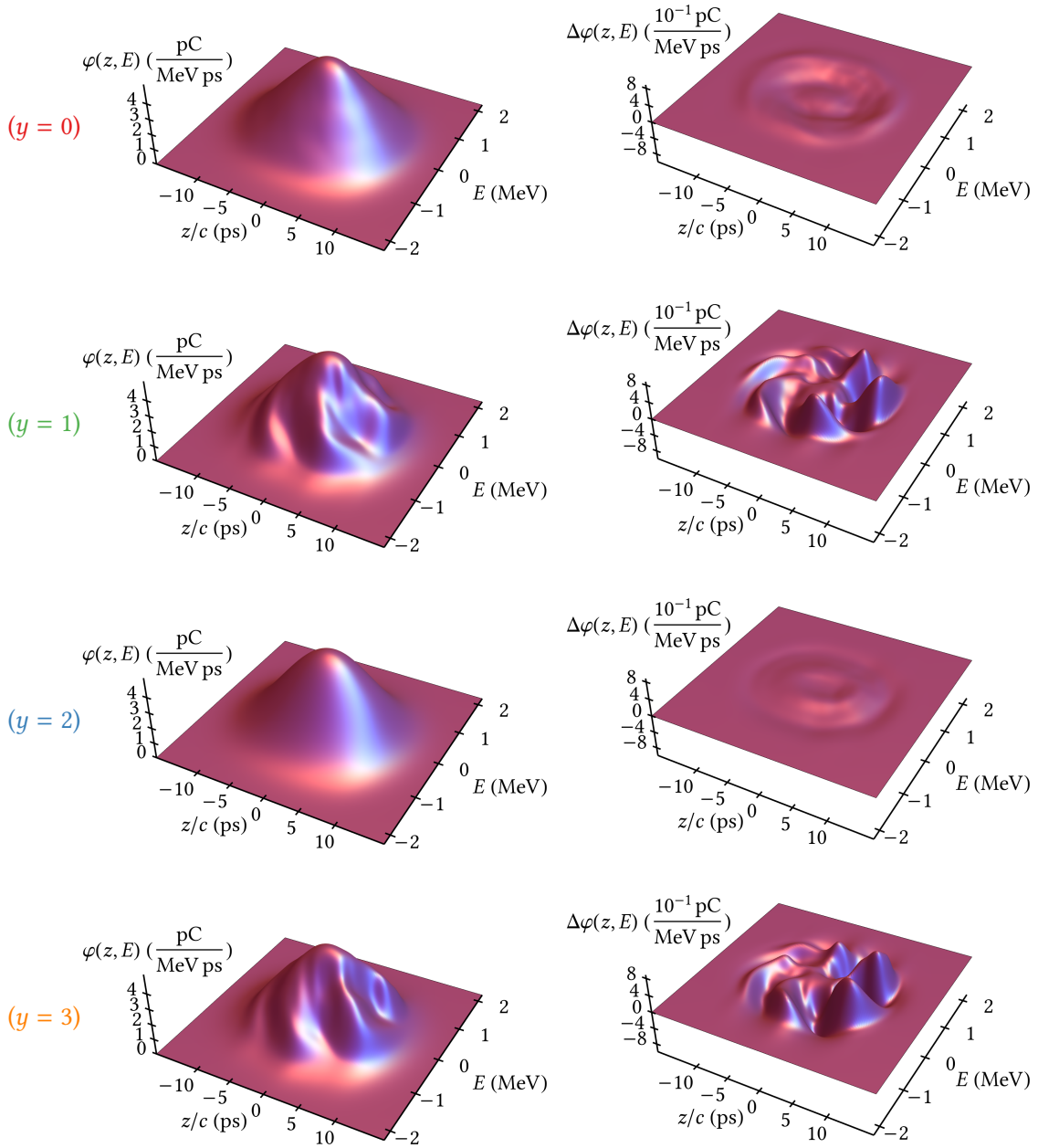
Figure 4.13.: Phase space cluster means for the case of $I_{\text{saw}} = 1.15\,\text{mA}$ and $k = 4$. The cluster with label $y = 0$ (first row) and the cluster with $y = 2$ (third row) correspond to the red and blue cluster centers in Figure 4.11 and display the effects of the bunch shortening process. The phase space cluster means of the clusters with label $y = 1$ (second row) and $y = 3$ (last row) correspond to the green and orange cluster centers in Figure 4.11 and display actual micro-structures. Compared to those found in the regular bursting regime (see Figure 4.6) they appear very similar. However, here the amplitude is increased by approximately a factor of 11.

The emitted CSR power $P_{\mathrm{csr}}(t_i)$ in the sawtooth bursting regime consists of relatively long sections where the dominating longitudinal dynamic is a reduction of the electron bunch length σ_z and of relatively short sawtooth shaped bursts of CSR emission between that. The above illustrated micro-structures are always present in the longitudinal phase space. This is illustrated in the right part of Figure 4.14, where a snapshot of the referenced phase space density $\Delta\varphi(z, E, t_i)$ is shown for the time step $t_i = 211\,T_{\mathrm{s}}$, which lies in the very middle of two bursts of the emitted CSR power $P_{\mathrm{csr}}(t_i)$. Though not quite as distinct, the micro-structures are still present.
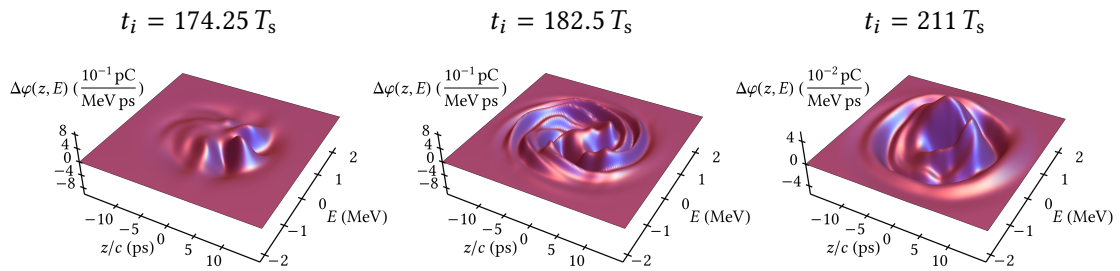
$$t_i = 174.25\,T_{\mathrm{s}} \qquad t_i = 182.5\,T_{\mathrm{s}} \qquad t_i = 211\,T_{\mathrm{s}}$$

Figure 4.14.: In order to verify the representative function of the previously calculated phase space cluster means $\Delta\varphi_{\mathrm{C}}$ and to further study the longitudinal dynamics, an exemplary sequence of longitudinal phase space densities $\Delta\varphi(z, E, t_i)$ with subtracted global phase space mean $\overline{\varphi}(z, E)$ is studied. Shown are characteristic snapshots for three different time steps, i.e. $t_i = 174.25\,T_{\mathrm{s}}$ (left), $t_i = 182.5\,T_{\mathrm{s}}$ (middle) and $t_i = 211\,T_{\mathrm{s}}$ (right). It should be noted, due to the comparably low amplitude of the micro-structures, the scaling of $\Delta\varphi$-axis in the right figure has been adjusted.

The sudden increase of the emitted CSR power during the sawtooth shaped bursts is attended by an enhancement of the micro-structures' amplitudes. This is illustrated in the left of Figure 4.14 by a snapshot of the referenced phase space density $\Delta\varphi(z, E, t_i)$ for the time step $t_i = 174.25\,T_{\mathrm{s}}$, which lies at the beginning of such a sawtooth shaped burst. While the amplitude of the micro-structures is increased, it is still beyond the amplitudes achieved during the subsequent burst, where the micro-structures are the most distinct. Therefore, during the sawtooth shaped bursts, they can be studied quite easily. The micro-structures are rotating counter-clockwise around the origin in the longitudinal phase space while getting slightly magnified in the $z > 0$ direction and reduced again in the $z < 0$ direction. As different extrema get added up during the projection on the z-axis, alternating states of modulations are caused on the corresponding longitudinal profiles. This is the effect, which is causing the oscillation of the CSR power in the regular bursting regime. After the burst, when the CSR power is decreasing again, so are the amplitudes of these micro-structures. Additionally, at this point in time, the micro-structures appear to be "washed out", compared to their previously quite distinct structure, which is shown in the middle of Figure 4.14 for the time step $t_i = 182.5\,T_{\mathrm{s}}$. Immediately after a burst in the emitted CSR power, the electron bunch has a comparably long bunch length σ_z. Subsequently, the bunch length is shrinking again until the next burst is reached.

It should be noted, despite the increased amplitude, the displayed micro-structures appear very similar to those found in the regular bursting regime shown in Figure 4.6. In fact, similar looking micro-structures were found for all the different bunch currents I_{bunch} above the bursting threshold I_{th} in Figure 4.1. While the general appearance, i.e. the number of micro-structures and their overall shape is consistent throughout the different regimes of CSR emission, the temporal changes of their amplitude is what causes the differences in the emitted CSR power. This is considered one of the main results of this thesis.

4.3. Optimization of Cluster Number *k*

In the introduction to the k-means method in Section 2.2.2, it was mentioned that the number of clusters k is a free parameter, i.e. it has to be chosen manually for every concrete application of the k-means method. For the data set at hand, the k-means method was applied to all 151 bunch currents I_{bunch} searching for $k = 2$ to $k = 6$ clusters. In the following, different methods to identify the optimal value k_{opt} are discussed.

The application of the k-means method provides a separation of the given data set into different categories by assigning a particular label y to each data object. In order to achieve an appropriate categorization, it makes use of statistical features like the cluster mean or the quadratic sum of distances of data objects within a cluster to their respective cluster mean, see Eq.(2.30). The degree to which the k-means method was able to separate the data set into distinct clusters can be checked by employing various methods, see e.g. Ref. [32]. Two of these, i.e. the so-called elbow method and the calculation of silhouette coefficients are discussed below. It should be noted, the displayed within cluster standard deviations in the Figures 4.2, 4.4, 4.9 and 4.11 are already a measure for the achieved compactness and separation of the found clusters.

Due to the nature of the k-means method, the final value of the objective function J_k after reaching convergence is monotonically decreasing for incremented cluster number k. This is illustrated in Figure 4.15a for the case of $I_{\text{saw}} = 1.15\,\text{mA}$. For many successful applications of the k-means method, the displayed objective function J_k has a distinct kink at a specific value of k causing the overall shape to look somewhat similar to an elbow. However, for the data sets in this thesis, such a kink is often barely noticeable. The identification of the kink can also be done automatically, rather than by the unaided eye, using e.g. the so-called gap statistic [33]. Yet, for the context of this thesis, other methods of evaluation have been explored.

Another statistical technique to evaluate the found clustering is the calculation of so-called silhouette coefficients, as introduced in Ref. [34]. For each data object $\boldsymbol{x}_i$ assigned to cluster C_a, the silhouette coefficient describes the similarity of $\boldsymbol{x}_i$ to the other objects within C_a compared to the similarity of $\boldsymbol{x}_i$ to the objects within another cluster C_b:

$$s(\boldsymbol{x}_i) = \frac{\text{dist}(\boldsymbol{x}_i, C_b) - \text{dist}(\boldsymbol{x}_i, C_a)}{\max\{\text{dist}(\boldsymbol{x}_i, C_a),\ \text{dist}(\boldsymbol{x}_i, C_b)\}}\ , \tag{4.8}$$

where $\text{dist}(\boldsymbol{x}_i, C_a)$ denotes the average distance of $\boldsymbol{x}_i$ to a data object $\boldsymbol{x}_a \neq \boldsymbol{x}_i$ in cluster C_a. Analogously, $\text{dist}(\boldsymbol{x}_i, C_b)$ denotes the average distance of $\boldsymbol{x}_i$ to a data object $\boldsymbol{x}_b$ in cluster

C_b. The reference cluster C_b is chosen as that with the highest similarity to C_a, i.e. where the average distance of $\boldsymbol{x}_i$ to the objects in C_b is the smallest. Furthermore, the average value of all the silhouette coefficients $\boldsymbol{x}_i$ in the data set for a given value of k is described by the silhouette score:

$$S_k = \frac{1}{n} \sum_{i=1}^{n} s(\boldsymbol{x}_i) \, . \tag{4.9}$$

While the possible values range from $s(\boldsymbol{x}_i) = -1.0$ to $s(\boldsymbol{x}_i) = 1.0$, an overall score of $S_k > 0.5$ is considered a sign for a distinct structure in the data set displayed by the categorization of the clustering method. It should be noted, the silhouette coefficients $s(\boldsymbol{x}_i)$ and therefore the silhouette score S_k are not defined for the case of $k = 1$.
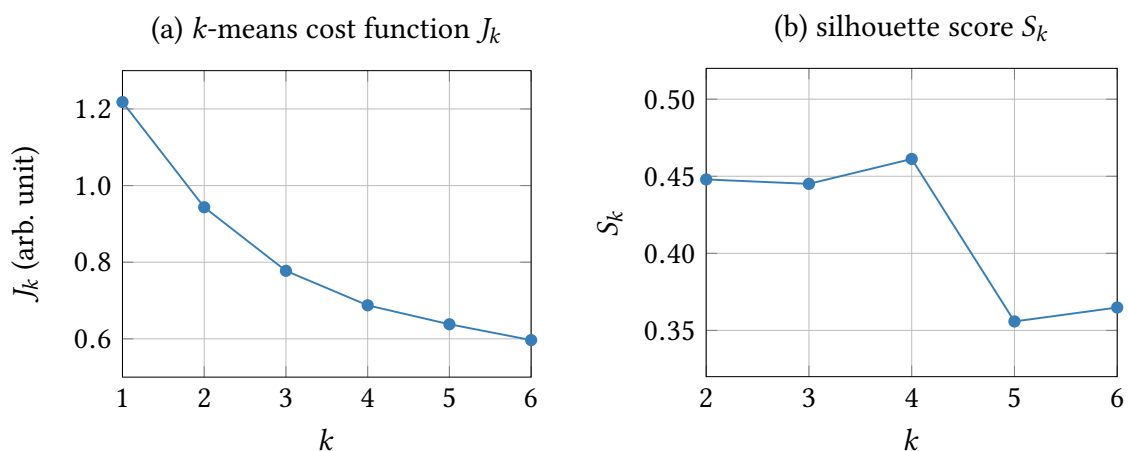

Figure 4.15.: The results of two different methods to evaluate the found clusters and to identify the optimal number of clusters k_{opt} are shown. (a) The k-means cost function J_k is monotonically decreasing for incremented cluster number k. The so-called elbow method aims to identify a kink after which the cost function is decreasing much slower. However, in this case there is no such definite kink visible. (b) The silhouette coefficient $s(\boldsymbol{x}_i)$ is a measure of how similar a data object $\boldsymbol{x}_i$ is to the other data objects within its cluster compared to its similarity to data objects in another cluster. Shown is the average value S_k of $s(\boldsymbol{x}_i)$ for all data objects, i.e. longitudinal profiles, in the data set for each value of k respectively. For this method, the highest value of S_k marks the best possible cluster number, in this case $k_{\mathrm{opt}} = 4$.

Figure 4.15b shows the such obtained values S_k for the case of $I_{\mathrm{saw}} = 1.15\,\mathrm{mA}$ and the cluster numbers $k = 2$ to $k = 6$. Relying on these findings, the optimal value for the number of clusters to search for in this data set would be $k_{\mathrm{opt}} = 4$. In the case of $I_{\mathrm{saw}} = 1.15\,\mathrm{mA}$, this is quite appropriate since no additional insights were gained when searching for more than $k = 4$ clusters. As previously illustrated, atleast $k > 2$ is necessary to display the micro-structures during the sawtooth shaped bursts of the CSR power $P_{\mathrm{csr}}(t_i)$. For $k = 4$, the phase and paraphase of the corresponding modulation on the longitudinal profiles are represented. However, by analyzing the results for different values of k, it was e.g. easier to distinguish between cluster centers displaying the bunch shortening process

rather than actual micro-structures. An investigation of the longitudinal profiles using step by step incremented values of k helps to further understand the underlying dynamics. Additionally, using the silhouette score S_k to identify k_{opt} for different bunch currents I_{bunch} does not always yield such satisfying results as for $I_{saw} = 1.15\,\text{mA}$.

Eventually, for the application of the k-means method in this thesis, neither of the above discussed methods are found to be perfectly suited to evaluate the found results or to determine the optimal value for the number of clusters k_{opt}. Instead, studying the correlation to the respective CSR power signal is considered the most adequate way of evaluating the clusters found by the k-means method. This is due to the fact that this is not an ordinary application of the clustering method. Ideally, the k-means method is applied to a data set with a distinct number of different groups of data objects which are very compact and clearly separable from each other. Since, for the case at hand, the k-means method is employed as an exploratory tool of data analysis in order to gain deeper insights to a dynamic process, such distinct groups might not exist. The k-means method has been applied onto a continuously changing dynamic system, which is approximated by a discretization process in the time domain. Although the silhouette score $S_4 \approx 0.46$ proves the found separation quite reasonable, the achieved categorization has to be interpreted as a statistically representative discretization of the dynamics in the longitudinal bunch profiles. These describe e.g. the phase and paraphase of a dynamic modulation or different states in a bunch shortening process. After evaluating these discrete states, i.e. the cluster centers as representatives of the found clusters, and studying the correlation of the respective cluster label sequence $y(t_i)$ to the emitted CSR power $P_{csr}(t_i)$, it can be stated that this discretization is also a reasonable approximation of the underlying longitudinal dynamics and the corresponding radiation behavior. This is further addressed in Section 4.5, where the found clustering sequence $y(t_i)$ and the corresponding radiation behavior are analyzed throughout the entire range of bunch currents I_{bunch} displayed in Figure 4.1.

4.4. Modulation Amplitude and Frequency

For the modeling of the regular bursting dynamics in Section 4.1.4, the frequency of the found modulation f_{mod} is approximated by the frequency with maximal spectral intensity in the spectrum of the Fourier transformed referenced cluster center with label $y = 0$. In order to study the dynamics of the found micro-structures over the various currents, the modulation frequency and amplitude have been determined for all the referenced cluster centers found for $k = 4$ for each of the 151 bunch currents I_{bunch}. Figure 4.16 illustrates the procedure for the bunch current of $I_{saw} = 1.15\,\text{mA}$. As the referenced cluster centers consist of merely $n_{grid} = 200$ points, they are zero-padded[3] before the Fourier transform is calculated.

The thus obtained approximated modulation frequencies f_{mod} for all the different referenced cluster centers are shown in Figure 4.17. The color of each point displays the cluster label y of the respective referenced cluster center, according to Table 4.1. For example, the green and orange points at $I_{saw} = 1.15\,\text{mA}$ with values between $f_{mod} = 100\,\text{GHz}$ and

---

[3] Several zeros are added at the left and right edges of the cluster centers to increase the amount of frequency bins after the subsequent Fourier transformation, see e.g. [35].
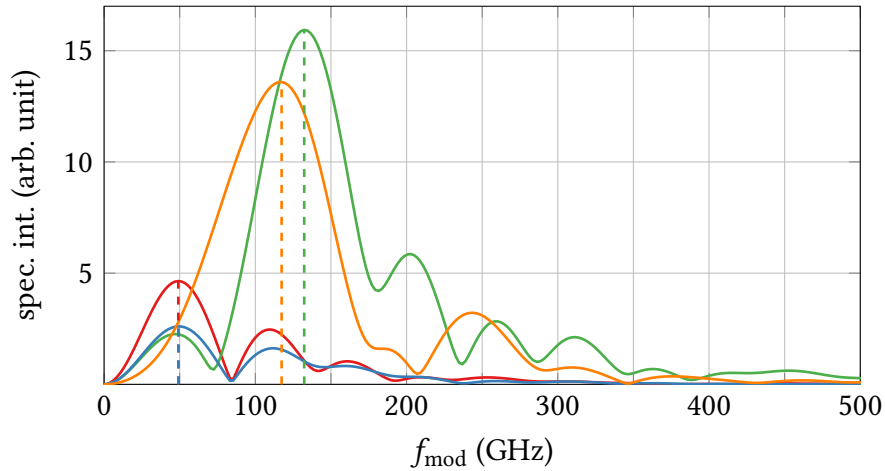
Figure 4.16.: Approximation of the modulation frequency f_{mod} for $I_{saw} = 1.15\,\text{mA}$ and $k = 4$. Shown are the Fourier transformed zero-padded referenced cluster centers displayed in the lower part of Figure 4.11. While the main frequency for the red and blue referenced cluster centers is about $f_{mod} \approx f_\sigma \approx 50\,\text{GHz}$, the green and orange referenced cluster centers have quite dominant frequencies higher than $f_{mod} = 100\,\text{GHz}$.

$f_{mod} = 150\,\text{GHz}$ correspond to the referenced cluster centers with the same color in Figure 4.11. While the micro-structures displayed by these cluster centers yield a modulation frequency of $f_{mod} > 100\,\text{GHz}$, the red and blue referenced cluster centers in Figure 4.11 correspond to an equal modulation frequency of about $f_{mod} \approx f_\sigma \approx 50\,\text{GHz}$, due to the previously mentioned bunch shortening process. For the case of $I_{reg} = 0.88\,\text{mA}$, the green and orange referenced cluster centers in Figure 4.4 yield an identical modulation frequency at roughly $f_{mod} \approx 160\,\text{GHz}$. In contrast, the red and blue intermediate states in Figure 4.4 yield a modulation frequency of about $f_{mod} \approx 230\,\text{GHz}$.

Below the bursting threshold at $I_{th} = 0.87\,\text{mA}$, despite very few exceptions, only modulation frequencies with $f_{mod} \approx f_\sigma$ are found. While the longitudinal profiles are slightly deviating in their bunch length σ_z, no micro-structures are found in this current range. Right above the threshold at $I_{th} = 0.87\,\text{mA}$, the cluster centers found by the k-means method display modulations which are caused by micro-structures in the longitudinal phase space. The average differences of longitudinal profiles displaying the phase and paraphase of the corresponding modulations are dominating, when compared to the previously displayed deviations in bunch length. For this reason, no modulation frequencies with $f_{mod} \approx f_\sigma$ are displayed for a range of bunch currents above $I_{th} = 0.87\,\text{mA}$. However, entering the sawtooth bursting regime, the deviations in bunch length are increasing until they compete with the differences caused by micro-structures. Additionally, for the applied discretization of the time axis t_i, the number of longitudinal profiles in the relatively long sections between the sawtooth shaped bursts is much higher than those during the relatively short bursts. This is heavily influencing the results of the k-means method, e.g. when searching for merely $k = 2$ clusters in the sawtooth bursting regime (see Figure 4.9).
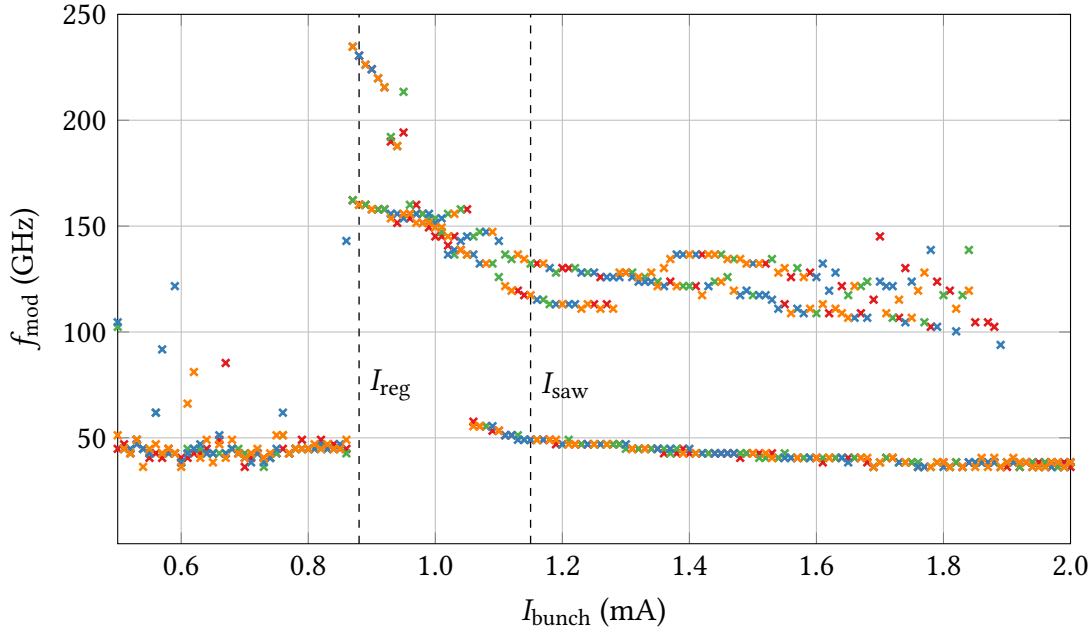
Figure 4.17.: The frequency f_{mod} of the modulations found in different cluster centers is approximated using the Fourier transform of the respective referenced cluster centers, as explained in Figure 4.16. Shown are the results for all 151 bunch currents I_{bunch}, searching for $k = 4$ clusters. The points with values concentrated around $f_{\mathrm{mod}} = 50\,\mathrm{GHz}$ are due to deviations in the bunch length σ_z, while the points with higher frequency are caused by micro-structures in the longitudinal phase space.

For bunch currents higher than $I_{\mathrm{bunch}} \approx 1.9\,\mathrm{mA}$, a cluster number with $k > 4$ is necessary to display the micro-structures, which is why only points with $f_{\mathrm{mod}} \approx f_\sigma$ are visible.

Eventually, it is worth noting, the main modulation frequency f_{mod} due to micro-structures in the longitudinal profiles is very similar across all the different bunch currents I_{bunch} above $I_{\mathrm{th}} = 0.87\,\mathrm{mA}$. Despite a slight decay, which is also visible for the points at $f_{\mathrm{mod}} \approx f_\sigma$, the dominant modulation frequencies for the different currents stay almost constant in Figure 4.17. These results agree with the previously mentioned similarity of the micro-structures in the longitudinal phase space across different bunch currents I_{bunch} (see Sections 4.1.3 and 4.2.3).

Another way to study the scale of the micro-structures on the longitudinal profiles is to determine the amplitude A_{mod} of the found modulations. Figure 4.18 shows the maxima of the absolute value of the referenced cluster centers found for $k = 4$ across the range of bunch currents I_{bunch}. Below the threshold $I_{\mathrm{th}} = 0.87\,\mathrm{mA}$, this amplitude is very small as the main dynamics are slight deviations in the bunch length σ_z of the longitudinal bunch profiles. Exactly at the bursting threshold $I_{\mathrm{th}} = 0.87\,\mathrm{mA}$, there is an abrupt rise in the modulation's amplitude A_{mod} due to micro-structures occurring in the longitudinal phase space. For the referenced cluster centers in the regular bursting regime, as shown in Figure 4.4, the phase and paraphase yield very similar amplitudes A_{mod} respectively. However, the red and blue cluster centers displaying intermediate states of the modulation
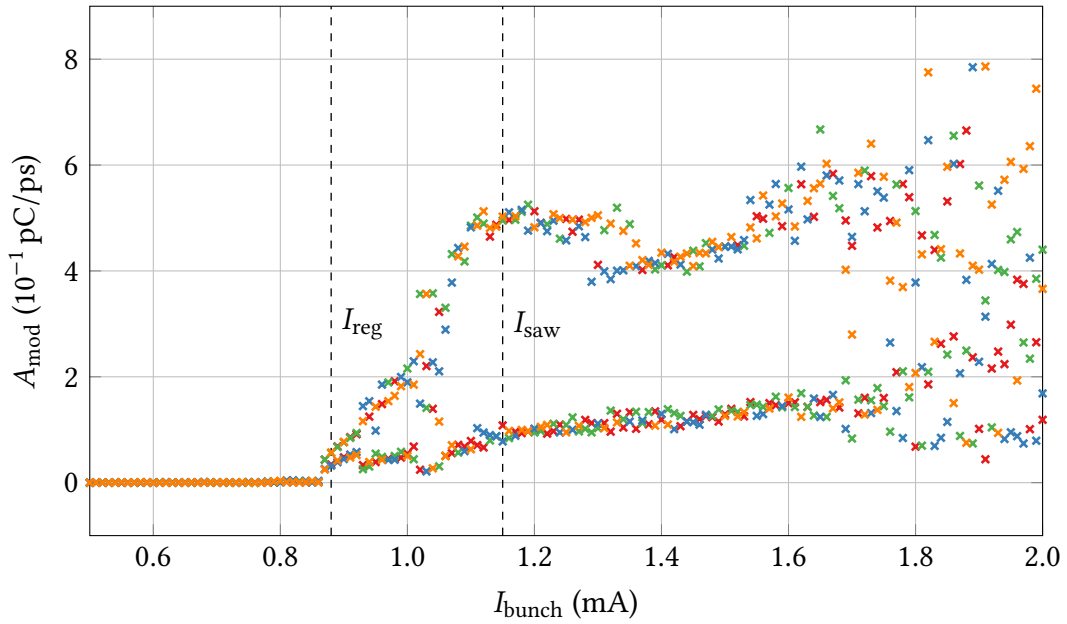
Figure 4.18.: The modulations' amplitudes A_{mod} can be estimated by calculating the maxima of the absolute value of the referenced cluster centers. Shown are the results for all 151 bunch currents while searching for $k = 4$ clusters. Two separate groups of points are visible due to different effects causing the respective modulation. While most of the points with low amplitude A_{mod} correspond to referenced cluster centers describing a bunch shortening, the higher values of A_{mod} are due to referenced cluster centers displaying actual micro-structures.

have slightly smaller amplitude than the green and orange referenced cluster centers. This yields the initial two separate regions of points above $I_{\mathrm{th}} = 0.87\,\mathrm{mA}$ until $I_{\mathrm{bunch}} = 0.93\,\mathrm{mA}$. For $I_{\mathrm{bunch}} = 0.94\,\mathrm{mA}$ and higher currents, the respective CSR power displays no longer a purely sinusoidal oscillation with f_{reg}, but has some low-frequency contributions. For the sawtooth bursting regime starting approximately at $I_{\mathrm{bunch}} = 1.07\,\mathrm{mA}$, this yields a distinct separation of the referenced cluster centers' amplitude. For $I_{\mathrm{saw}} = 1.15\,\mathrm{mA}$, the red and blue referenced cluster centers in Figure 4.11 display the bunch shortening process, while the green and orange referenced cluster centers display actual micro-structures and therefore yield an approximately five times higher amplitude A_{mod}. Above $I_{\mathrm{bunch}} \approx 1.8\,\mathrm{mA}$, the amplitudes A_{mod} are no longer divided into these distinct groups. By comparing with Figure 4.17, it is apparent that the modulation's amplitude due to the bunch shortening process is now in the same order of magnitude as the one which is caused by actual micro-structures in the longitudinal phase space.

In order to further verify the two separate effects of a bunch shortening and microstructures in the longitudinal phase space on the found modulations, the correlation between the modulation's frequency f_{mod} and amplitude A_{mod} is illustrated in Figure 4.19. All points with higher frequency than $f_{\mathrm{mod}} = 75\,\mathrm{GHz}$ are marked red in the left figure. The same color scheme is applied to the modulation amplitudes on the right. Apparently, the referenced cluster centers with $f_{\mathrm{mod}} \approx f_\sigma$ correspond to low values in the amplitude
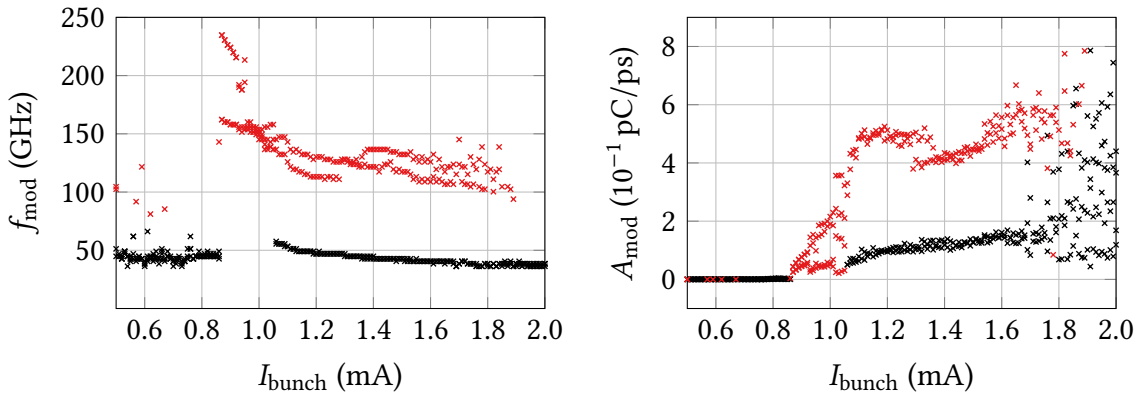
Figure 4.19.: (Left) The modulation frequencies with $f_{mod} > 75\,\text{GHz}$ are colored red. (Right) The same color scheme is applied to the modulation amplitudes, illustrating the correlation of f_{mod} and A_{mod}. While the modulation frequencies corresponding to a bunch shortening effect $f_{mod} \approx f_\sigma$ (black) yield small values of A_{mod}, the modulation amplitudes due to micro-structures are considerably higher (red).

A_{mod}, while the occurring micro-structures have a higher modulation frequency f_{mod} as well as a higher amplitude A_{mod}.

The micro-structures within this data set (i.e. with the parameter settings in Table 3.1) were found to display very similar scale and overall structure. However, a systematic study of additional data sets to verify these findings was beyond the scope of this thesis. This is necessary in order to confirm the nearly constant modulation frequency over various bunch currents and to analyze its dependency on different parameters, e.g. the parallel plates distance g. Additionally, the slight decay of the modulation frequencies at higher currents, which can be seen in Figure 4.17, needs further investigation. One reason might be the variation of the general shape of the longitudinal profiles for different bunch currents, which might influence the previously estimated modulation frequencies. Especially the relation to the bunch length σ_z should be carefully considered.

4.5. Cluster Label Spectrogram

As illustrated in Sections 4.1.2 and 4.2.2, the temporal sequence of cluster labels $y(t_i)$ is strongly correlated to the emitted CSR power $P_{csr}(t_i)$. This motivated an investigation of the frequencies with which these different cluster labels occur. Such findings can then be compared to the CSR power spectrogram in Figure 4.1. However, the temporal sequence of cluster labels $y(t_i)$ represents the time series of a categorical variable. In contrast to the CSR power $P_{csr}(t_i)$, the spectral analysis of such a signal is not supposed to be done by employing a simple Fourier transformation. The cluster labels y assigned by the implementation of the k-means method in the scikit-learn package consist of k integers with $y \in \{0, 1, \dots, k-1\}$. Theoretically, this cluster assignment could be denoted in many other ways, e.g. $\{a, b, c, \dots\}$ instead. Using integers is just a convenient way to do this

in computers. Additionally, the assignment of a specific label y to a found cluster C_i, e.g. $y = 0$ for the first cluster C_0, is completely arbitrary. In fact, all mappings of the clusters $\{C_0, C_1, \ldots, C_{k-1}\}$ to the used cluster labels $y \in \{0, 1, \ldots, k - 1\}$ are equally justified due to the categorical nature of the clustering information. The particular mapping obtained by applying the k-means method as implemented in Ref. [28] is due to the mapping of the randomly chosen initial cluster centers. Therefore, the sequence of cluster labels $y(t_i)$ should not be treated as a numeric signal, but as that of a categorical variable. However, it is still possible to conduct a simple Fourier transformation of the integer sequences, which in this case, yields quite similar results (shown in Appendix A.4).
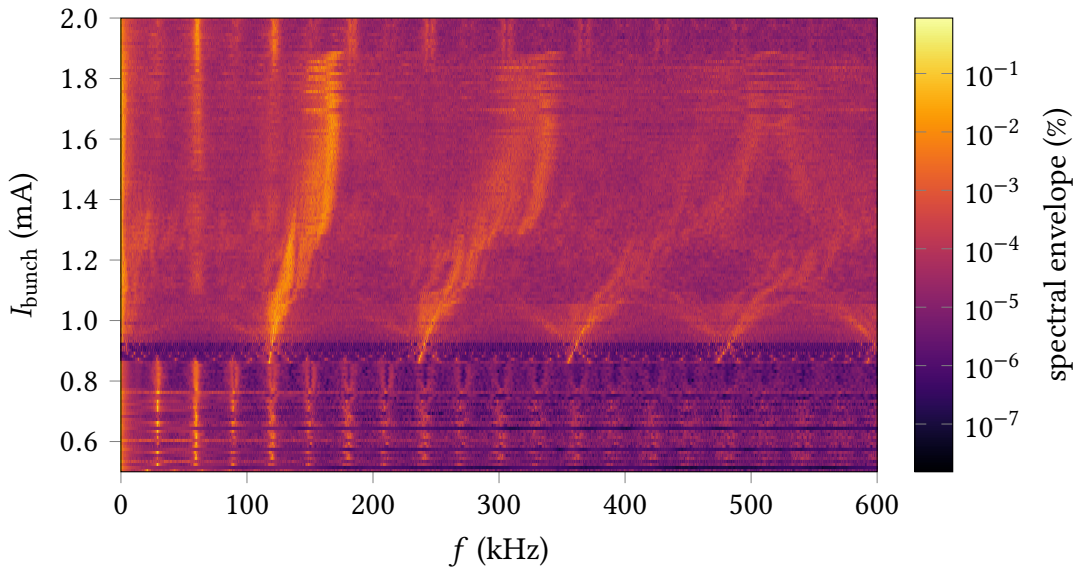

Figure 4.20.: Cluster label spectrogram for $k = 4$. The spectral envelope, as introduced in Section 4.5, is calculated for the temporal sequences of cluster labels $y(t_i)$ generated by applying the k-means method to the longitudinal profiles of all 151 bunch currents I_{bunch}. This yields a spectrogram similar to the CSR power spectrogram displayed in Figure 4.1.

One way to consider the categorical nature of the sequence of cluster labels $y(t_i)$, is by calculating the spectral envelope as proposed by Stoffer et al. in Ref. [36]. This spectral envelope is a frequency-based principal components technique, which can be applied to multivariate time series. It can especially be used to discover periodic components in categorical time series. This is achieved by considering all possible scalings $\boldsymbol{\beta} \in \mathbb{R}^k$ of the present categories C_i to numeric values. Dependent on the particular scaling, one obtains the real-valued time series $y(t_i; \boldsymbol{\beta})$ and the corresponding spectral density $f_y(\omega; \boldsymbol{\beta})$. Now, for the spectral envelope $\lambda(\omega)$, the scaling $\boldsymbol{\beta}$ is chosen to maximize the power at each frequency ω relative to the total power $\sigma^2(\boldsymbol{\beta}) = \text{var}\{y(t_i; \boldsymbol{\beta})\}$:

$$\lambda(\omega) = \max_{\boldsymbol{\beta}} \left\{ \frac{f_y(\omega; \boldsymbol{\beta})}{\sigma^2(\boldsymbol{\beta})} \right\} . \tag{4.10}$$

This means, $\lambda(\omega)\mathrm{d}\omega$ represents the largest portion of the total power which can be attributed to the frequencies $(\omega, \omega + \mathrm{d}\omega)$ for any particular scaled time series $y(t_i; \boldsymbol{\beta})$. There-

fore, $\lambda(\omega)$ envelopes the standardized spectrum of any scaled time series $y(t_i; \boldsymbol{\beta})$, i.e. given any scaling $\boldsymbol{\beta}$, which is normalized so that $y(t_i; \boldsymbol{\beta})$ has total power one, it yields $f_y(\omega; \boldsymbol{\beta}) \leq \lambda(\omega)$.

The spectral envelope can be calculated in R statistical language [29] by employing the code provided by Shumway and Stoffer in Ref. [37]. Figure 4.20 displays the results of applying this code to all the cluster label sequences $y(t_i)$ obtained when searching for $k = 4$ clusters for each of the 151 bunch currents I_{bunch}. The dominant frequencies in the CSR power signal $P_{\text{csr}}(t_i)$ as displayed in Figure 4.1 are reproduced remarkably well. This includes not only the regular bursting frequency at $f_{\text{reg}} = 117.6\,\text{GHz}$ and its higher harmonics, but also the more complex behavior in the sawtooth bursting regime above. The repetitive vertical lines below the threshold $I_{\text{th}} = 0.87\,\text{mA}$ display multiples of the synchrotron frequency $f_{\text{s}} = 30\,\text{kHz}$. As there are no other explicit dynamics altering the longitudinal bunch profiles in this range of bunch currents, the clusters found by applying the k-means method emphasize the slight differences caused by the synchrotron oscillation. It should be noted, the changes due to the periodical shifts of the center of mass position caused by the synchrotron oscillation were already mitigated by the re-centering procedure explained in Section 3.4.

Eventually, the cluster label spectrogram in Figure 4.20 verifies one more time the strong correlation of the sequence of assigned cluster labels $y(t_i)$ and the CSR power signal $P_{\text{csr}}(t_i)$. This proves the categorization, provided by applying the k-means method on the longitudinal bunch profiles, a reasonable approximation of the underlying longitudinal dynamics and the corresponding radiation behavior.

5. Extensive Analysis of Further Characteristics

The procedures and techniques discussed in the previous chapter can in principle be applied to the energy profiles $\rho(E)$ as well, which is discussed in the first part of this chapter. Beyond that, the chapter provides a compilation of further characteristics examined in the context of studying the longitudinal bunch profiles $\rho(z)$ and the emitted CSR power. This includes an investigation of the dynamics of the charge density at a specific position z_{loc} within the electron bunch. Moreover, the additional low current bursting regime, appearing for specific machine settings, is studied by employing the previously derived methods. Finally, a bench mark test determining the signal-to-noise ratio, necessary in order to reproduce the found results on measured data, is presented.

5.1. Energy Profiles

As mentioned in Section 2.1.5, the energy profile $\rho(E)$ is the projection of the longitudinal phase space density $\varphi(z, E)$ onto the E-axis:

$$\rho(E) = \int \varphi(z, E)\mathrm{d}z \ . \tag{5.1}$$

This means, the energy profiles $\rho(E, t_i)$ for a specific bunch current I_{bunch} correspond to the same phase space densities $\varphi(z, E, t_i)$, illustrated for example in Figure 4.14, as the longitudinal bunch profiles $\rho(z, t_i)$. Therefore, it can be expected that the energy profiles display similar modulations as explored above. Figure 5.1 shows the cluster centers found by applying the k-means method to the energy profiles $\rho(E, t_i)$ for the case of $I_{\mathrm{reg}} = 0.88\,\mathrm{mA}$ and $k = 4$ referenced to the global mean of energy profiles with this current:

$$\overline{\rho}(E) = \frac{1}{n_{\mathrm{steps}}} \sum_{i=1}^{n_{\mathrm{steps}}} \rho(E, t_i) \ . \tag{5.2}$$

The respective cluster centers display the phase and paraphase of a modulation on the associated energy profiles as well. Similar to the longitudinal profiles, one observes an asymmetry of the modulation's amplitude along the E-axis. Here, the modulation is more prominent for low energies $E < 0$ when compared to $E > 0$. It should be noted, due to the changed scaling of the respective vertical axis, the modulation's amplitude is not directly comparable with the one displayed in e.g. Figure 4.4. In the case of $I_{\mathrm{reg}} = 0.88\,\mathrm{mA}$, an increased cluster number of $k = 4$ yields modulation states which are slightly shifted along the E-axis, rather than the previously found intermediate states with lower amplitude. This
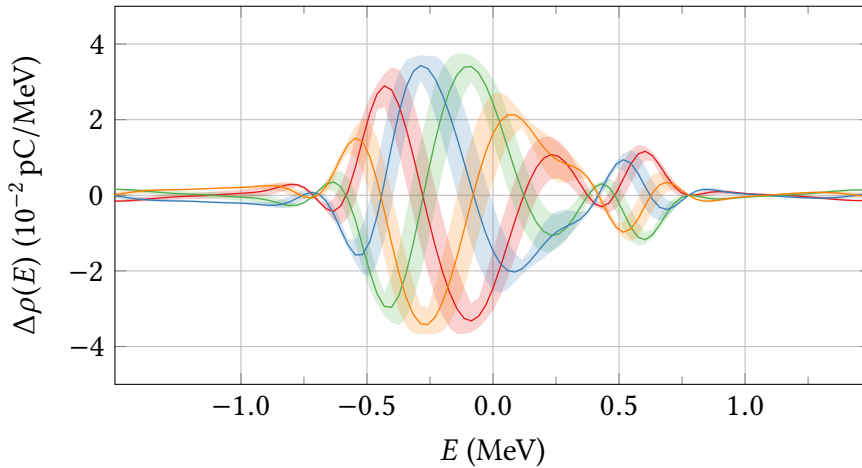
Figure 5.1.: Referenced cluster centers found on the energy profiles with bunch current $I_{reg} = 0.88\,\text{mA}$. After subtracting the global mean $\overline{\rho}(E)$, the cluster centers found by the k-means method while searching for $k = 4$ clusters display modulations similar to Figure 4.4. This illustration serves as an example, demonstrating the similarity of the results obtained by applying the previously derived procedures to the energy profiles instead.

is due to the altered projection of the phase space densities $\varphi(z, E, t_i)$. For these time steps t_i, the extrema of the micro-structures balance each other in the projection on the z-axis, while for the E-axis the maximum of the absolute value of the modulation amplitude remains almost unchanged.

As in the case of the longitudinal profiles, similar modulations are found throughout the various bunch currents I_{bunch} above the threshold I_{th}. Analogously to Section 4.5, the spectral analysis is conducted with respect to the categorical nature of the cluster label sequence $y(t_i)$ and shown in Figure 5.2. Even though the clusters' distributions and therefore the temporal sequences of cluster labels $y(t_i)$ are slightly different, Figure 5.2 proves the general correlation to the emitted CSR power $P_{csr}(t_i)$. Again, the results are remarkably comparable to the CSR power spectrogram displayed in Figure 4.1, considering only the categorical information of the cluster labels $y(t_i)$ is used.

Eventually, it is found that the modulations displayed on the longitudinal bunch profiles are slightly more distinct and have an overall more sinusoidal shape than those on the energy profiles. This facilitates the analysis of the frequencies corresponding to the micro-structures in the longitudinal phase space. Additionally, it is worth mentioning that the application of the k-means method to the energy profiles $\rho(E, t_i)$ required an occasionally higher number of clusters k in order to reveal the presence of the modulations caused by micro-structures in the longitudinal phase space. Nevertheless, this section serves as a proof of concept for the application of the methods derived in the context of this thesis to the temporal sequence of energy profiles $\rho(E, t_i)$ as well.
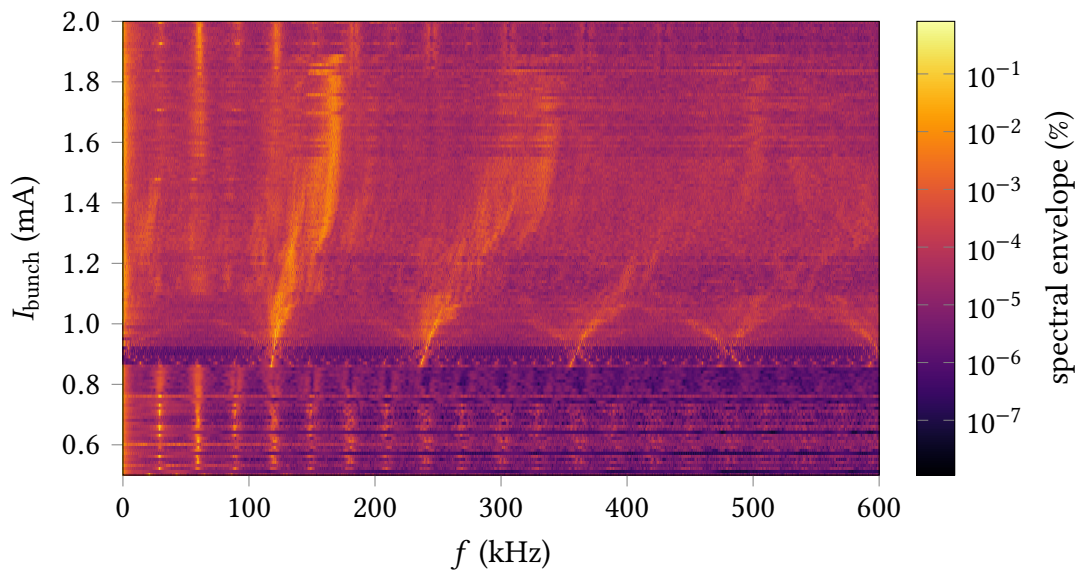
Figure 5.2.: Cluster label spectrogram as obtained for the energy profiles with cluster number $k = 4$. Analogously to Figure 4.20, the spectral envelope of each temporal sequence of cluster labels $y(t_i)$ for all 151 bunch currents I_{bunch} is calculated and displayed above.

5.2. Dynamics of a Localized Charge Density

As shown in Chapter 4, the temporal sequence of cluster labels $y(t_i)$ is strongly correlated to the emitted CSR power $P_{\text{csr}}(t_i)$. The respective cluster centers display varying modulation states on the longitudinal profiles. This motivated the subsequent investigation of the dynamics of a localized charge density $\rho(z_{\text{loc}}, t_i)$. As illustrated in the left part of Figure 5.3, the charge density, i.e. the value of the longitudinal bunch profile $\rho(z)$ at a particular position z_{loc} within the bunch, is observed over time. The right part of the Figure 5.3 shows the such obtained signal for the case of $I_{\text{reg}} = 0.88\,\text{mA}$ and $z_{\text{loc}} = 0$, i.e. the center of mass position. The strcuture of the observed signal resembles the corresponding CSR power P_{csr}, as displayed in Figure 4.5. This is quite expected as, according to Eq.(2.17), the emitted CSR depends on the longitudinal form factor $\mathcal{F}_z(k_z)$ introduced in Eq. (2.19) and therefore the longitudinal bunch profile $\rho(z)$. However, it should be pointed out, only one of the $n_{\text{grid}} = 200$ points approximating the longitudinal profile $\rho(z)$ is considered, which yields no information about the overall shape of the electron bunch. Additionally, it should be noted, due to the applied re-centering procedure, the position z_{loc} is here defined with respect to the center of mass position μ_z, see Eq. (3.1). Though similar results are obtained when the position is given with respect to the synchronous particle.

In order to study the current-dependency of the such obtained signal $\rho(z_{\text{loc}}, t_i)$, this is calculated for all 151 bunch currents I_{bunch} for a fixed value z_{loc}. Subsequently, these signals are Fourier transformed to enable the comparison with the CSR power spectrogram in Figure 4.1. The results at the center of mass position $z_{\text{loc}} = 0$ are shown in Figure 5.4.

Apparently, the charge density at the center of mass position is strongly correlated to the corresponding emitted CSR power. In fact, when compared with Figure 4.1, the two
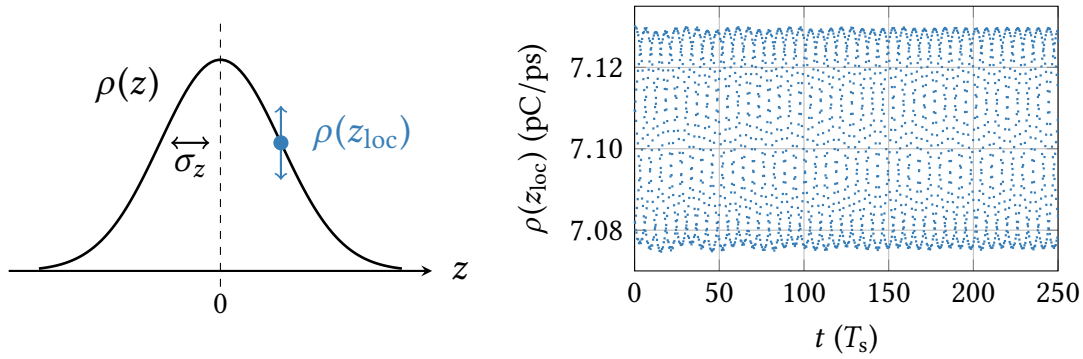
Figure 5.3.: Localized charge density $\rho(z_{\text{loc}})$. (Left) The fluctuation of the charge density, i.e. the value of the longitudinal profile $\rho(z_{\text{loc}})$ at a particular position z_{loc} within the electron bunch is studied over time. (Right) The such obtained signal for $I_{\text{reg}} = 0.88\,\text{mA}$ and $z_{\text{loc}} = 0$ resembles the CSR power displayed in Figure 4.5. It should be noted, here, $z_{\text{loc}} = 0$ marks the center of mass position due to the previously explained re-centering procedure.

spectrograms appear nearly identical. Similar results are obtained by studying $\rho(z_{\text{loc}}, t_i)$ for positions close to the center of mass, i.e. $-10\,\text{ps} < z_{\text{loc}}/c < 10\,\text{ps}$. However, approaching the head or tail of the electron bunch, i.e. at the very edges of the longitudinal bunch profiles $|z_{\text{loc}}/c| > 15\,\text{ps}$, the results are quite different. Figure 5.5 displays the spectrogram obtained for $\rho(z_{\text{loc}}, t_i)$ at the position $z_{\text{loc}}/c = 14.91\,\text{ps}$. Here, only the regular bursting frequency $f_{\text{reg}} = 117.6\,\text{kHz}$ right above the threshold $I_{\text{th}} = 0.87\,\text{mA}$ is clearly visible. While its second harmonic $f = 2\,f_{\text{reg}}$ can still be identified, the higher harmonics are not recognizable. Additionally, the complex structure in the above sawtooth bursting regime is merely indicated. However, it is worth mentioning, the low-frequency contributions starting at $I_{\text{bunch}} = 0.94\,\text{mA}$ are still represented.

These findings can be explained by the declining amplitude A_{mod} of the modulations found in Chapter 4 along the z-axis. As previously illustrated, the fluctuations of the CSR power signal P_{csr} are mainly caused by micro-structures in the longitudinal phase space and therefore modulations on the longitudinal bunch profiles. The micro-structures displayed in Sections 4.1.1 and 4.2.1 are all quite prominent near the center of mass position while their amplitude drops off considerably, when approaching the edges of the longitudinal profiles. Therefore, the dynamics found for $|z_{\text{loc}}/c| > 15\,\text{ps}$ are mainly effects of the synchrotron oscillation, leading to the parallel vertical lines at $f = n\,f_{\text{s}}$.

Eventually, it has to be stated that the dynamics found for the localized charge densities $\rho(z_{\text{loc}}, t_i)$ near the center of mass position are surprisingly similar to the behavior of the CSR power $P_{\text{csr}}(t_i)$ signal, although no information is given about the overall shape of the electron bunch. It should be pointed out, the CSR power P_{csr} denotes the integral over the coherently emitted radiation power per unit frequency $\mathrm{d}P_{\text{csr}}/\mathrm{d}\omega$, according to Eqs. (2.17) and (2.29). Here, $\mathrm{d}P_{\text{csr}}/\mathrm{d}\omega$ depends on the charge density distribution via the longitudinal form factor $\mathcal{F}_z(k_z)$, which is the square of the absolute value of the Fourier transformed longitudinal bunch profile $\rho(z)$. Therefore, given $\rho(z_{\text{loc}})$ and P_{csr} are such
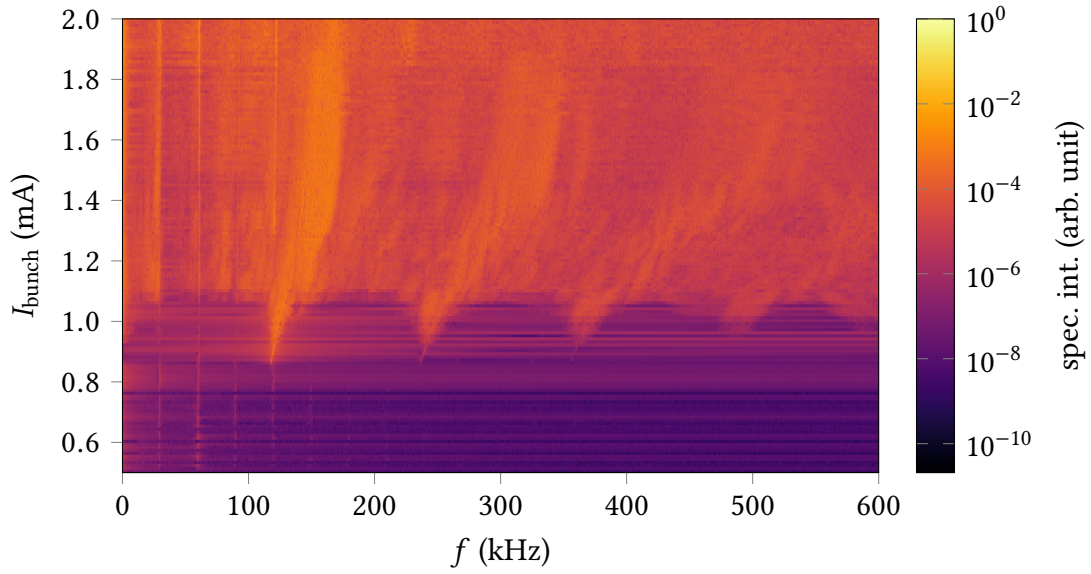
Figure 5.4.: The localized charge density $\rho(z_{\text{loc}}, t_i)$ at the particular position $z_{\text{loc}} = 0$ and at different times t_i are Fourier transformed and displayed as horizontal lines in the above spectrogram. This yields quite similar results to the CSR power spectrogram in Figure 4.1.
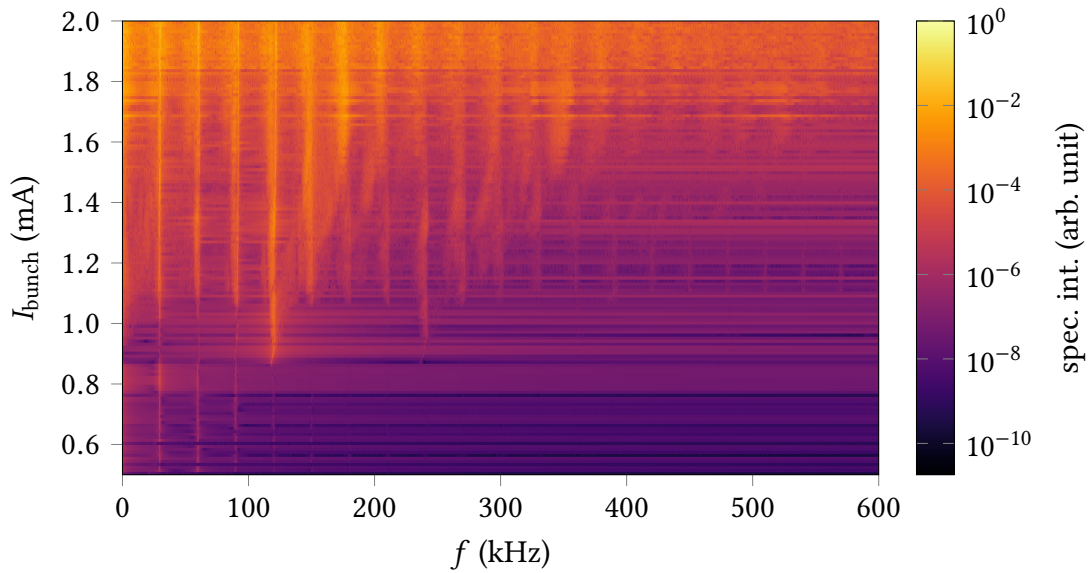

Figure 5.5.: For localized charge densities at positions further distant from the center of mass, here $z_{\text{loc}}/c = 14.91\,\text{ps}$, the obtained spectrogram deviates from the one displayed in Figure 5.4. Especially multiples of the synchrotron frequency $f_{\text{s}} = 30\,\text{kHz}$ are dominating.

different physical quantities, the previously illustrated correlations are not evident and need further investigation.

However, these results might be quite useful considering the measurement of the longitudinal profiles $\rho(z)$ at synchrotron light sources. The accuracy at a fixed position z_{loc} can be considerably higher than otherwise achievable. In other words, obtaining the charge density at one particular longitudinal position with high accuracy can still provide valuable information in order to study the dynamics of interest.

5.3. Low Current Bursting Regime

Occasionally, fluctuations of the CSR power signal below the estimated threshold I_{th} are observed at ANKA. These are similar in appearance to the previously discussed regular bursting regime, but are specifically occurring at low currents. Therefore, for the context of this thesis, it is called low current bursting regime.
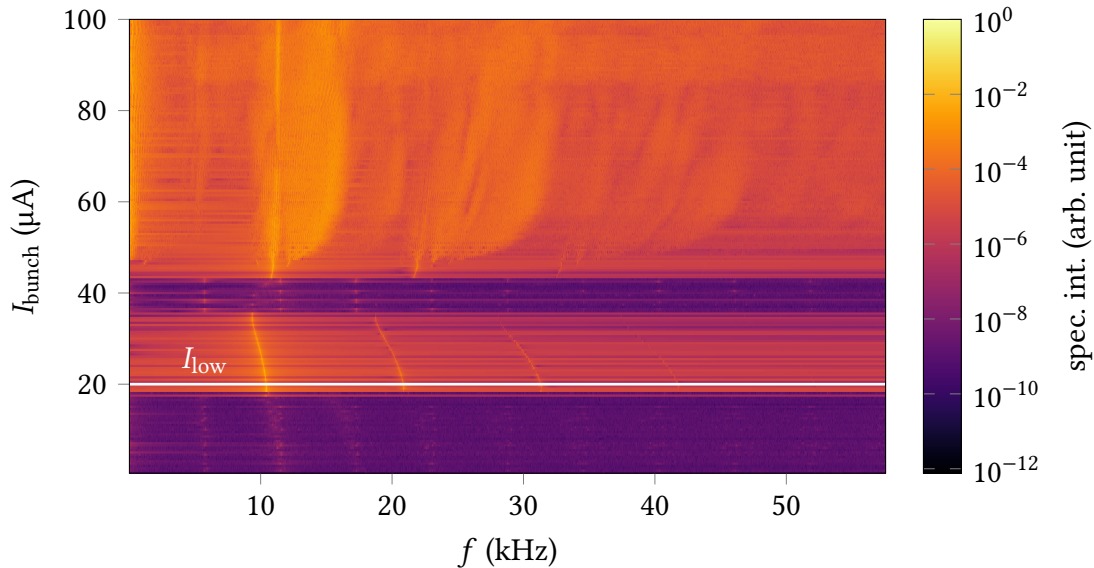

Figure 5.6.: Shown is the CSR power spectrogram obtained for the parameter settings specified in Table 5.1. Below the threshold at $I_{\text{th}} = 43.5\,\mu\text{A}$, there is an additional regime of fluctuating CSR emission visible, between $I_{\text{bunch}} = 18.5\,\mu\text{A}$ and $I_{\text{bunch}} = 35.5\,\mu\text{A}$. Due to its occurrence at relatively low bunch currents, this is called low current bursting regime in this thesis. Exemplary results for this regime are shown in Figures 5.7 and 5.8.

One of the additional data sets studied during this thesis, was deliberately chosen to display such low current bursting. The altered parameter settings used to generate this data set can be found in Table 5.1. Here, the simulated bunch currents I_{bunch} vary from $0.5\,\mu\text{A}$ to $100\,\mu\text{A}$, with an equidistant step size of $\Delta I_{\text{bunch}} = 0.5\,\mu\text{A}$, yielding a total of 200 different currents. To deal with the in Section 3.2 mentioned transition oscillation, the simulated data for a time period of $t_{\text{transition}} \approx 3000\,T_{\text{s}}$ is neglected, before the actual data set for a duration of $t = 500\,T_{\text{s}}$ is generated.

Table 5.1.: Simulation parameters used to generate an additional data set displaying low current bursting. The bunch currents I_{bunch} are varied between $0.5\,\mu A$ and $100\,\mu A$. To deal with the transition oscillation mentioned in Section 3.2, the simulated data for the initial $t_{\text{transition}} \approx 3000\,T_{\text{s}}$ is neglected.

Physical parameter	Value
RF voltage U_0	$1.3\,\text{MV}$
revolution frequency f_{rev}	$2.72\,\text{MHz}$
synchrotron frequency f_{s}	$5.76\,\text{kHz}$
damping time τ_{d}	$2.66\,\text{ms}$
harmonic number h	184
parallel plates distance g	$3.2\,\text{cm}$
initial electron distribution $\varphi(z, E, t_0)$	2-dim. Gaussian
simulation time t	$500\,T_{\text{s}}$
bunch current I_{bunch}	$0.5\,\mu A$ to $200\,\mu A$

Control parameter	Value
grid size n_{grid}	256
time steps n_{steps}	10 000

The obtained CSR power spectrogram for this data set is shown in Figure 5.6. Similarly to Figure 4.1, there is a distinct line at f_{reg} and its higher harmonics above the threshold at $I_{\text{th}} = 43.5\,\mu A$, indicating the regular bursting regime. For higher bunch currents, the more complex structure of the sawtooth bursting regime is displayed as well. However, for bunch currents between $I_{\text{bunch}} = 18.5\,\mu A$ and $I_{\text{bunch}} = 35.5\,\mu A$, there is an additional regime of fluctuating CSR emission visible.

Due to the modified parameter settings, applying the previously derived methods to the longitudinal bunch profiles in the regular and sawtooth bursting regime yields slightly different results than in Chapter 4. This means, the found micro-structures in the longitudinal phase space and the corresponding modulations on the longitudinal profiles have a slightly different appearance. This includes for example the number of distinct structures displayed in the longitudinal phase space. While in Sections 4.1.3 and 4.2.3 roughly five separate structures or peaks are displayed, there are merely three present in the longitudinal phase space densities of this data set. However, the general dynamics are quite comparable. For the regular bursting regime this means, alternating phases of the modulations corresponding to distinct structures rotating in the longitudinal phase space are found as well. These cause a sinusoidal CSR power oscillating with the dominant frequency f_{reg}. In the sawtooth bursting regime, the relatively long sections displaying a bunch shortening process are also present. Between these, there are sawtooth shaped bursts of the emitted CSR power P_{csr} which are caused by distinct micro-structures of relatively high amplitude in the longitudinal phase space.
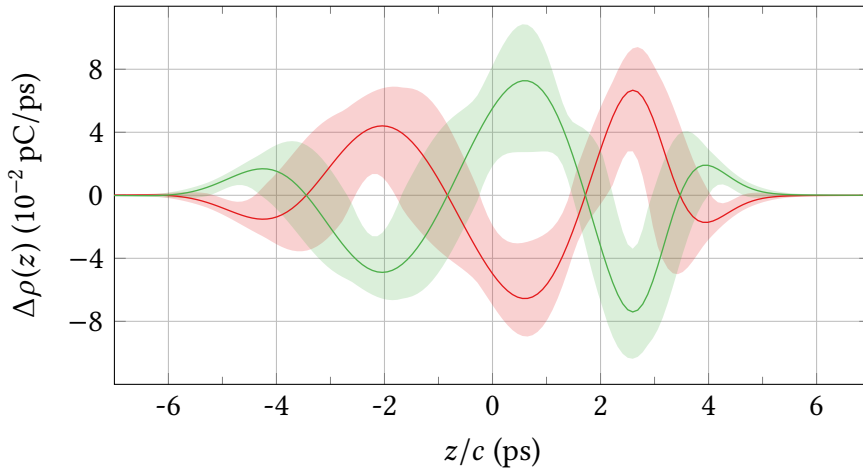
Figure 5.7.: Shown are the referenced cluster centers found when searching for $k = 2$ clusters in the longitudinal profiles with bunch current $I_{\text{low}} = 20\,\mu\text{A}$. It should be noted, the modulation is displayed with more than 1.5 periods indicating micro-structures rather than deviating bunch lengths σ_z.

The results obtained in the low current bursting are fairly comparable to the dynamics of the regular bursting regime. This is illustrated in Figure 5.7, where the two referenced cluster centers found for $I_{\text{low}} = 20\,\mu\text{A}$ and $k = 2$ are displayed. At first glance, one might relate these findings to the effects of deviating bunch lengths σ_z as the modulation looks similar to the illustration in Figure 4.10. However, it should be noted, there are clearly more than 1.5 periods displayed, indicating micro-structures in the longitudinal phase space.
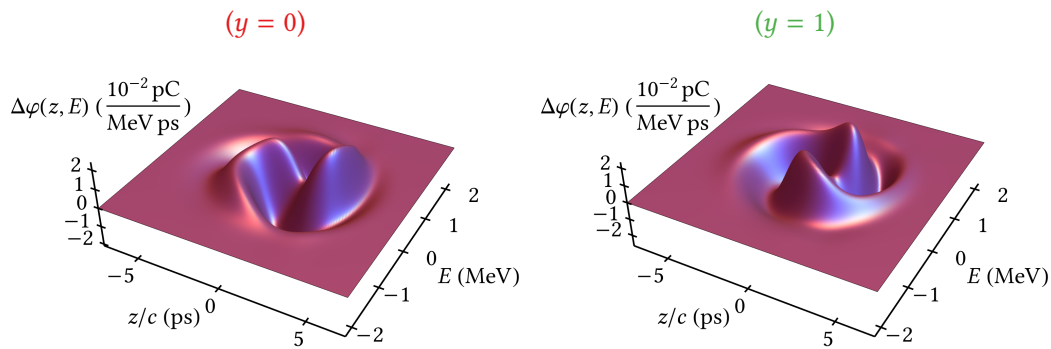

Figure 5.8.: Referenced phase space cluster means for the case of $I_{\text{low}} = 20\,\mu\text{A}$ and $k = 2$. While three separate structures or peaks are found at higher bunch currents, in the low current bursting regime, there are only two micro-structures visible.

This can be confirmed by studying the corresponding phase space cluster means in Figure 5.8. Now, the interesting part about this low current bursting regime is the fact, that there are only two separate structures or peaks present in the longitudinal phase space. While the modulations displayed in Figure 5.7 are slightly different as well, this is a drastic

change compared to the three micro-structures observed for higher bunch currents. This renders the low current bursting regime an interesting subject for further research in order to understand the micro-structure dynamics which are causing the general phenomenon of a bursting CSR emission. The explanation of why an additional micro-structure is appearing for higher bunch currents might lead one step closer to understanding, why these micro-structures are appearing in the first place.[1]

5.4. Signal-to-Noise Ratio Benchmark Tests

All data sets studied in this thesis were exclusively generated with the in Section 3.1 introduced simulation code Inovesa. As aforementioned, the such obtained longitudinal phase space densities $\varphi(z, E, t_i)$ and longitudinal bunch profiles $\rho(z, t_i)$ are of very low noise, which are ideal conditions for the application of the k-means method. It was already mentioned in Section 2.2.2, the k-means method can be prone to noise and outliers, as they can substantially influence the mean value, whose calculation represents the very basis of the k-means procedure.
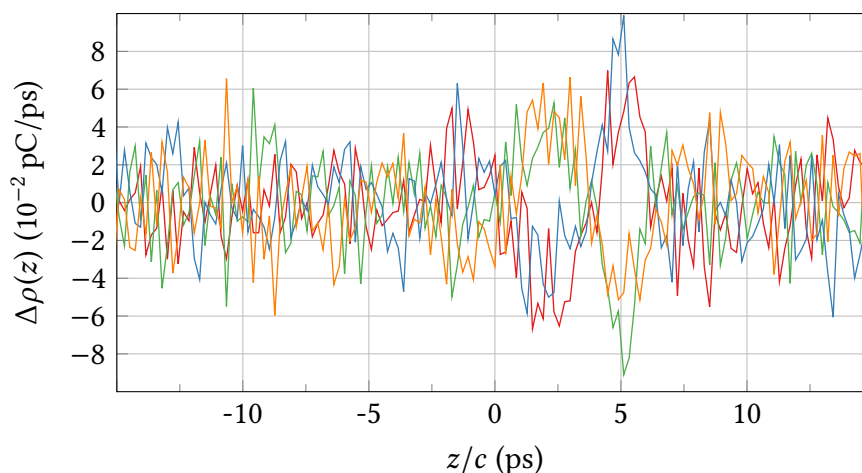

Figure 5.9.: In order to study the effects of considerably higher noise levels in measured data, the simulated longitudinal profiles are modified by adding normally distributed noise to each value $\rho(z)$. Subsequently, the k-means method is applied. Shown are the results for the case of $I_{\mathrm{reg}} = 0.88\,\mathrm{mA}$ and $k = 4$ with a signal-to-noise ratio of SNR = 30. In contrast to Figure 4.4, the within cluster standard deviations are not shown as they exceed the limits of the vertical axis considerably.

As longitudinal bunch profiles measured in experiments can exhibit considerable higher noise levels, reproducing the previous results on measured data can be quite challenging. Therefore, a bench mark test is conducted estimating the signal-to-noise ratio required to reproduce the previously illustrated results on measured data. The signal-to-noise ratio is

---

[1] In addition, the current-dependent modulation frequency f_{mod} and amplitude A_{mod} for this data set are shown in Appendix A.5.

defined as:

$$\text{SNR} = \frac{P_{\text{signal}}}{P_{\text{noise}}} \ . \tag{5.3}$$

It should be pointed out, the signals of interest in this case are the modulations on the longitudinal profiles displaying micro-structures in the longitudinal phase space, and not their roughly Gaussian shape. However, to enable the comparison with the estimated signal-to-noise values in measurements, the signal strength P_{signal} is approximated by the maximum value of the total cluster centers $\rho_C(z)$. This enables additionally the comparison of different bunch currents I_{bunch} as the respective maxima of the found cluster centers are in the same order of magnitude. As there always are several cluster centers and therefore signal strengths P_{signal} to choose from, only the highest value is considered. Subsequently, the corresponding noise level is given by:

$$P_{\text{noise}} = \frac{\max\{\rho_C(z)\}}{\text{SNR}} \ . \tag{5.4}$$

In order to study the effects on the results of the application of the k-means method, normally distributed noise with $\sigma = P_{\text{noise}}$ is added to all $n_{\text{grid}} = 200$ points of each longitudinal profile $\rho(z)$.
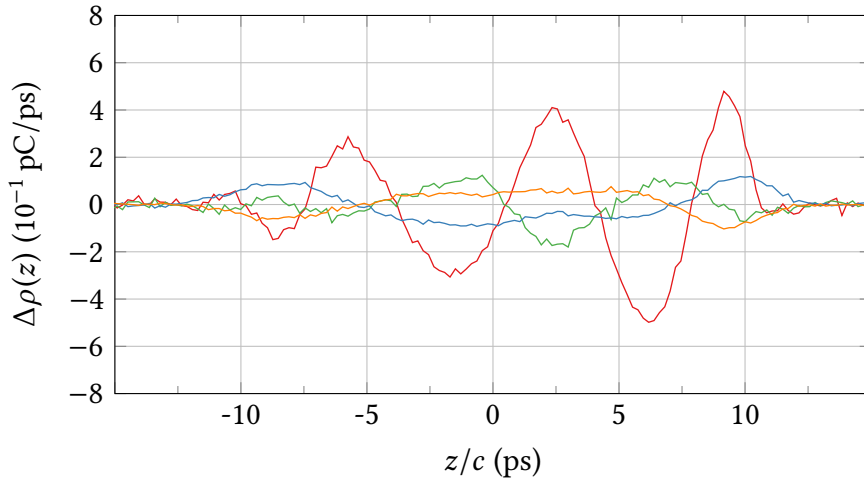

Figure 5.10.: Shown are the results of applying the k-means method with $k = 4$ to the longitudinal profiles modified by adding normally distributed noise for the case of $I_{\text{saw}} = 1.15\,\text{mA}$ and a signal-to-noise ratio of SNR = 30. Compared to Figure 5.9, the modulation amplitude A_{mod} is roughly ten times higher. This means, reproducing the findings for this bunch current $I_{\text{saw}} = 1.15\,\text{mA}$ on measured longitudinal profiles might be considerably easier.

Applying the k-means method with $k = 4$ to the such modified longitudinal profiles for the bunch current $I_{\text{reg}} = 0.88\,\text{mA}$ with SNR = 30, yields the results displayed in Figure 5.9. The within cluster standard deviations are not shown in this illustration as they go far beyond the limits of the vertical axis. The differences to Figure 4.4 are clearly visible. Due to the small amplitude of the modulations found in the regular bursting regime, the

added noise is substantially influencing the results obtained by applying the *k*-means method. Additionally, the individual found referenced cluster centers display small and fast oscillations as an effect of the added noise. Therefore, the previously found modulation phase and paraphase are merely indicated.

However, applying the same procedure to the longitudinal profiles in the sawtooth bursting regime yields different results. Figure 5.10 shows the referenced cluster centers for $I_{saw} = 1.15\,\text{mA}$, $k = 4$ and SNR = 30. Here, the modulation amplitude A_{mod} is roughly ten times higher than for $I_{reg} = 0.88\,\text{mA}$. Therefore, the red referenced cluster center displays the found micro-structures, although the corresponding paraphase is barely recognizable. Here, the micro-structures are already indicated for lower signal-to-noise ratios SNR < 30. However, for this benchmark test it is already clear, what signal to expect and where to look for it, which might not be the case for the application to actual measured data. Due to this bias, the signal-to-noise ratio SNR = 30 is considered a reasonable target value in order to reproduce similar results on measured longitudinal profiles.

First attempts to reproduce the previously discussed results on measured data taken with the electro-optical setup at ANKA [12] were not successful. As the corresponding signal-to-noise ratio is below the above estimated required value of SNR = 30, this is quite expected. After the time when these first tests were conducted, several improvements were made to the electro-optical setup, see Ref. [38]. The results for potentially improved signal-to-noise ratios should be carefully considered.

The *k*-means method has proven a reasonable choice for the application to simulated longitudinal bunch profiles. However, as it can be prone to noise and outliers, employing different clustering methods for the analysis of measured data should be taken into consideration. For the application of different clustering methods, especially in the case of measured data, this thesis provides an illustration of the micro-structure dynamics which can be expected.

6. Summary and Outlook

In order to increase the emitted CSR power, several synchrotron light sources are deliberately operating with short electron bunches, including the ANKA storage ring at KIT. The reduction of the bunch length however, causes complex dynamics within the electron bunch and leads to the formation of dynamically changing micro-structures. In this thesis, these micro-structure dynamics have been simulated with the Vlasov-Fokker-Planck-Solver Inovesa. As this quickly accumulates to large data sets, the machine learning method k-means has been applied to the longitudinal bunch profiles. With this procedure, the dominant micro-structures within a fixed bunch current have been successfully identified. Furthermore, several visualization methods have been developed to study the characteristics of these micro-structures. Moreover, the strong correlation of the found micro-structure dynamics to the radiation behavior has been verified by various methods.

For the regular bursting regime, the cluster centers display various states of modulations caused by consistent micro-structures in the longitudinal phase space. Despite their rotation around the center and a slight asymmetry along the longitudinal and energy axis, the micro-structures are fairly stationary in the longitudinal phase space, which explains the sinusoidal shape of the emitted CSR power.

In contrast, for the sawtooth bursting regime, an additional bunch shortening process has been identified. During this process, the micro-structures are still present in the longitudinal phase space and eventually reach their maximum amplitude when the bunch shortening leads to a sawtooth shaped burst in the corresponding CSR power. After this burst, the micro-structures' amplitude is reduced again and the longitudinal profiles have a relatively long bunch length.

As the micro-structures found at different bunch currents display very similar characteristics, e.g. number of distinct structures and overall shape, the current-dependency of their scale has been analyzed. Therefor, the modulation frequencies and amplitudes on the longitudinal bunch profiles have been determined. For bunch currents below the bursting threshold, no micro-structures were found and the modulation frequencies were clarified as an effect of small deviations in the bunch lengths of the longitudinal profiles. For bunch currents higher than the bursting threshold, a nearly constant modulation frequency has been found across various bunch currents.

The previously derived techniques have been shown to be applicable to the energy profiles as well, yielding similar results. Furthermore, an additional data set displaying low current bursting has been briefly discussed. While the general findings for the regular and sawtooth bursting regime could be verified, the low current bursting regime displays considerably different results. Here, compared to the findings for higher bunch currents, one less micro-structure was found in the longitudinal phase space densities.

Finally, a SNR benchmark test was conducted, estimating the required signal-to-noise ratio in order to reproduce these results on measured data to about SNR = 30.

The continuous presence of distinct micro-structures in the longitudinal phase space within a specific bunch current as well as their similar behavior across various bunch currents are considered main results of this thesis. The micro-structures found in the regular and sawtooth bursting regime resemble each other, corresponding to nearly constant modulation frequencies on the longitudinal profiles. Further investigations by a systematic study of different accelerator parameter settings are required to verify these findings, but were beyond the scope of this thesis. Especially, the slight decay of the found modulation frequencies with increasing bunch currents should be carefully examined. As the overall shape of the longitudinal profiles, e.g. the bunch length, might change with increasing bunch currents, this can also influence the estimated value of the modulation frequency.

Additionally, the deviating bunch lengths in the sawtooth bursting regime complicate the verification of the continuous presence of the found micro-structures. Here, an additional pre-processing procedure yielding longitudinal profiles with comparable variance might be beneficial, e.g. scaling the individual longitudinal profiles with their corresponding bunch length. If the continuous presence of the micro-structures and their similarity across various bunch currents can be confirmed, the different radiation behavior for different bunch currents could be explained by the temporal changes of the micro-structures' amplitude.

While yielding reasonable results on simulation data, the used clustering method *k*-means can be quite prone to noise, as studied in the SNR benchmarks tests and is therefore not ideally suited for the application to measured data. Consequently, additional clustering methods which are more robust against influences of outliers and noise should be considered. Though, it is worth mentioning, the *k*-means method can also be applied with different norms. These can e.g. be used to balance between the few longitudinal profiles with relatively high modulation amplitude during the sawtooth shaped bursts and the many longitudinal profiles in the bunch shortening process between these bursts. As aforementioned, the *k*-means procedure can be intuitively understood, which is very beneficial to gain initial insights to the structure of the given data sets. However, more sophisticated clustering methods, or such better suited for the application to time series, should be considered as well.

Additionally, it is worth mentioning, as the resolution of the measured charge densities within the longitudinal profile can vary dependent on the longitudinal position, an additional pre-processing can be applied to put more emphasis on positions with high accuracy and to neglect such with very low accuracy. For the example of the *k*-means method, this could be achieved by scaling the total variance for the individual positions dependent on the respective confidence level. Subsequently, the such obtained clusters can be studied for the original longitudinal profiles.

Systematic studies of the influence of different accelerator parameter settings on the micro-structure dynamics were beyond the scope of this thesis. However, the presented techniques provide the opportunity to examine their dependence on specific physical quantities, e.g. the parallel plates distance g (corresponding to the vacuum chamber height in real accelerators, see Appendix A.6) or the bending radius R. Especially the dependence of the modulation frequency, i.e. the micro-structures' scale on these parameters should be carefully examined. An investigation of these dependencies might lead to additional

insights into the underlying dynamics and provide first basic relations regarding an analytical description.

The illustrated phase space densities in this thesis display consistent micro-structures. Despite their rotation around the center and slight asymmetries along the longitudinal and energy axis, these micro-structures are fairly stationary. Consequently, it has been learned from this thesis, a direct investigation of the longitudinal phase space densities might provide further insights to the underlying dynamics and should be considered as well. In principle, the k-means method can similarly be applied to the longitudinal phase space densities as well. Considering the experimental observation, the longitudinal phase space is very difficult to access. However, new measurement techniques will be employed at ANKA using tomography algorithms, which might provide additional opportunities for the future.

For any particular case of further investigations, this thesis presents first direct insights to the micro-structure dynamics appearing for short electron bunches. It provides several basic techniques to analyze and visualize these micro-structures, as well as their correlation to the emitted coherent synchrotron radiation for future systematic studies.

A. Appendix

A.1. Transition Oscillation

As mentioned in Section 3.2, the initial electron distribution $\varphi(z, E, t_0)$ has to be manually chosen for Vlasov-Fokker-Planck-Solvers and can not be calculated analytically. Therefore, in this thesis, $\varphi(z, E, t_0)$ is approximated by a two-dimensional Gaussian and given as an input to Inovesa. This procedure leads to a transition oscillation, which is illustrated by the CSR power signal in Figure A.1. For the generated data sets, this issue is dealt with by neglecting the initial $t \geq 1000\, T_\mathrm{s}$.
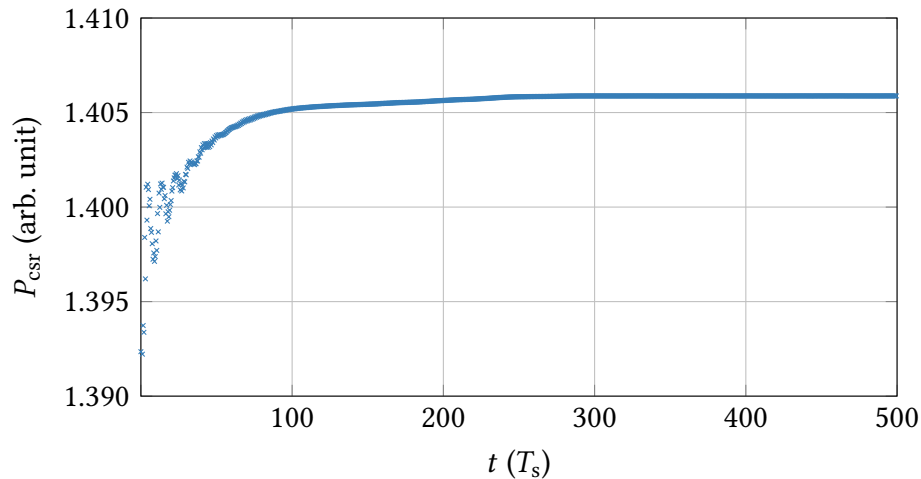
Figure A.1.: Shown is the simulated CSR power signal for the parameter settings in Table 5.1 and the bunch current $I_\mathrm{bunch} = 11.5\,\mathrm{\mu A}$ from $t = 0$ to $t = 500\, T_\mathrm{s}$. Especially, during the first 50 synchrotron periods there are small fluctuations visible due to the previously mentioned transition oscillation. In order to mitigate this effect, at least the first one thousand synchrotron periods are neglected.

A.2. Low Frequency Contributions in the CSR power spectrogram

In the sawtooth bursting regime, studied in Chapter 4 for the exemplary bunch current $I_{\text{saw}} = 1.15\,\text{mA}$, the emitted CSR power displays several sawtooth shaped bursts. The frequency with which these occur ($f_{\text{saw}} \approx 1\,\text{kHz}$) is barely visible in the corresponding horizontal line in the CSR power spectrogram (see Figure 4.1). Therefore, the same CSR power spectrogram is shown in Figure A.2 with a logarithmically scaled frequency axis. These low frequency contributions are appearing for bunch currents higher than $I_{\text{bunch}} = 0.94\,\text{mA}$ and mark the end of the regular bursting regime below.
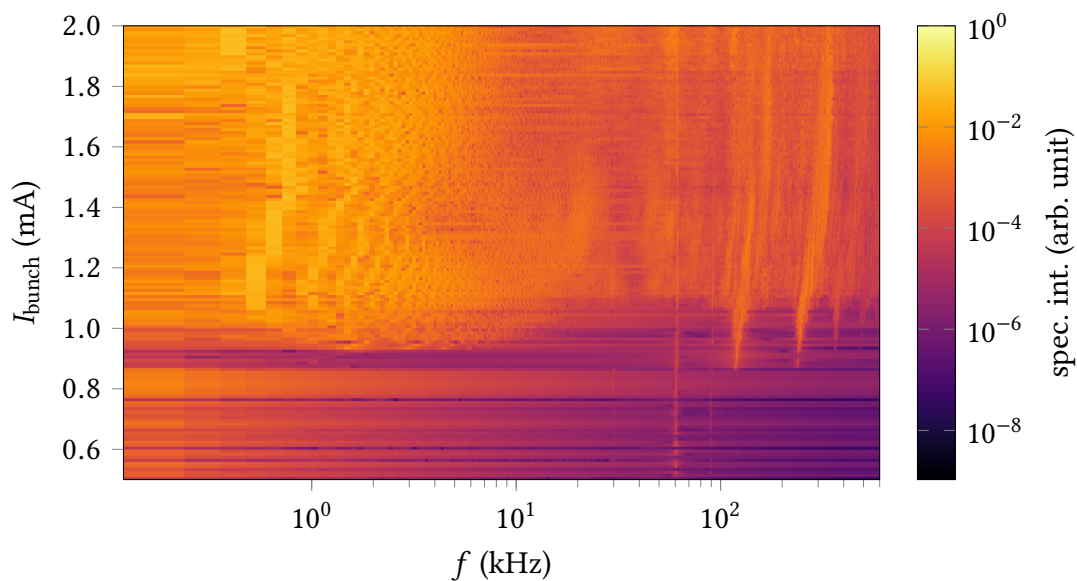
Figure A.2.: The same CSR power spectrogram as displayed in Figure 4.1 is shown again with a logarithmically scaled frequency axis. Here, the low frequency contributions with $f_{\text{saw}} \approx 1\,\text{kHz}$, which are causing the sawtooth shaped CSR power signal in the sawtooth bursting regime, are clearly visible.

A.3. Statistical Moments in the Sawtooth Bursting Regime

To further illustrate the bunch shortening process found in the sawtooth bursting regime in Chapter 4, the corresponding bunch lengths $\sigma_z(t_i)/c$ for the given time steps t_i are shown in Figure A.3. Analogously to the CSR power in Section 4.2.2, each displayed value is colored according to the corresponding cluster labels $y(t_i)$.
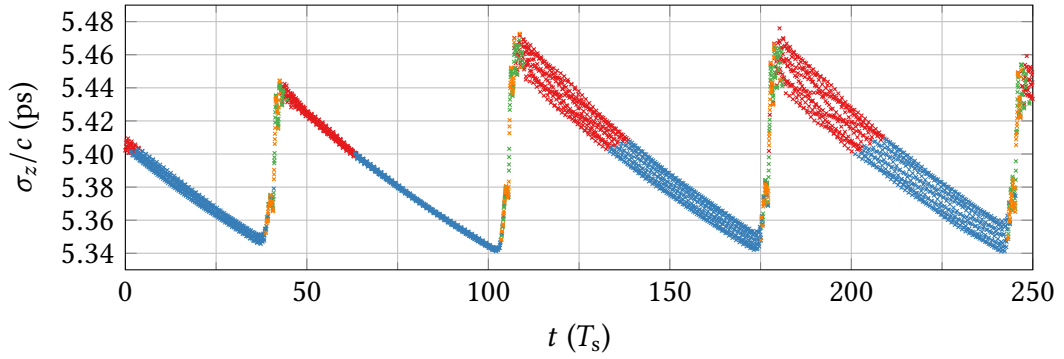

Figure A.3.: Displayed are the bunch lengths $\sigma_z(t_i)/c$ for the bunch current $I_{\mathrm{saw}} = 1.15\,\mathrm{mA}$. The value of $\sigma_z(t_i)/c$ for each time step t_i is colored according to the associated cluster labels $y(t_i)$.

Additionally, during this bunch shortening process, e.g. between $t \approx 50\,T_{\mathrm{s}}$ and $t \approx 100\,T_{\mathrm{s}}$, the longitudinal bunch profiles $\rho(z)$ show a changing skewness s_z:

$$s_z = \frac{\mu_{z,3}}{\sigma_z^3} \,, \tag{A.1}$$

where $\mu_{z,3}$ denotes the third statistical moment of the longitudinal bunch profile $\rho(z)$. This is illustrated in Figure A.4. The decreasing negative values during the bunch shortening process indicate, the longitudinal bunch profiles are leaning more and more toward the head of the bunch until a sawtooth shaped burst of CSR emission is reached.
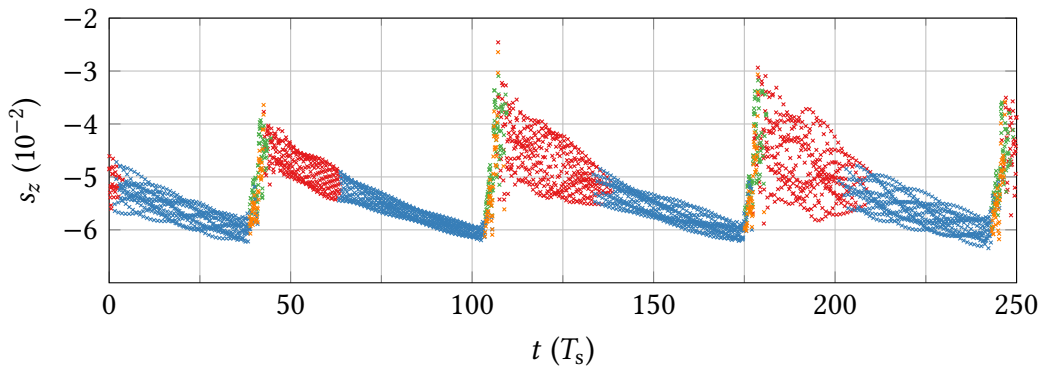

Figure A.4.: Shown is the skewness $s_z(t_i)$ of the longitudinal bunch profiles with bunch current $I_{\mathrm{saw}} = 1.15\,\mathrm{mA}$. Again, each value is colored according to the associated cluster labels $y(t_i)$.

A.4. Cluster Label Spectrogram Using a Simple Fourier Transformation

The spectral analysis of the generated cluster label sequences $y(t_i)$ is discussed in Section 4.5. As illustrated, the cluster label sequences should be treated as a time series of a categorical variable, making a simple Fourier transformation of the integer sequences not sufficient. However, as it can still be conducted, the results are shown in Figure A.5. These appear quite similar to the cluster label spectrogram in Figure 4.20, generated by calculating the spectral envelope.
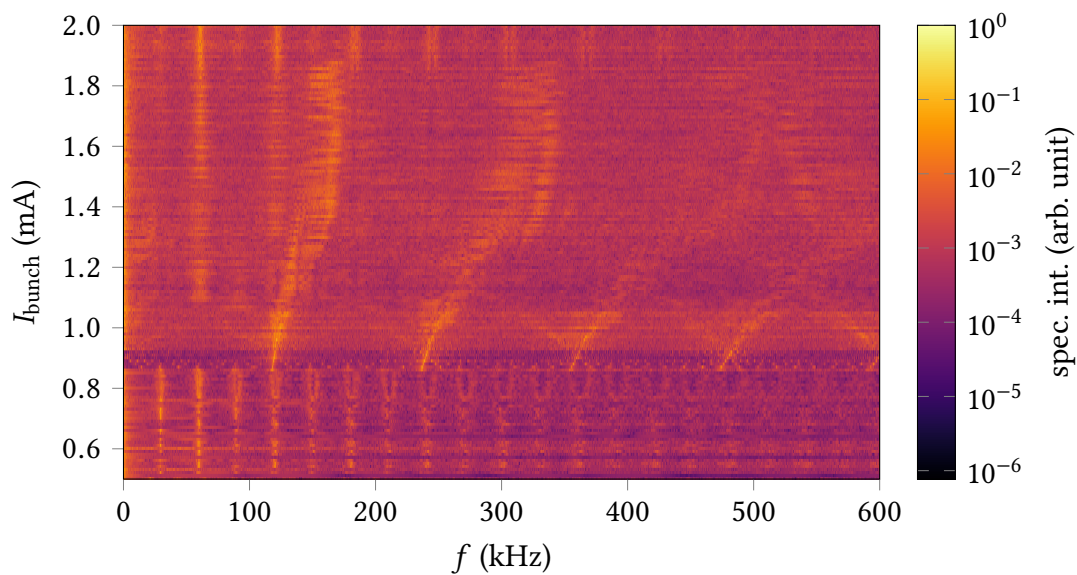
Figure A.5.: Cluster label spectrogram generated by calculating the Fourier transform of the integer cluster label sequences $y(t_i)$. Although the spectral analysis of the time series of a categorical variable requires more sophisticated methods, the results are quite comparable to Figure 4.20.

A.5. Modulation Frequencies and Amplitudes for the Second Data Set

In Section 4.4, the current-dependency of the scale of the found micro-structures is studied by determining the modulation frequency f_{mod} and amplitude A_{mod} on the longitudinal profiles. The same procedure can be applied to the aforementioned data set defined in Table 5.1, which displays low current bursting. The such obtained modulation frequencies for the 200 different bunch currents between $I_{\mathrm{bunch}} = 0.5\,\mu\mathrm{A}$ and $I_{\mathrm{bunch}} = 100\,\mu\mathrm{A}$ are shown in Figure A.6.
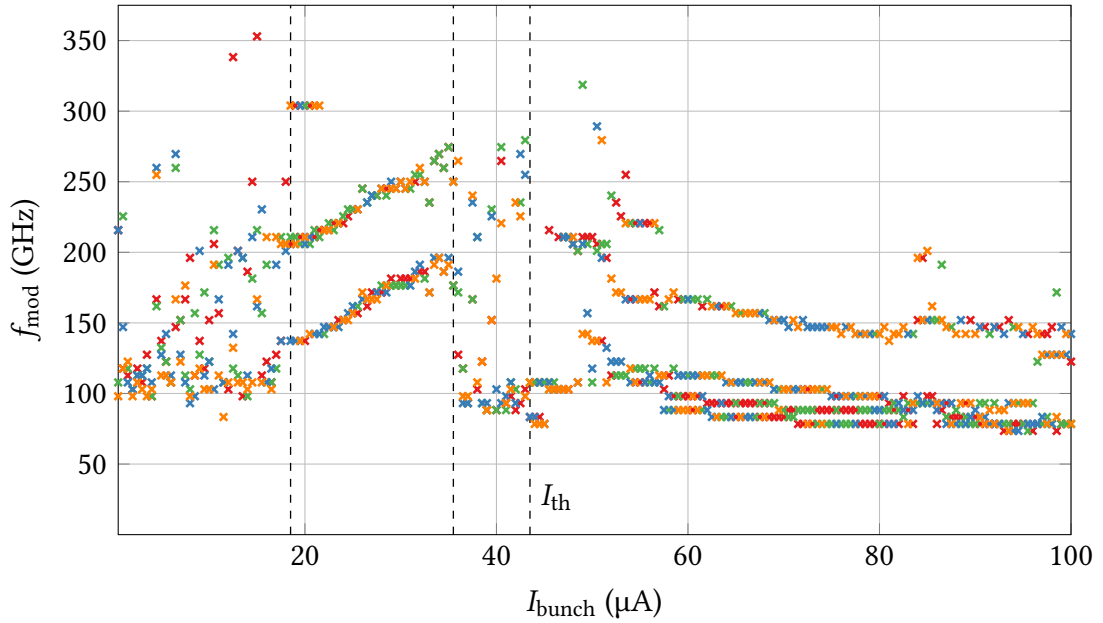
Figure A.6.: Analogously to Figure 4.17, the modulation frequencies f_{mod} are determined for this data set with the parameter settings in Table 5.1. The low current bursting regime is marked by two vertical, dashed lines at $I_{\mathrm{bunch}} = 18.5\,\mu\mathrm{A}$ and $I_{\mathrm{bunch}} = 35.5\,\mu\mathrm{A}$, while the third dashed line indicates the bursting threshold $I_{\mathrm{th}} \approx 43.5\,\mu\mathrm{A}$. While the results for the regular and sawtooth regime are quite comparable to the previous findings in Figure 4.17, the current-dependency of the modulation frequencies in the low current bursting regime appears considerably different.

Due to the generally shorter bunch lengths in this data set, the frequency corresponding to the deviations in bunch length is in the order of $f_{\mathrm{mod}} \approx 100\,\mathrm{GHz}$. Similarly to the previous results, despite a small decay, the modulation frequencies above the threshold I_{th} are concentrated around a constant value, in this case $f_{\mathrm{mod}} \approx 150\,\mathrm{GHz}$. However, from right above the threshold $I_{\mathrm{th}} \approx 43.5\,\mu\mathrm{A}$ to roughly $I_{\mathrm{bunch}} \approx 50\,\mu\mathrm{A}$, the modulation frequencies show the considerably higher values of approximately $f_{\mathrm{mod}} \approx 210\,\mathrm{GHz}$. Subsequently, right above $I_{\mathrm{bunch}} \approx 50\,\mu\mathrm{A}$, the modulation frequencies drop off abruptly to $f_{\mathrm{mod}} \approx 150\,\mathrm{GHz}$. Additionally, it should be mentioned, the low current bursting regime (marked by two vertical, dashed lines) displays significantly different results. Here, the modulation fre-

quencies are continuously increasing for higher bunch currents and are split into two
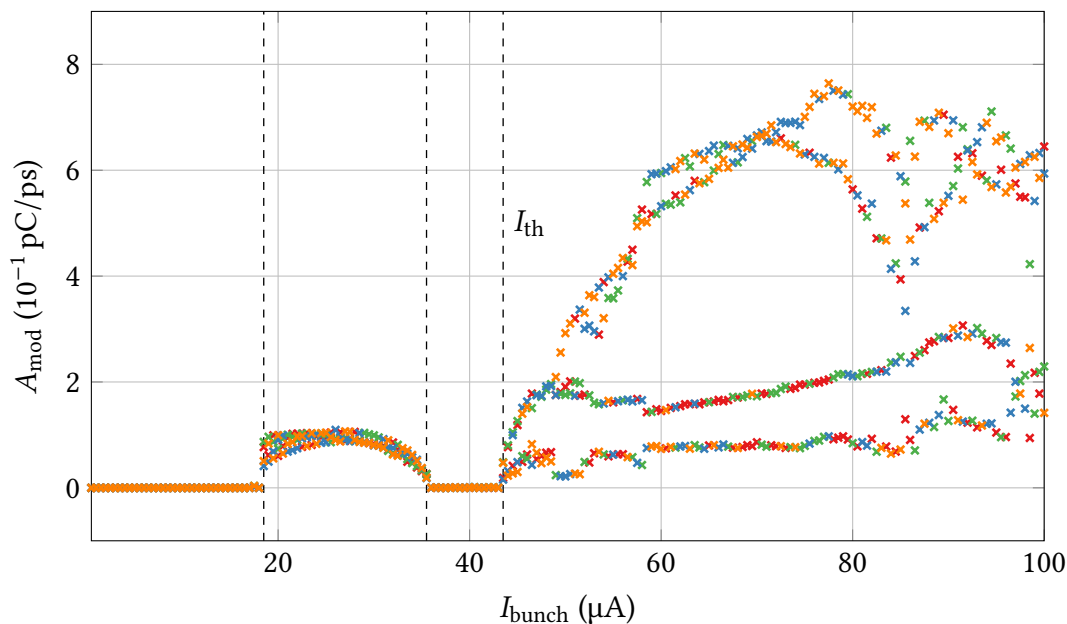separate regions of points.

Figure A.7.: Shown are the modulation amplitudes A_{mod} found for the data set with the
parameter settings in Table 5.1. As in Figure A.6, the vertical, dashed lines mark
the low current bursting regime between $I_{\mathrm{bunch}} = 18.5\,\mu\mathrm{A}$ and $I_{\mathrm{bunch}} = 35.5\,\mu\mathrm{A}$,
and the threshold $I_{\mathrm{th}} \approx 43.5\,\mu\mathrm{A}$. Again, the low current bursting regime shows
quite different results.

The corresponding modulation amplitudes A_{mod} are shown in Figure A.7. Similarly
to the previous findings displayed in Figure 4.18, the modulation amplitudes above the
threshold I_{th} are split into regions of higher and lower values, although here, there is an
additional separation for the points with smaller amplitude. For the low current bursting
regime, the modulation amplitudes are initially increasing for higher bunch currents until
they reach a maximum at approximately $I_{\mathrm{bunch}} \approx 27\,\mu\mathrm{A}$. Subsequently, the amplitudes are
decreasing again until the end of the low current regime is reached at $I_{\mathrm{bunch}} = 35.5\,\mu\mathrm{A}$. As
mentioned before, the deviating results for this low current bursting regime render it an
interesting subject for further investigations.

A.6. Micro-Structure Dependence on Vacuum Chamber Height

As mentioned in Section 3.1, Inovesa can model the radiation behavior, including the coherently emitted synchrotron radiation, of short electron bunches quite well, when the shielding effects of the beam pipe are approximated by two infinitely extending parallel plates. This becomes apparent by comparing the measured THz-Power spectrogram in Figure 2.7 with the simulated CSR power spectrogram in Figure 4.1 and is further addressed in Ref. [13]. The parallel plates distance g, which corresponds to the vacuum chamber height in real accelerators, can significantly influence the micro-structure dynamics and therefore the radiation behavior of the electron bunch. Although systematic studies were beyond the scope of this thesis, an additional data set with the same parameter settings defined in Table 3.1, but with the modified parallel plates distance $g' = 0.5\,g = 1.6\,\text{cm}$ was simulated and briefly analyzed. Figure A.8 shows the resulting referenced cluster centers for the application of the k-means method with $k = 2$ to the longitudinal profiles with bunch current $I_{\text{bunch}} = 1.4\,\text{mA}$, which lies in the regular bursting regime for these modified parameter settings.
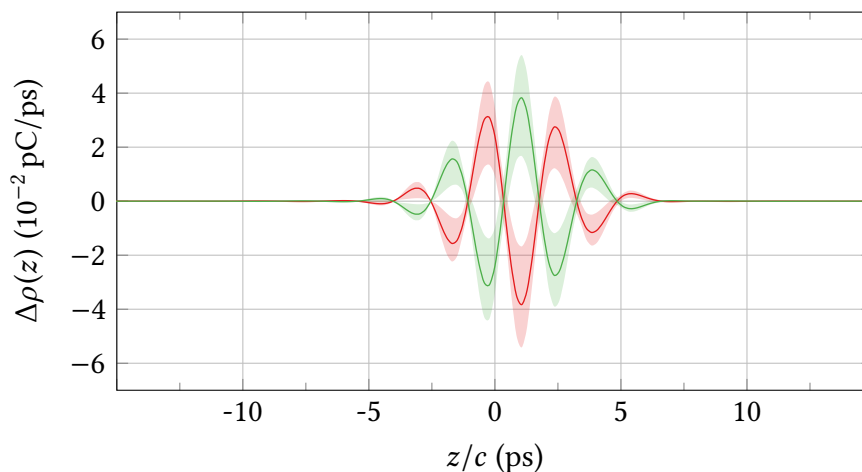

Figure A.8.: Referenced cluster center for modified parallel plates distance $g' = 0.5\,g$, bunch current $I_{\text{bunch}} = 1.4\,\text{mA}$ and $k = 2$. Similarly to Figure 4.2, these display the phase and paraphase of a modulation on the longitudinal profiles. However, this modulation is considerably more concentrated around the center of mass position and has a higher frequency.

Similarly to the previous results in the regular bursting regime, the found referenced cluster centers display the phase and paraphase of a modulation on the longitudinal profiles. The amplitude of this modulation is relatively high near the center of mass position as well. However, it drops off significantly quicker for positions far away from $z = 0$ when compared to e.g. Figure 4.2. The modulation frequency is considerably higher and amounts to $f_{\text{mod}} \approx 350\,\text{GHz}$.

By studying the corresponding phase space cluster means in Figure A.9, it becomes apparent, that these are the results of a higher number of micro-structures in the longitudinal phase space. In fact, there are approximately twice as many distinct structures

visible. As these are just the results for one particular set of simulation parameters, further investigations are required to confirm the correlation of the parallel plates distance g and the number of emerging micro-structures in the longitudinal phase space.
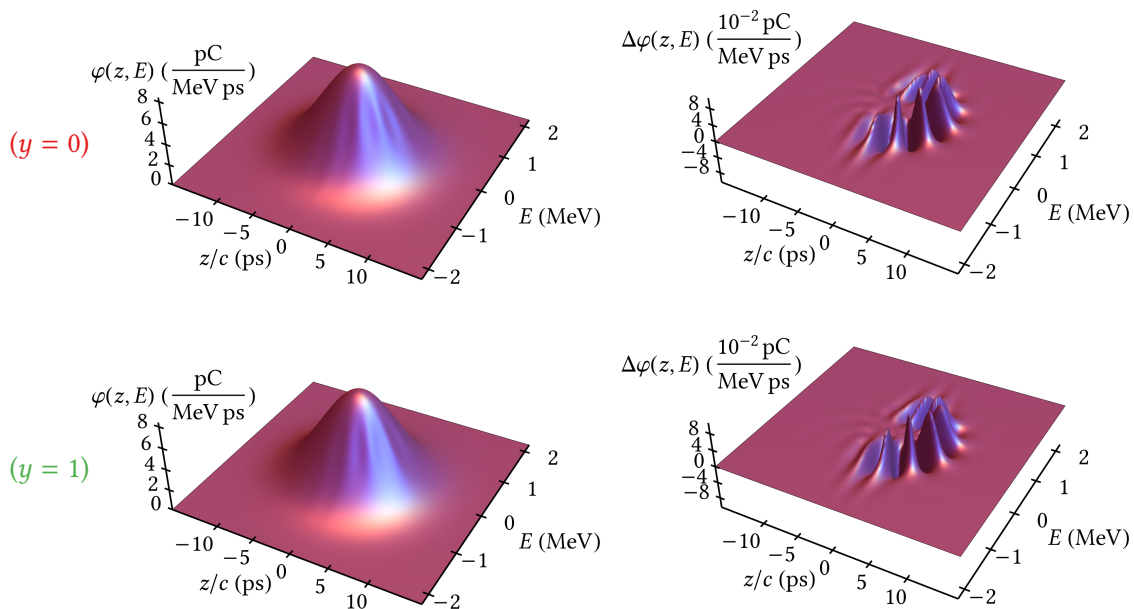

Figure A.9.: In the left column, the phase space cluster means for the modified parallel plates distance $g' = 0.5\,g$, bunch current $I_{bunch} = 1.4\,\text{mA}$ and $k = 2$ are shown. The right column displays the referenced phase space cluster means respectively.

Bibliography

1. Elder, F. R., Gurewitsch, A. M., Langmuir, R. V. & Pollock, H. C. Radiation from Electrons in a Synchrotron. *Phys. Rev.* **71,** 829–830 (11 1947).

2. Rowe, E. M. & Mills, F. E. Tantalus. 1. A Dedicated Storage Ring Synchrotron Radiation source. *Part. Accel.* **4,** 211–227 (1973).

3. Kobilka, B. The Structural Basis of G-Protein-Coupled Receptor Signaling (Nobel Lecture). *Angewandte Chemie International Edition* **52,** 6380–6388. ISSN: 1521-3773 (2013).

4. Nodvick, J. S. & Saxon, D. S. Suppression of coherent radiation by electrons in a synchrotron. *Phys. Rev.* **96,** 180 (1954).

5. Bane, K. L. F., Cai, Y. & Stupakov, G. Threshold studies of the microwave instability in electron storage rings. *Phys. Rev. ST Accel. Beams* **13,** 104402 (2010).

6. Evain, C. *et al.* Spatio-temporal dynamics of relativistic electron bunches during the micro-bunching instability in storage rings. *EPL (Europhysics Letters)* **98,** 40006 (2012).

7. Venturini, M. & Warnock, R. Bursts of Coherent Synchrotron Radiation in Electron Storage Rings: a Dynamical Model. *Phys. Rev. Lett.* 224802 (2002).

8. Müller, A.-S. *Accelerator-Based Sources of Infrared and Terahertz Radiation* in *Reviews of Accelerator Science and Technology* (2010), 165–183. doi:`http://dx.doi.org/10.1142/S1793626810000427`.

9. Abo-Bakr, M., Feikes, J., Holldack, K., Kuske, P. & Wustefeld, G. *Coherent emission of synchrotron radiation and longitudinal instabilities* in *Particle Accelerator Conference* (2003), 3023–3025. doi:`10.1109/PAC.2003.1289801`.

10. Shields, W. *et al.* Microbunch Instability Observations from a THz Detector at Diamond Light Source. *Journal of Physics: Conference Series* **357,** 012037 (2012).

11. J.Feikes *et al.* Metrology Light Source: The first electron storage ring optimized for generating coherent THz radiation. *Phys. Rev. ST Accel. Beams* **14,** 030705 (2011).

12. Hiller, N. *Electro-Optical Bunch Length Measurements at the ANKA Storage Ring* PhD thesis (KIT, 2013).

13. Schönfeldt, P., Brosi, M., Schwarz, M., Steinmann, J. L. & Müller, A.-S. Parallelized Vlasov-Fokker-Planck solver for desktop personal computers. *Phys. Rev. Accel. Beams* **20,** 030704 (3 Mar. 2017).

14. Wille, K. *The Physics of Particle Accelerators: An Introduction* 1st. ISBN: 978-0-19-850549-5 (Clarendon Press, 2001).

15. Wiedemann, H. *Particle Accelerator Physics* 4th. ISBN: 978-3-319-18316-9. doi:`10.1007/978-3-319-18317-6` (Springer, 2015).

16. Bernhard, A. *Accelerator Physics II: Synchrotron Light Sources* Lectures at KIT. 2016.

17. Müller, A.-S. *Accelerator Physics I: Particle Accelerators* Lectures at KIT. 2015.

18. Warnock, R. L. & Ellison, J. A. *A General method for propagation of the phase space distribution, with application to the sawtooth instability* in *The physics of high brightness beams. Proceedings, 2nd ICFA Advanced Accelerator Workshop, Los Angeles, USA, November 9-12, 1999* (2000), 322–348. doi:`10.1007/978-1-4419-7865-3`.

19. Podobedov, B. V. *Saw tooth instability studies at the Stanford Linear Collider damping rings* PhD thesis (SLAC, 1999).

20. Arp, U. *et al.* Spontaneous coherent microwave emission and the sawtooth instability in a compact storage ring. *Phys. Rev. ST Accel. Beams* **4,** 054401 (5 May 2001).

21. Carr, G., Kramer, S. & Murphy, J. *Investigation of coherent emission from the NSLS VUV ring* in *Particle Accelerator Conference* (1999), 134–136. doi:`10.1109/PAC.1999.795644`.

22. Stupakov, G. & Heifets, S. Beam instability and microbunching due to coherent synchrotron radiation. *Phys. Rev. ST Accel. Beams* **5,** 054402 (2002).

23. Samuel, A. L. Some Studies in Machine Learning Using the Game of Checkers. *IBM Journal of research and development,* 206–226 (1959).

24. Han, J., Pei, J. & Kamber, M. *Data Mining: Concepts and Techniques* 3rd. ISBN: 978-0-12-381479-1 (Morgan Kaufmann, 2011).

25. Bhat, P. C. *Multivariate Analysis Methods in Particle Physics* in *Annual Review of Nuclear and Particle Science* (2011), 281–309. doi:`10.1146/annurev.nucl.012809.104427`.

26. Bishop, C. M. *Pattern Recognition and Machine Learning* 424–428. ISBN: 978-0-387-31073-2 (Springer, 2006).

27. Duda, R. O., Hart, P. E. & Stork, D. G. *Pattern Classification* 2nd, 526–528. ISBN: 978-0-471-05669-0 (John Wiley & Sons, Inc., 2000).

28. Pedregosa, F. *et al.* Scikit-learn: Machine Learning in Python. *Journal of Machine Learning Research* **12,** 2825–2830 (2011).

29. R Core Team. *R: A Language and Environment for Statistical Computing* R Foundation for Statistical Computing (Vienna, Austria, 2014).

30. Wolfram Research, Inc. *Mathematica* Version 10.4 (Champaign, Illinois, USA, 2016).

31. Arthur, D. & Vassilvitskii, S. *k-means++: The Advantages of Careful Seeding* in *Proceedings of the eighteenth annual ACM-SIAM symposium on Discrete algorithms* (New Orleans, Louisiana, USA, 2007), 1027–1035.

32. Milligan, G. W. & Cooper, M. C. An examination of procedures for determining the number of clusters in a data set. *Psychometrika* **50,** 159–179 (1985).

33. Tibshirani, R., Walther, G. & Hastie, T. Estimating the number of clusters in a data set via the gap statistic. *Journal of the Royal Statistical Society: Series B (Statistical Methodology)* **63,** 411–423 (2001).

34. Rousseeuw, P. J. Silhouettes: A graphical aid to the interpretation and validation of cluster analysis. *Journal of Computational and Applied Mathematics* **20,** 53–65 (1986).

35. Alessio, S. M. *Digital Signal Processing and Spectral Analysis for Scientists: Concepts and Applications* 1st. ISBN: 978-3-319-25468-5 (Springer, 2016).

36. Stoffer, D. S., Tyler, D. E. & McDougall, A. J. Spectral analysis for categorical time series: Scaling and the spectral envelope. *Biometrika* **80,** 611–622 (1993).

37. Shumway, R. H. & Stoffer, D. S. *Time Series Analysis and Its Applications* 3rd. ISBN: 978-1-4419-7864-6. doi:`10.1007/978-1-4419-7865-3` (Springer, 2011).

38. Schönfeldt, P. *Simulation and measurement of the dynamics of ultra-short electron bunch profiles for the generation of coherent THz radiation* to be published. PhD thesis (KIT, 2017).

Acknowledgments